

ABSTRACT

QU, JUN. Development of Cylindrical Wire Electrical Discharge Machining Process and Investigation of Surface Integrity and Mechanical Property of EDM Surface Layers. (Under the direction of Albert J. Shih)

The cylindrical wire Electrical Discharge Machining (EDM) process was developed to generate precise cylindrical forms on hard, difficult-to-machine materials. A precise, flexible, and corrosion-resistant underwater rotary spindle was designed and added to a conventional two-axis wire EDM machine to enable the generation of free-form cylindrical geometries. A detailed spindle error analysis identified the major source of error at different frequencies. The mathematical models for material removal rate and surface finish were derived. Experimental results indicated that higher maximum material removal rate might be achieved in the cylindrical wire EDM than the 2D wire EDM. Effects of some key process parameters, wire feed rate, pulse on-time and part rotational speed, on the surface finish and roundness are explored. For WC-Co parts, an arithmetic average surface roughness and roundness as low as 0.68 and 1.7 μm , respectively, can be achieved. Surfaces of the cylindrical EDM parts were examined using Scanning Electron Microscopy (SEM) to identify the macro-ridges and craters on the surface. Cross-sections of the EDM parts are examined using the SEM to quantify the recast layer and heat-affected zone under various process parameters. This study also used nanoindentation to investigate the influence of cylindrical wire EDM process on the mechanical properties of WC-Co composite. Multiple indents were conducted on the cross-section of the recast layer, heat-affected zone, and bulk material. The SEM micrographs were used to correlate the individual nano-indent to the measured hardness

and modulus of elasticity. The experimental results showed that the heat-affected zone had more compact microstructure less indentation cracking. The recast layer had lower hardness and modulus of elasticity than the original material and heat-affected zone. EDS X-ray and X-ray diffraction were used to analyze the material compositions of the heat-affected zone and recast layer and to understand the effects of wire EDM process on the machined WC-Co surface. The micro-blasting process has been applied to improve the surface integrity of the part machined by wire EDM. The surface roughness of WC-Co parts could be reduced significantly using micro-size SiC abrasives. The surface finish improvement was also shown by the SEM micrographs of the blasted surfaces and their cross-sections. The undesired recast layer, which has poor mechanical properties and irregular features, was eventually removed by micro-blasting. Compressive residual stress introduced by micro-blasting could increase the surface wear resistance. Experiments with different process parameters were conducted to study the efficiency and effectiveness of micro-blasting for surface property control.

**DEVELOPMENT OF CYLINDRICAL WIRE ELECTRICAL DISCHARGE
MACHINING PROCESS AND INVESTIGATION OF SURFACE INTEGRITY
AND MECHANICAL PROPERTY OF EDM SURFACE LAYERS**

by
JUN QU

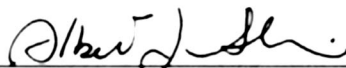
A dissertation submitted to the Graduate Faculty of
North Carolina State University
in partial fulfillment of the
requirements for the Degree of
Ph.D.

MECHANICAL ENGINEERING

Raleigh, North Carolina

2002

APPROVED BY:



Chair of Advisory Committee



Co-Chair of Advisory Committee

DEDICATION

May this work commemorate my grandmother, who dedicated herself to bringing me up. Through all life's sunny and rainy days, I feel you were there, which encouraged me to head up with smile. I would like to thank you in my heart, and I know you are listening.

To my family and all my friends I thank you for the past 29 years. I cannot think of better people to be with through this dance we call life.

BIOGRAPHY

Jun Qu was born in Shenyang, P.R. China. He is the first son of Weihong Qu and Guifeng Zhao and brother of Gang Qu. Both of his parents are environmental engineers and dedicate themselves to the research on air pollution and natural sources protection. In middle school, Jun met Ye Sun, who became his wife 13 years later. They fell in love in junior (1993) and got married in 1998 at Ames, Iowa. Now their lovely ten-month-old son, Steven S. Qu, has started to learn walking.

Jun showed his talents on Physics and Mathematics in high school and chose Precision Instrument Engineering as the major when he enrolled in Tianjin University in 1991. He achieved his Bachelor's degree and entered the graduate school in 1995. During his research work, Jun was lucky to get the guidance of Professor Guoxiong Zhang, one of the most famous scholars in precision engineering in the world.

At the beginning of 1998, Jun came to US and joined Iowa State University. After 18 months research work in CAD/CAM with Dr. Radha Sarma, he got another Master's degree in Mechanical Engineering. Jun achieved the Outstanding Paper Award Finalist from the North American Manufacturing Research Institution of the Society of Manufacturing Engineers (NAMRI/SME) in 1999.

Jun has spent the last three years pursuing a Doctoral degree in Mechanical Engineering at NC State University. To be a Ph.D. is one of his dreams from childhood. Under the guidance of his supervisor Dr. Albert Shih and advisory committee, Jun has done good research work in Precision Manufacturing and Material Characterization. He will be graduating in May and start working at Oak Ridge National Laboratory.

ACKNOWLEDGMENTS

I would like to first thank my advisor, Dr. Albert J. Shih. I have learned and improved a lot with your guidance and help in the past three years. Thank you for your efforts, time, and energy and give my best regards to you and your family.

I would like to take this opportunity to thank my advisory committee members, Dr. Jeffrey Eischen, Dr. John Strenkowski, and Dr. Paul Franzon, for your guidance and help.

I would like to thank my parents. Your unfailing support and encouragement have meant more than what you will ever know. With my heart, I thank you.

I would like to thank my wife, Ye Sun. Your love is always the source of my energy.

I would also like to give a special thank to my mother-in-law. Without your help on taking care of my son, I could not fully dedicate myself to the research work in the past twelve months.

Gratefully acknowledge the support by National Science Foundation Grant #9983582 (Dr. K. P. Rajurkar, Program Director).

Portion of this research was sponsored by the User program in the High Temperature Material Lab, Oak Ridge National Lab and the Heavy Vehicle Propulsion Systems Materials Program, Office of Transportation Technologies, US Department of Energy.

Thanks to Everyone at Oak Ridge National Lab who assisted in this research, especially:

- Dr. Arvid Pasto, for coordinating the involvement of NCSU with ORNL.
- Dr. Ray Johnson, for his guidance on this project.
- Sam McSpadden Jr., for facilitating the work at HTML, ORNL.
- Laura Riestler, for doing the Nanoindentation experiments.
- Dr. Ronald Ott, for his help during visiting HTML, ORNL.
- Dr. Thomas Watkins, for assisting the X-Ray diffraction experiments.
- Dr. Edgar Lara-Curzio, for assisting the material characterization.
- Tom Geer, for polishing the wire EDM parts.
- Dorothy Coffey, for assisting the SEM experiments.
- Randy Parten, for assisting the surface roughness and roundness measurement.
- Larry Walker, for assisting the SEM and EDX experiments.
- Tyler Jenkins, for slicing the wire EDM parts.

Thanks to Darryl Gust of Cummins Technical Center for the design and manufacture of the underwater spindle.

TABLE OF CONTENTS

	Page
LIST OF TABLES	vii
LIST OF FIGURES	viii
1. INTRODUCTION	1
1.1. Background of Electrical Discharge Machining (EDM)	1
1.2. Overview	6
References	8
2. CONCEPT, DESIGN, AND MATERIAL REMOVAL RATE OF CYLINDRICAL WIRE ELECTRICAL DISCHARGE MACHINING.....	10
2.1. Introduction.....	10
2.2. Spindle Design.....	12
2.3. Spindle Error Analysis.....	13
2.4. Material Removal Rate Modeling.....	15
2.5. Experiment on the Maximum Material Removal Rate	17
2.6. Concluding Remarks.....	22
References	23
3. SURFACE INTEGRITY AND ROUNDNESS OF CYLINDRICAL WIRE ELECTRICAL DISCHARGE MACHINING.....	24
3.1. Introduction.....	24
3.2. Surface Finish Modeling	26
3.3. Experiments on Surface Finish and Roundness	29
3.4. SEM Micrographs of EDM Surface and Sub-Surface	39
3.5. Concluding Remarks.....	44
References	45
4. ANALYTICAL SURFACE ROUGHNESS PARAMETERS OF A THEORETICAL PROFILE CONSISTING OF ELLIPTICAL OR CIRCULAR ARCS.....	47
4.1. Introduction.....	47
4.2. Closed-form Expressions of Roughness Parameters for a Theoretical Surface Profile Consisting of Elliptical Arcs.....	49
4.3. Roughness Parameters in Dimensionless Form.....	54
4.4. Theoretical Surface Profile Consisting of Circular Arcs	59
4.5. Approximate Solutions	60
4.6. Concluding Remarks.....	66

References	67
5. NANOINDENTATION CHARACTERIZATION OF SURFACE LAYERS OF ELECTRICAL DISCHARGE MACHINED WC-CO	70
5.1. Introduction.....	70
5.2. Experiment Setup and Sample Preparation.....	71
5.3. Experimental Results and Discussion.....	73
5.4. Concluding Remarks.....	83
References	84
6. ABRASIVE MICRO-BLASTING OF WIRE ELECTRICAL DISCHARGE MACHINED WC-CO COMPOSITE	87
6.1. Introduction.....	87
6.2. Sample Preparation and Experiment Setup	91
6.3. Experimental Results and Discussion.....	93
6.4. Concluding Remarks.....	100
References	100
7. CONCLUSIONS.....	103
APPENDICES	106
Appendix A. Material Removal Rate Modeling in Cylindrical Wire EDM.....	107
Appendix B. Derivation of Semi-Axes a and b and Feed f for a Measurement Profile on the Surface Machined by Flat-End Milling	112
Appendix C. Derivation of the Closed-Form R_a and R_q Using the Parametric Form	114

LIST OF TABLES

	Page
Chapter 2	
Table 2.1. Machine setup for the cylindrical wire EDM experiment	18
Table 2.2. MRR_{max} for the cylindrical wire EDM test with $\mathbf{a} = 0$ and gradually increasing v_f	20
Table 2.3. MRR_{max} for the cylindrical wire EDM test with constant \mathbf{a} and v_f	20
Table 2.4. MRR_{max} for the 2D wire EDM test	21
Chapter 3	
Table 3.1. Machine setup for the Experiments I and II.....	31
Table 3.2. Material removal rate of Experiments I and II.....	31
Table 3.3. Surface finish of 2D wire EDM parts in Experiment I	34
Chapter 4	
Table 4.1. Error analysis of approximate solutions	66
Chapter 5	
Table 5.1. Hardness and modulus of elasticity of bulk material, heat-affected zone, and recast layer in descending order of the hardness.....	75
Table 5.2. Experimental conditions of the X-ray diffraction measurements	82
Chapter 6	
Table 6.1. Process parameters of wire EDM rough cut and skim cut	91
Table 6.2. Process parameters of Micro-blasting experiments	92

LIST OF FIGURES

	Page
Chapter 1	
Fig. 1.1. Illustration of the wire EDM process	2
Fig. 1.2. Four types of gap conditions in EDM	3
Fig. 1.3. Evolution of a single spark in the EDM process	5
Chapter 2	
Fig. 2.1. The concept of cylindrical wire EDM process	11
Fig. 2.2. A cylindrical wire EDM part with the same shape as the diesel engine injector plunger.....	11
Fig. 2.3. Side view of the hybrid bearing underwater spindle	13
Fig. 2.4. Spindle error at 30 rpm rotational speed	14
Fig. 2.5. Spindle error vs. Rotational speed	15
Fig. 2.6. FFT frequency spectrum of the spindle error	15
Fig. 2.7. Parameters in the free form cylindrical wire EDM process	16
Fig. 2.8. Four test configurations to find the maximum material removal rate.....	19
Fig. 2.9. Key parameters of the two configurations to find the maximum material removal rate in cylindrical wire EDM	20
Chapter 3	
Fig. 3.1. Cross-section view of an ideal cylindrical wire EDM surface and the key parameters and coordinate system for mathematical modeling	26
Fig. 3.2. The configuration of surface finish experiment	32
Fig. 3.3. The surface finish and roundness of cylindrical wire EDM parts in Experiment I with high material removal rate.....	35
Fig. 3.4. The surface finish and roundness of cylindrical wire EDM parts in Experiment II with improvements on surface finish and roundness	38
Fig. 3.5. SEM micrographs of macro-ridges and ideal arcs on surfaces of brass parts in Experiment I	40
Fig. 3.6. SEM micrographs of surfaces and cross-sections of carbide parts	41
Fig. 3.7. SEM micrographs of surfaces and cross-sections of brass samples	42
Chapter 4	
Fig. 4.1. A theoretical surface profile consisting of elliptical arcs	50
Fig. 4.2. Dimensionless surface roughness parameters R_t/b , R_a/b , and R_q/b vs. f/a ...	58
Fig. 4.3. Comparison of closed-form and approximate solutions of surface finish parameters.....	65

Chapter 5

Fig. 5.1.	MTS Nano-indenter TM II.....	73
Fig. 5.2.	Nanoindentation on the cross-section of WC-Co part machined by cylindrical wire EDM	74
Fig. 5.3.	Nanoindentation on the bulk material	77
Fig. 5.4.	Nanoindentation on heat-affected zone	79
Fig. 5.5.	EDS X-Ray analysis of the recast layer	81
Fig. 5.6.	X-Ray diffraction analysis of the recast layer	81
Fig. 5.7.	Nanoindentation on the recast layer	83

Chapter 6

Fig. 6.1.	SEM micrographs of the surface and cross-section of a WC-Co part machined by wire EDM.....	88
Fig. 6.2.	Micro-blasting on a micro cylindrical wire EDM WC-Co part	90
Fig. 6.3.	Two sizes of SiC abrasives	92
Fig. 6.4.	Erosion wear rate of micro-blasting on wire EDM WC-Co.....	94
Fig. 6.5.	Surface finish improvement on wire EDM WC-Co using micro-blasting ..	97
Fig. 6.6.	SEM micrographs of surfaces and cross-sections of the wire EDM rough cut WC-CO part after micro-blasting using abrasive A at 0.276 MPa air pressure	97
Fig. 6.7.	SEM micrographs of surfaces and cross-sections of the wire EDM rough cut WC-CO part after micro-blasting using abrasive A at 0.138 MPa air pressure	98
Fig. 6.8.	SEM micrographs of surfaces and cross-sections of the wire EDM rough cut WC-CO part after micro-blasting using abrasive B at 0.138 MPa air pressure	98
Fig. 6.9.	SEM micrographs of surfaces and cross-sections of the wire EDM skim cut WC-CO part after micro-blasting using abrasive B at 0.276 MPa air pressure	99
Fig. 6.10.	SEM micrographs of surfaces and cross-sections of the wire EDM skim cut WC-CO part after micro-blasting using abrasive A at 0.276 MPa air pressure	99

Appendices

Fig. A.1.	Free form geometry in cylindrical wire EDM	107
Fig. A.2.	Calculation of V_{II}	108
Fig. A.3.	Calculation of V_{III}	110
Fig. B.1.	The measurement profile on the surface machined by flat-end milling	113

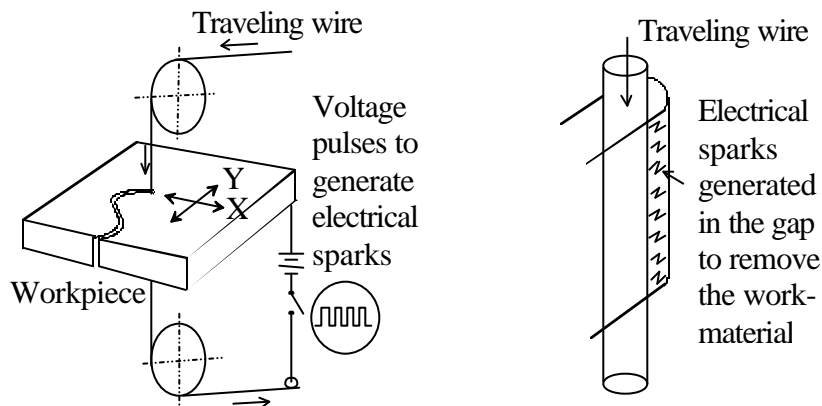
CHAPTER 1. INTRODUCTION

1.1. Background of Electrical Discharge Machining (EDM)

In the past decades, EDM technology has gradually evolved and become an important manufacturing process. EDM is a thermoelectric process that erodes workpiece material by a series of discrete electrical sparks between the workpiece and electrode flushed by or immersed in a dielectric fluid. Unlike traditional cutting and grinding processes which rely on a much harder tool or abrasive material to remove the softer work-material, the EDM process utilizes electrical sparks or thermal energy to erode the unwanted work-material and generate the desired shape. The material removal rate of EDM process mainly depends on the electrical conductivity and melting temperature of the work-material [1]. A workpiece with higher electrical conductivity and lower melting temperature can be machined more efficiently. The hardness and strength of the work-material are no longer the dominating factors that affect the tool wear and hinder the machining process. This makes EDM particularly suitable for machining hard, difficult-to-machine materials, such as Metal Matrix Composites (MMCs). The EDM process has the ability to machine precise, complex, and irregular shapes with a CNC control system. In addition, the cutting force in the EDM process is small, which makes it ideal for fabricating parts with miniature features. Ehrfeld et al. [2] and Michel and Ehrfeld [3] reviewed the application of micro wire EDM in

manufacturing mechatronic micro devices. Kruusing, et al. [4] studied the machining of micro-magnets. The micro-EDM of silicon has also been well addressed [5,6].

There are two typical types of EDM processes, die-sinking EDM and wire EDM. The electrode of die-sinking EDM has the reversed shape of the part to be machined, while wire EDM uses brass wire, ranging from 0.01 to 0.36 mm in diameter, as the electrode. Figure 1.1(a) illustrates the wire EDM process, a traveling wire eroding a groove in the workpiece. The close-up view of the gap and electrical sparks between the wire and workpiece is illustrated in Fig. 1.1(b).



(a) Wire EDM.

(b) Close-up view of the gap.

Fig. 1.1. Illustration of the wire EDM process.

Four types of gap conditions, open, spark, arc, and short, exist in the EDM process, as shown in Fig. 1.2 [1]. It can be seen that sparks or effective discharge require some delay time before the discharge current reaches its nominal value. The arcs, however, require negligible or zero delay time and occur at a lower breakdown voltage due to partially deionized dielectric. When the distance between the two electrodes is far

enough, an open voltage pulse occurs with no current. A short circuit pulse is the result of direct contact between the wire electrode and the workpiece. The debris particles in the gap may form a bridge between two electrodes to create a short circuit. Flushing with the high pressure deionized water is the way to prevent it. Sparks are the desired gap condition in EDM. Arcs, which damage the surface finish and dimensional accuracy, should be avoided. In order to optimize the EDM process, different types of monitoring and control systems have been developed, such as the ignition delay monitoring system [7], DDS monitoring system [8], R.F. monitoring system [8], and EDM discharge parameter monitoring system [10,11].

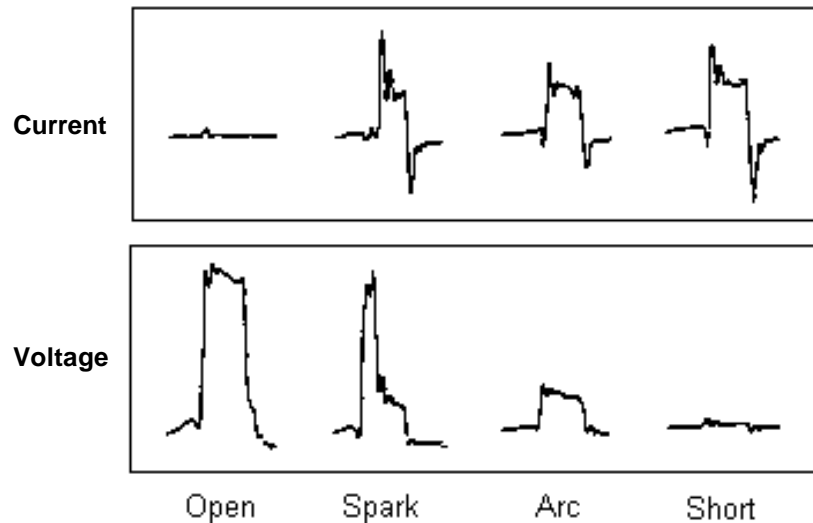


Fig. 1.2. Four types of gap conditions in EDM [1].

The procedure of a single electrical spark discharge can be illustrated by Fig. 1.3 [12]. The voltage and current charts are shown at the bottom of each illustration. In all the diagrams, the electrode (anode in this case) is the upper dark-color material and the

workpiece is the lower jagged part that is negatively charged. The dielectric fluid in the machining gap serves as an insulator. First, the electrode moving close to the workpiece as shown in Fig. 1.3(a). As the potential difference increases between the two surfaces, the local dielectric fluid breaks down and ions are generated. The electrical field is strongest at the point where the distance between the two surfaces is minimal. The electrical spark will occur at that location. Note the voltage has increased, but no current is flowing because of the presence of the dielectric material.

Next, as shown in Fig. 1.3(b), more and more ions have been generated, making the insulating properties of the dielectric fluid begin to decrease along a narrow channel at the point with the strongest electrical field. Voltage reaches its peak, while current is still zero. Figure 1.3(c) shows that a current starts to be established, causing the voltage to decrease. A discharge channel begins to form between the electrode and workpiece. The voltage continues dropping, as shown in Fig. 1.3(d), while the current continues increasing. Heat builds up rapidly, causing some of the anode, cathode, and dielectric materials to vaporize.

Figure 1.3(e) depicts the expansion of the discharge channel full of vapor is constrained by the rush of ions, attracted by the intense electro-magnetic field, toward it. Figure 1.3(f) is near the end of the voltage on cycle. The current and voltage have stabilized. The heat and pressure inside the channel have reach the maximum and some materials have been melted and removed. The molten material is held in place by the pressure of vapor.

Figures 1.3(g), 1.3(h), and 1.3(i) show what happens after voltage and current go to zero. The temperature and pressure rapidly decrease in the discharge channel and causes it to collapse, which allows the molten material to be expelled from the surface of the workpiece. Fresh dielectric material, if used, comes in, flushes the debris away, and quenches the surfaces of the anode and cathode. Unexpelled molten material resolidifies back to the surface to form a recast layer. This electrical spark is done and the environment is ready for next spark.

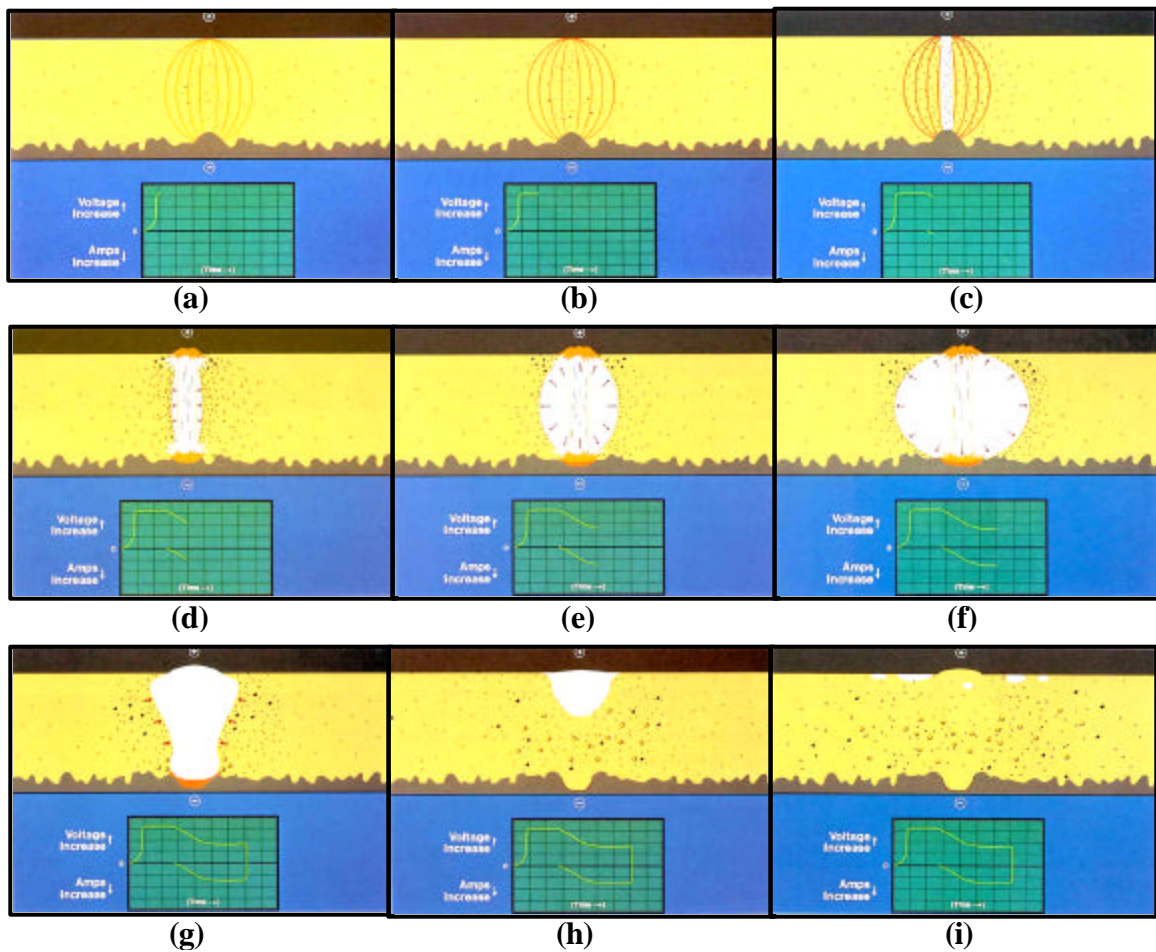


Fig. 1.3. Evolution of a single spark in the EDM process [12].

1.2. Overview

In this study, the cylindrical wire EDM process is developed to generate free-form cylindrical components. Applications of this process include the diesel injector plunger, engine valve, turbo-charger shaft, hydraulic pump actuator, miniature parts, etc. It is especially suitable for the hard, wear-resistant materials, such as Inconel, cermets, polycrystalline diamond and CBN, etc. The surface integrity and mechanical properties of the surface layers machined by cylindrical wire EDM have also been investigated. These topics are going to be addressed in the following Chapter 2-6. Partial results have been covered in four journal papers [13-16] and presented in the ASME and ASPE conferences in 2001 [17-18].

The concept, spindle design, and material removal rate of the cylindrical wire EDM development is summarized in Chapter 2 and [13,17,18]. The concept is first described. A precision underwater rotary spindle is then designed and manufactured to rotate the part to enable the generation of free-form cylindrical shapes. Fast Fourier transformation is applied to analyze the spindle error to identify the major error sources. The mathematical model for material removal rate is built and the experiments are conducted to find the maximum material removal rate in both cylindrical wire EDM and the 2D wire EDM.

Chapter 3 and [16] are focused on the surface finish and roundness of the cylindrical wire EDM parts. The mathematical model for surface finish is derived. Experiments are conducted to investigate the effects of the key process parameters of cylindrical wire

EDM on the surface finish and roundness. Surfaces and cross-sections of the machined parts are also examined using Scanning Electron Microscopy to identify and analyze the damage layers generated by electrical sparks during the cylindrical EDM process.

The theoretical profile of the surface machined by cylindrical wire EDM is found to consist of small and repetitive circular arcs. Similar profiles exist on the surfaces of turning and end milling processes. In Chapter 4 and [15], the theoretical profile consisting of elliptical or circular arcs is investigated and the closed-form expressions of the three roughness parameters, the peak-to-valley roughness R_t , arithmetic average roughness R_a , and root-mean-square roughness R_q , are derived.

The mechanical properties of surface layers generated in cylindrical wire EDM are critical to the part performance, particularly the fatigue and wear properties. Chapter 4 and [16] introduces the nanoindentation technique to investigate the influence of cylindrical wire EDM process on the mechanical properties of WC-Co composite. Multiple indents are conducted on the cross-section of the surface, subsurface, and bulk material. The SEM micrographs is used to correlate the individual nano-indent to the measured hardness and modulus of elasticity. EDS X-Ray and X-Ray diffraction are used to analyze the material compositions of the damage layers.

Chapter 5 presents the surface integrity improvement using micro-blasting. The wire EDM surfaces are blasted using 5~10 microns size SiC media and the effect of key process parameters of micro-blasting on surface roughness is studied. The micro-blasted surfaces and their cross-sections are also examined by SEM.

References

- [1] Rajurkar, K. P. and Pandit, S. M., 1988, "Recent Progress in Electrical Discharge Machine Technology and Research," *Proceedings of Manufacturing International '88, Atlanta, GA, USA*, Vol. 1, pp. 219-226.
- [2] Ehrfeld, W., Lehr, H., Michel, F., and Wolf, A., 1996, "Micro Electro Discharge Machining as a Technology in Micromachining," *SPIE*, Vol. 2879, pp. 332-337.
- [3] Michel, F., and Ehrfeld, W., 1999, "Mechatronic Micro Devices," *1999 International Symposium on Micromechatronics and Human Science, IEEE*, pp. 27-34.
- [4] Kruusing, A., Leppavuori, S., Uusimaki, A., Petretis, B. and Makarova, O., 1999, "Micromachining of magnetic materials," *Sensors and Actuators*, Vol. 74, pp. 45-51.
- [5] Reynaerts, D., Meeusen, W., Van Brussel, H., 1998, "Machining of three-dimensional microstructures in silicon by electro-discharge machining," *Sensors and Actuators*, Vol. 67, pp. 159-165.
- [6] Reynaerts, D. and Van Brussel, H., 1999, "Micro-EDM: A versatile technology for silicon micromachining," *Int. J. Japan Soc. Prec. Eng.*, Vol. 33, No. 2, pp. 114-119.
- [7] Snoeys, R. and Cornellissen, H., 1975, "Correlation between Electro-Discharge Machining Data and Machining Settings," *Annals of the CIRP*, Vol. 24, No. 1, pp. 83-88.
- [8] Rajurkar, K. P., Pandit, S. M., and Wittig, W. H., 1983, "Pulse Current as a Sensor for On-line Control of EDM," *Transactions of North American Manufacturing Research Institution of SME, 1983*, pp. 379-385.
- [9] Bhattacharyya, S. K. and El-Menshawy, M. F., 1978b, "Monitoring the EDM process by Radio Signals," *International Journal of Production Research*, Vol. 16, No. 5.
- [10] Rajurkar, K. P. and Wang, W. M., 1993, "Thermal Modeling and On-line Monitoring of Wire-EDM," *Journal of Materials Processing Technology*, Vol. 38, pp. 417-430.
- [11] Rajurkar, K. P. and Wang, W. M., 1997, "Improvement of EDM Performance with Advanced Monitoring and Control System," *Transactions of the ASME*, Vol. 199, pp. 770-775.
- [12] Poco, 2000, *EDM Technology Manual*, Poco Graphite Inc.

- [13] Qu, J., Shih, A. J., and Scattergood, R., 2002, "Development of the Cylindrical Wire Electrical Discharge Machining Process, Part I: Concept, Design, and Material Removal Rate," *Journal of Manufacturing Science and Engineering* (accepted).
- [14] Qu, J., Shih, A. J., and Scattergood, R., 2002, "Development of the Cylindrical Wire Electrical Discharge Machining Process, Part II: Surface Integrity and Roundness," *Journal of Manufacturing Science and Engineering* (accepted).
- [15] Qu, J. and Shih, A. J., 2002, "Analytical Surface Roughness Parameters of a Theoretical Profile Consisting of Elliptical or Circular Arcs," *Precision Engineering* (submitted).
- [16] Qu, J., Riester, L., Shih, A. J., Scattergood, R., Lara-Curzio, E., and Watkins, T., 2002, "Nanoindentation Characterization of Surface Layers of Electrical Discharge Machined Wc-Co," *Materials Science and Engineering-A* (to be submitted).
- [17] Qu, J., Shih, A.J., and Scattergood, R., "Development of the Cylindrical Wire Electrical Discharge Machining Process," *Symposium on Nontraditional Manufacturing Research and Applications, Proceedings of 2001 ASME International Mechanical Engineering Congress and Exposition, Vol. 3, IMECE2001/MED-23343, Nov. 11-16, New York, 2001.*
- [18] Qu, J., Shih, A. J., Scattergood, R. and McSpadden, S. B., "Cylindrical Wire Electrical Discharge Machining Process Development," *Proceedings of the ASPE 2001 Annual Meeting, Vol. 25, Nov. 10-15, 2001, pp. 501-504.*

CHAPTER 2. CONCEPT, DESIGN, AND MATERIAL REMOVAL RATE OF CYLINDRICAL WIRE ELECTRICAL DISCHARGE MACHINING

2.1. Introduction

The concept of cylindrical wire EDM is illustrated in Fig. 2.1. A rotary axis is added to a conventional two-axis wire EDM machine to enable the generation of a cylindrical form. The initial shape of the part needs not to be cylindrical in shape. The electrically charged wire is controlled by the X and Y slides to remove the work-material and generate the desired cylindrical form. An example of the diesel fuel system injector plunger machined using the cylindrical wire EDM method is shown in Fig. 2.2.

The idea of using wire EDM to machine cylindrical parts has been reported by Dr. Masuzawa's research group at University of Tokyo [1-8]. These research activities were aimed to manufacture small-diameter pins and shafts. A wire guide was used to reduce the wire deflection during EDM of small-diameter shafts. Cylindrical pins as small as 5 μm in diameter can be machined [8]. The small-diameter pins can be used as tools for 3D micro-EDM applications [9, 10].

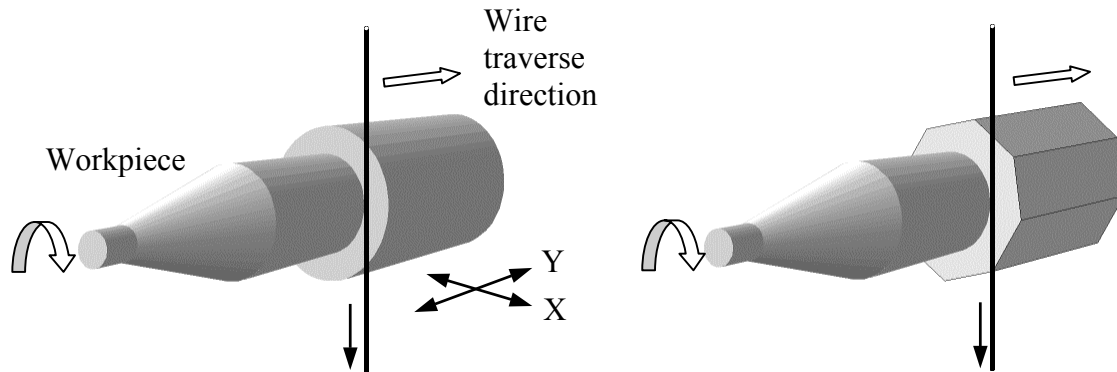


Fig. 2.1. The concept of cylindrical wire EDM process.

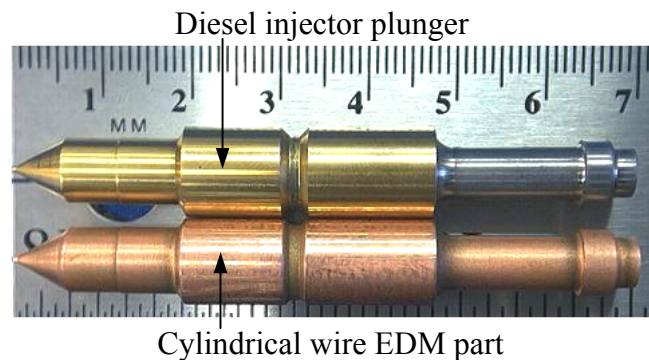


Fig. 2.2. A cylindrical wire EDM part with the same shape as the diesel engine injector plunger.

In this study, instead of machining small-diameter pins, the focus is on exploring high material removal rates in the cylindrical wire EDM process. The material removal rate data was not reported in Masuzawa's research [1-8]. In this study, two configurations to find the maximum material removal rate for cylindrical wire EDM were explored. One of the difficult-to-machine metal matrix ceramic composites, tungsten carbide in cobalt matrix, was used in this study. The mathematical model for material removal rate was derived to help understand and improve the cylindrical wire EDM process.

The spindle design and spindle error analysis methods are first presented in this paper. The model of material removal rate in free-form cylindrical wire EDM is then derived. Finally, the experimental results of the maximum material removal rates in the cylindrical wire EDM process are analyzed and compared to that of 2D wire EDM.

2.2. Spindle Design

The rotating workpiece is driven by a spindle, which is submerged in a tank of deionized water. Two jets of high-pressure water are used to flush the workpiece to improve the material removal rate and maintain a uniform thermo-environment. A precision underwater spindle is the key subsystem of the experiment. This spindle must meet the following design criteria:

1. *Accuracy*: The spindle error needs to be small to machine accurate parts and maintain the consistent gap condition.
2. *Flexibility*: The spindle has to accommodate different sizes of workpiece.
3. *High Current Electrical Connection*: Wire EDM requires high-current, high-voltage electrical connections between the rotating workpiece and the ground. A back-wired carbon electrical brush is required for the electrical connection to the rotating workpiece.
4. *Corrosion Resistance*: Because the spindle is underwater, components of the spindle need to be corrosion resistant in water.

The picture of the underwater spindle used in this study is shown in Fig. 2.3, respectively. A pair of deep groove silicon nitride ball bearings with stainless steel rings

was used. The gear motor was located above water on the top of the frame. A timing belt was used to transmit the rotational motion to the R8 collet holder. Precision internal grinding of the angle in the collect holder was required to achieve the desired runout specification, which is less than $10\ \mu\text{m}$ on the part 20 mm from the face of the collet.

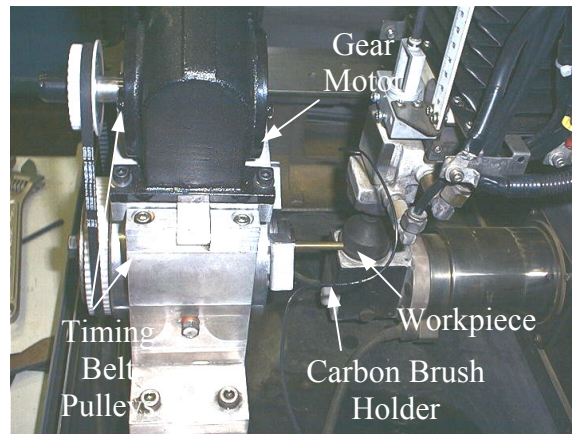


Fig. 2.3. Side view of the hybrid bearing underwater spindle.

2.3. Spindle Error Analysis

Spindle runout error is an important parameter that can affect the maximum material removal rate, roundness, and surface finish of cylindrical wire EDM parts. The Donaldson reversal principle [11] was applied to measure the spindle error. An electronic indicator with $0.1\ \mu\text{m}$ resolution was used to measure two runout traces on opposite sides of a 6.35 mm diameter silicon-nitride bar. The spindle error can be calculated from these two runout traces. A sample spindle error trace at 30 rpm is shown in Fig. 2.4. The maximum spindle error is defined as the average peak to valley value on the error trace. Results of the maximum spindle error at 10 different speeds are shown in

Fig. 2.5. Fourier transformation was applied to analyze the spindle runout data to identify the source of error. Figure 2.6 shows the amplitude of error vs. frequency for two spindle rotational speeds at 30 and 60 rpm. Four major peaks can be identified.

- (i) f_o : This is the major peak, which is caused by the off center error. The position of this peak always corresponds to the spindle rotational speed.
- (ii) f_1 : This is always equal to five times the rotational speed of the spindle, possibly caused by the form error on bearing races.
- (iii) f_3 and f_4 : These two frequencies, 60 and 120 Hz, remain unchanged for different motor rotational speeds. The frequency peak at 120 Hz is possibly caused by the DC motor. The amplitude of the frequency at 60 Hz is only significant at certain motor rotational speeds, such as 90 and 180 rpm. This is possibly caused by resonance at the spindle's natural frequency, which is measured as 60 Hz.

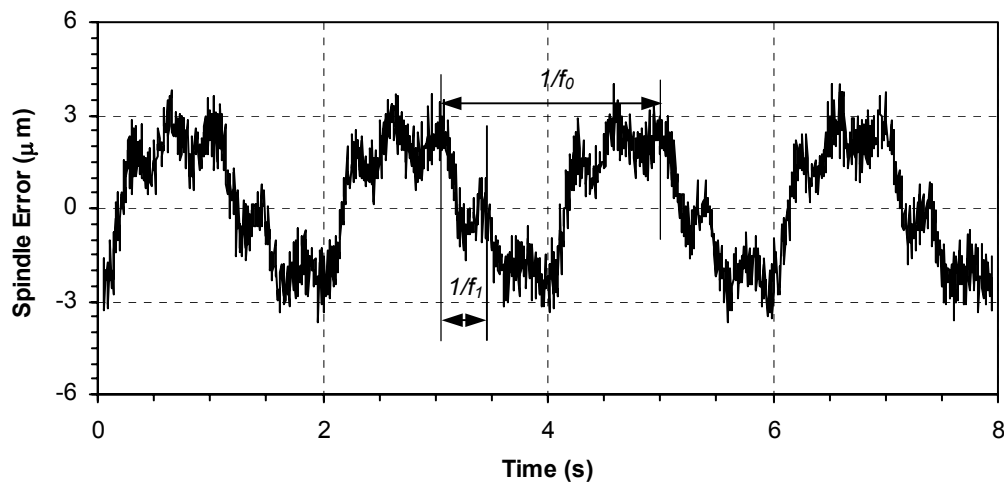


Fig. 2.4. Spindle error at 30 rpm rotational speed.

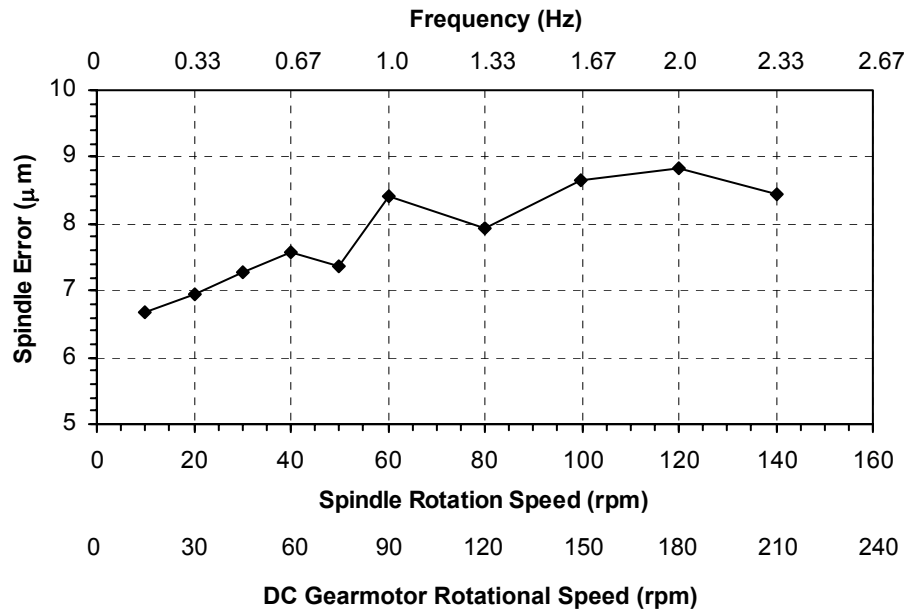
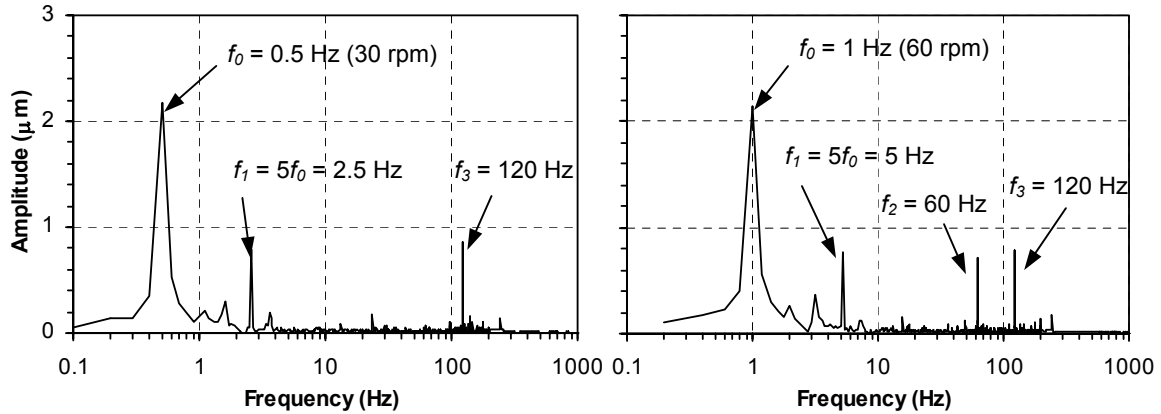


Fig. 2.5. Spindle error vs. rotational speed.



(a) Spindle rotation speed of 30 rpm. (b) Spindle rotation speed of 60 rpm.

Fig. 2.6. FFT Frequency spectrum of the spindle error.

2.4. Material Removal Rate Modeling

The process parameters for modeling the material removal rate in cylindrical wire EDM of a free-form shape are illustrated in Fig. 2.7. An XY coordinate system is first

defined. The X-axis coincides with the rotational axis of the workpiece. The positive direction of the X-axis is determined by the direction of the wire traverse velocity vector, v_f . The component of the wire traverse velocity vector on the X-axis is always positive. The Y-axis, in the radial direction of the cylindrical workpiece, is perpendicular to both the X-axis and the wire. Assume the original workpiece is in cylindrical geometry. R is the original radius of the workpiece. r_e is the radius of the effective circle, C_e , which equals the wire radius, r_w , plus the width of the gap between the wire and the workpiece. r is the minimum distance from the effective circle, C_e , to the rotational axis of the workpiece. v_f , the magnitude of v_f , is equal to the wire feed rate during machining. α is the angle from the positive X-axis to v_f . The range of α is from $-\pi/2$ to $\pi/2$.

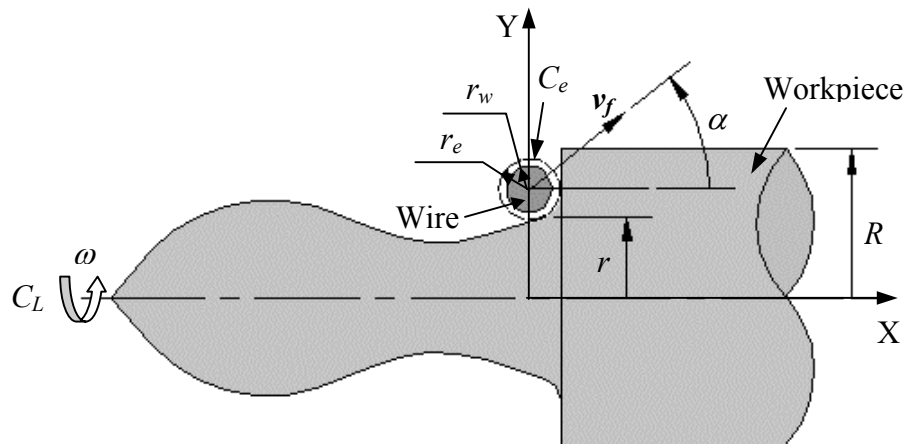


Fig. 2.7. Parameters in the free form cylindrical wire EDM process.

The Material Removal Rate (*MRR*) in cylindrical wire EDM of a free-form cylindrical geometry is shown in Eq. (2.1) with the detailed derivation summarized in the Appendix A.

$$MRR = v_f \cdot \pi[(R^2 - r^2) \cos \alpha + 2rr_e(1 - \sin \alpha - \cos \alpha) + r_e^2(2 - 2 \cos \alpha + (\frac{\pi}{2} - 2 - \alpha) \sin \alpha)] \quad (2.1)$$

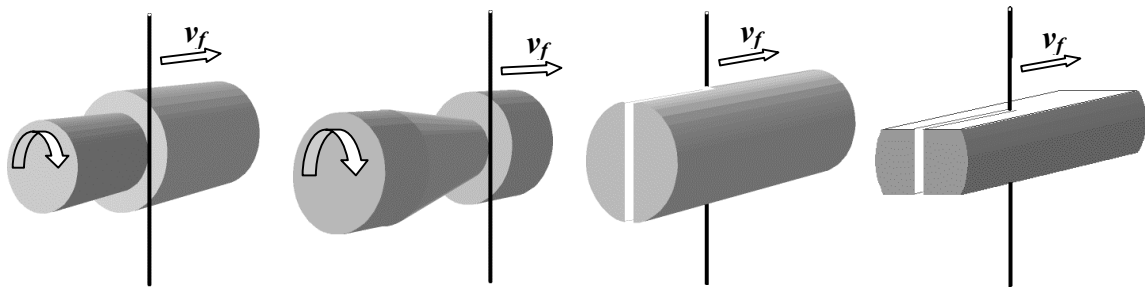
2.5. Experiment on the Maximum Material Removal Rate

Two types of materials, carbide and brass, were used in this study. The carbide material is 1 to 2 μm size tungsten carbide in a 10% cobalt matrix. This material has hardness of 92 Rc, transverse rupture stress of 3.4 MPa, and specific density of 14.5. The brass material is alloy 360 free-machining brass with 61.50% copper, 35.25% Zinc, and 3.25% lead. Relative to the carbide, brass is easy to EDM because of its good electrical conductivity and low melting temperature. The machine setup and process parameters for the cylindrical wire EDM experiment are listed in Table 2.1. Two parameters, the part rotational speed, ω , and wire feed rate, v_f , are varied in this study to investigate their effect on the cylindrical wire EDM of two different work-materials. Results of the maximum material removal rate are discussed below.

Table 2.1. Machine setup for the cylindrical wire EDM experiment.

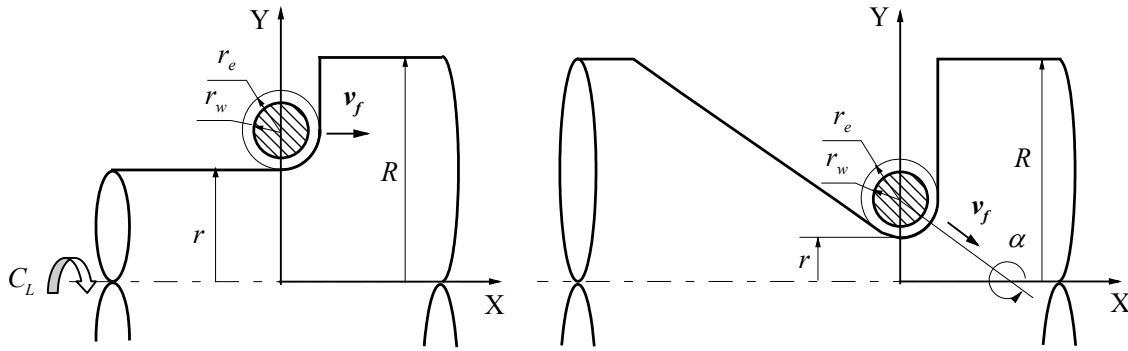
Wire EDM machine	Brother HS-5100	
Wire manufacturer	Charmilles Technologies, BercoCut	
Wire material	Brass	
Wire diameter (mm)	0.25	
Workpiece material	Brass	Carbide
Spark cycle (μs)	20	28
On-time (μs)	14	14
(Duty factor, On-time/Spark Cycle)	(70%)	(50%)
Axial direction wire speed (mm/s)	15	18
Wire tension (N)	14.7	14.7
Gap voltage (V)	45	35

The maximum material removal rate (MRR_{max}) is an important indicator of the efficiency and cost-effective of the process. Tests are designed to find the MRR_{max} in both the cylindrical and 2D wire EDM. Two test configurations to measure the MRR_{max} in cylindrical wire EDM are illustrated in Figs. 2.8(a) and 2.8(b). Two 2D wire EDM tests, as shown in Figs. 2.8(c) and 2.8(d), were also conducted on the same work-material to evaluate the difference in MRR_{max} .



(a) Cylindrical test I. (b) Cylindrical test II. (c) 2D test I. (d) 2D test II.
Fig. 2.8. Four test configurations to find the maximum material removal rate.

Key parameters of the two configurations to find the MRR_{max} in cylindrical wire EDM are shown in Fig. 2.9. In Fig. 2.9(a), α is set to 0 degree and v_f is gradually increased to the limiting speed, when the short circuit error occurs. This v_f is recorded as $v_{f,max}$ and the MRR_{max} can be calculated using Eq. (2.1). Another test configuration to measure MRR_{max} in cylindrical wire EDM, as shown in Fig. 2.9(b), has constant α and v_f . As the wire cuts into the workpiece, the material removal rate is gradually increased. At the position when the short circuit error occurs, the material removal rate is recorded as MRR_{max} . Two test configurations to find MRR_{max} for 2D wire EDM at different thickness are shown in Figs. 2.8(c) and 2.8(d). The v_f was gradually increased to find the MRR_{max} . Results of MRR_{max} are summarized in Tables 2.2 to 2.4.



(a) $\alpha = 0$ and gradually increasing v_f . (b) constant α and v_f .
Fig. 2.9. Key parameters of the two configurations to find the maximum material removal rate in cylindrical wire EDM.

Table 2.2. MRR_{max} for the cylindrical wire EDM test with $\alpha = 0$ and gradually increasing v_f .

Material	R (mm)	3.18			2.54	
	r (mm)	2.54	1.59	0.75	1.59	0.75
Brass	$v_{f,max}$ (mm/min)	5.72	2.69	2.13	5.33	3.46
	MRR_{max} (mm ³ /min)	65.2	64.1	63.7	65.7	64.0
Carbide	$v_{f,max}$ (mm/min)	1.42	0.81	0.66	1.55	1.02
	MRR_{max} (mm ³ /min)	16.2	19.3	19.7	19.1	18.9

Table 2.3. MRR_{max} for the cylindrical wire EDM test with constant α and v_f .

Material	v_f (mm/min)	α (degree)	-15	-30	-45
Brass	3.81	r_{min} (mm)	2.16	2.01	1.65
		MRR_{max} (mm ³ /min)	65.5	68.3	69.6
Carbide	1.02	r_{min} (mm)	2.02	1.95	1.17
		MRR_{max} (mm ³ /min)	19.1	18.7	20.9

Table 2.4. MRR_{max} for the 2D wire EDM test.

Material	Thickness (mm)	r_e (mm)	$v_{f,max}$ (mm/min)	MRR_{max} (mm ³ /min)
Brass	6.35	0.183	23.9	55.5
	3.23	0.183	37.8	44.7
Carbide	6.35	0.163	4.32	8.94
	3.23	0.163	8.00	8.42

Several observations can be extracted from the data in Tables 2.2 to 2.4.

1. The brass has much higher material removal rate than the carbide.
2. The MRR_{max} for cylindrical wire EDM in Tables 2.2 and 2.3 is greater than the 2D wire EDM results in Table 2.4. The possible cause may be better flushing conditions in the cylindrical wire EDM. In 2D wire EDM, as shown in Fig. 2.8(c), a narrow gap exists and affects the flow of high-pressure water jets for flushing. Such situation does not exist in the cylindrical wire EDM.
3. The MRR_{max} for 2D wire EDM changes slightly with thickness.
4. For carbide, the MRR_{max} may not be as high as that in rough grinding. However, this process does provide the advantage in flexibility to shape the workpiece.
5. The results from the two test configurations for cylindrical wire EDM at different sizes and angles are close to each other. The maximum material removal rate is calculated using the material removal rate model under various process setup parameters. This has verified the concept and mathematical model for the material removal rate.

Another important observation in this experiment is: the wire breakage is more likely to occur during cutting at a steeper angle α in the test configuration shown in Fig. 2.9(b).

2.6. Concluding Remarks

The feasibility of applying the cylindrical wire EDM process for high material removal rate machining of free-form cylindrical geometries was demonstrated in this study. The mathematical model for the material removal rate of cylindrical wire EDM of free-form surfaces was derived. Two experimental configurations designed to find the maximum material removal rates in cylindrical wire EDM were proposed. Results of each test configurations match each other. The maximum material removal rate for the cylindrical wire EDM was higher than that in 2D wire EDM of the same work-material. This indicates that the cylindrical wire EDM is an efficient material removal process.

The spindle was found to be a critical factor in achieving the desired roundness, surface finish, and material removal rate. The effect of spindle error on part roundness will be discussed in the following paper. Other refinements to enhance the spindle accuracy are required to achieve better cylindrical wire EDM results. One of the advantages of the cylindrical wire EDM process is its ability to machine micro-size shafts. Preliminary results indicated that a precision spindle is the key factor in the system for micro-machining applications.

References

- [1] Masuzawa, T., Fujino, M., Kobayashi, K., and Suzuki, T., 1985, "Study on Micro-Hole Drilling by EDM," *Bull. Japan Soc. of Prec. Eng.*, Vol. 20, No. 2, pp. 117-120.
- [2] Masuzawa, T., Fujino, M., Kobayashi, K., Suzuki, T., and Fujii, H., 1986, "Wire Electro-Discharge Grinding System for Machining Very Fine Rods," *International Conference on Computer-Aided Production Engineering, Edinburgh*, pp. 247-254.
- [3] Kuo, C.-L., Masuzawa, T., and Fujino, M., 1992, "High-Precision Micronozzle Fabrication," *IEEE Micro Electro Mechanical Systems '92, Travemunde Germany*, Feb. 4-7, pp.116-121.
- [4] Masuzawa, T., Kuo, C.-L., and Fujino, M., 1994, "A Combined Electrical Machining Process for Micronozzle Fabrication," *Annals of CIRP*, Vol. 43, pp.189-192.
- [5] Langen, H. H., Masuzawa, T., and Fujion, M., 1995, "Modular Method for Microparts Machining and Assembly with Self-Alignment," *Annals of CIRP*, pp. 173-176.
- [6] Sun, Xi-Qing, Masuzawa, T., and Fujino, M., 1996a, "Micro Ultrasonic machining and its Applications in MEMS," *Sensors and Actuators*, Vol. A57, pp. 159-164.
- [7] Sun, Xi-Qing, Masuzawa, T., and Fujino, M., 1996b, "Micro Ultrasonic Machining and Self-Aligned Multilayer Machining/Assembly Technologies for 3D Micromachines," *Proceedings of the IEEE Micro Electro Mechanical Systems (MEMS) 1996, Piscataway, NJ, USA*, pp. 312-317.
- [8] Masuzawa, T. and Tonshoff, H. K., 1997, "Three-Dimensional Micromachining by Machine Tools," *Annals of CIRP*, Vol. 46, pp. 621-628.
- [9] Yu, Z. Y., Masuzawa, T., and Fujino, M., 1998, "Micro-EDM for Three-Dimensional Cavities - Development of Uniform Wear Method," *Annals of CIRP*, Vol. 47, pp. 169-172.
- [10] Rajurkar, K. P. and Yu, Z. Y., 2000, "3D Micro-EDM Using CAD/CAM," *Annals of CIRP*, Vol. 49, pp. 127-130.
- [11] Slocum, A. H., 1992, *Precision Machine Design*, Prentice Hall.

CHAPTER 3. SURFACE INTEGRITY AND ROUNDNESS OF CYLINDRICAL WIRE ELECTRICAL DISCHARGE MACHINING

3.1. Introduction

The wire Electrical Discharge Machining (EDM) process removes the work-material by a series of electrical sparks between the workpiece and wire electrode. These sparks generate craters on the surface and recast layers and heat-affected zones on the sub-surface of the EDM workpiece. The surface integrity describes the mechanical, metallurgical, topological, and chemical conditions of the surface region. EDM surfaces are complicated. A comprehensive description of the surface integrity on EDM surfaces involves the measurement of surface roughness, depth of heat-affected zone, micro-hardness, size of surface crater, residual stresses, and endurance limit, etc. [1]. This study investigates the surface integrity and roundness of cylindrical wire EDM parts and explores possible ways to adjust process parameters to achieve better surface integrity and roundness.

Investigations have been carried out to analyze and improve the surface integrity of parts created by die-sinking EDM [2–5] and wire EDM [6–9]. In representative studies, the arithmetic average surface roughness, R_a , of the wire EDM processed workpiece was about 0.2 to 0.4 μm for tool steel [6] and 1.4 to 3.9 μm for metal matrix composites [9]. For the die-sinking EDM process, better surface finish has been reported. The R_a values could be achieved as low as 0.014 μm on silicon components [5] and 0.6 μm on titanium

carbide parts [4]. Researchers have demonstrated that better surface integrity can be achieved by optimizing the EDM process parameters [2, 4, 6, 8, 9]. For the cylindrical wire EDM process, effects of the new process parameters, such as part rotational speed, on the surface integrity and roundness are not known. A set of preliminary experiments was conducted to identify key process parameters that significantly affect the material removal rate and surface roughness. Two sets of experiments, in which these parameters are varied, were conducted to investigate their effects on material removal rate, surface integrity, and roundness of cylindrical wire EDM carbide and brass parts.

Scanning Electron Microscopy (SEM) has been a common tool to examine EDM surfaces [4, 7]. The EDM surface consists of small craters created by electrical sparks [1]. To improve the EDM surface integrity, the size of craters needs to be small. This study uses the SEM to examine and estimate the sizes of craters. Sub-surface depths of the recast layer and heat-affected zone are two other important characteristics of the EDM surface integrity. The SEM is used to examine the polished cross-section of EDM surfaces to quantify and compare sub-surface damage for various EDM process parameters and material removal rates.

In this paper, a mathematical model of the arithmetic surface roughness of an ideal cylindrical wire EDM surface is introduced in Section 2. Results of surface roughness and roundness measurements for two sets of experiments intended to produce for high material removal rate and fine surface roughness, respectively, are presented in Section 3. SEM micrographs of the surfaces and cross-sections of the sub-surfaces of cylindrical wire EDM carbide and brass parts are illustrated and discussed in Section 4.

3.2. Surface Finish Modeling

The cross-section of an ideal surface produced by the cylindrical wire EDM process consists of a series of circular arcs, as shown in Fig. 3.1. The real EDM surface finish is the combination of this ideal geometry and craters generated by sparks on the surface. The radius of the circular arc in the ideal surface, r_e , is equal to the radius of the wire, r_w , plus the gap between wire and workpiece. The same cross-section geometry can be found on surfaces machined by turning with a radius tool and by ball-end milling [10–16]. The peak to valley surface roughness, R_t , of the ideal surface with circular arcs has been studied [12, 13, 15, 16]. However, the closed-form analytical expression of the commonly used arithmetic average surface roughness, R_a , could not be found in literature. Only the approximation solution, which replaced the circular arc by a section of the parabolic curve, is available [15, 16]. The closed-form representation of the arithmetic average surface roughness, R_a , for an ideal surface consisting of circular arcs is derived in this study.

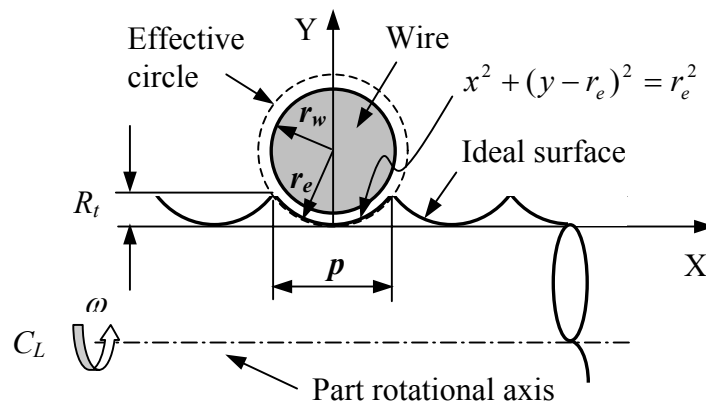


Fig. 3.1. Cross-section view of an ideal cylindrical wire EDM surface and the key parameters and coordinate system for mathematical modeling.

As shown in Fig. 3.1, after defining an XY coordinate system, one of the circular arcs on the surface can be expressed as:

$$x^2 + (y - r_e)^2 = r_e^2 \quad (3.1)$$

where

$$-\frac{p}{2} \leq x \leq \frac{p}{2} \quad (3.1a)$$

$$p = \frac{v_f \cos \alpha}{\omega} \quad (3.1b)$$

The pitch, p , as shown in Fig. 3.1, is a function of wire feed rate, v_f , workpiece rotation speed, ω , and wire traversing direction, α . The peak-to-valley surface roughness, R_t , of the ideal surface shown in Fig. 3.1 has been derived [15].

$$R_t = r_e - \sqrt{r_e^2 - \frac{p^2}{4}} \quad (3.2)$$

The arithmetic average surface finish, R_a , of the ideal surface is defined by the following formula:

$$R_a = \frac{1}{p} \int_{-p/2}^{p/2} |y - \bar{y}| dx \quad (3.3)$$

where

$$\bar{y} = \frac{1}{p} \int_{-p/2}^{p/2} y dx \quad (3.4)$$

Define $S(x)$ as follows:

$$S(x) = \int y dx = \int (r_e - \sqrt{r_e^2 - x^2}) dx = r_e x - \frac{1}{2} x \sqrt{r_e^2 - x^2} - \frac{1}{2} r_e^2 \arcsin\left(\frac{x}{r_e}\right) \quad (3.5)$$

Using $S(x)$, \bar{y} can be expressed as:

$$\bar{y} = \frac{2}{p} \int_0^{p/2} y dx = \frac{2}{p} [S(\frac{p}{2}) - S(0)] = \frac{2}{p} S(\frac{p}{2}) \quad (3.6)$$

Define another parameter x_c as the x coordinate where $y(x_c) = \bar{y}$.

$$x_c = \sqrt{2r_e \bar{y} - \bar{y}^2} \quad (3.7)$$

The analytical expression of arithmetic average roughness, R_a , can be expressed as:

$$R_a = \frac{2}{p} \left[\int_0^{x_c} (\bar{y} - y) dx + \int_{x_c}^{p/2} (y - \bar{y}) dx \right] = \frac{2}{p} \left[S\left(\frac{p}{2}\right) - 2 \cdot S(x_c) - \left(\frac{p}{2} - 2x_c\right) \cdot \bar{y} \right] \quad (3.8)$$

The extended closed-form solutions and their dimensionless expressions of surface roughness parameters for a theoretical profile consisting of elliptical or circular arcs will be presented in Chapter 4.

3.3. Experiments on Surface Finish and Roundness

Cylindrical wire EDM experiments were conducted to investigate the surface finish and roundness generated under different process parameters and to verify the surface finish model. The same work-materials, brass and carbide, as in the Chapter 2 are used in this study.

Two sets of experiments, designated as Experiments I and II, were designed. In Experiment I, the Material Removal Rate (MRR) was high. The wire feed rate and part rotational speed were varied to achieve different levels of surface roughness to verify the proposed surface finish model. In Experiment II, the goal was to adjust EDM process parameters to achieve the best possible surface finish and roundness. After conducting preliminary cylindrical wire EDM experiments, two process parameters, the pulse on-time and wire feed rate, were identified to have significant effects on surface finish.

Also, compared to Experiment I, the material removal rates were reduced significantly in Experiment II to achieve good surface finish and roundness. Key process parameters for Experiments I and II are listed in Table 3.1. The other process parameters remain the same as in the Chapter 2. Table 3.2 summarizes the *MRR* under different process parameters in Experiments I and II.

In Experiment I, four part rotation speeds and three wire feed rates were tested for cylindrical wire EDM of brass and carbide. In total, 24 experiments were conducted. The test configuration is illustrated in Fig. 3.2 with $\alpha = 0$, $R = 3.175$ mm, and $r = 2.54$ mm. As shown in Table 3.2, the maximum *MRR* was 13.9 and 52.1 mm³/min for carbide and brass, respectively. These are about 80% of the maximum *MRR* observed in [17].

In Experiment II, four pulse on-times and three wire feed rates were tested for brass and carbide. Similar to Experiment I, 24 tests were conducted. The cutting configuration shown in Fig. 3.2 with $\alpha = 0$, $R = 2.59$ mm, and $r = 2.54$ mm was used. A thin, 50 μ m layer of work-material was removed. This so called “skim cut” helps improve the surface finish. A small pitch of $p = 0.01$ mm was set for all tests in Experiment II to minimize surface roughness. To maintain the same pitch, the part rotational speeds, as shown in Table 3.2, were varied for different wire feed rates.

Table 3.1. Machine setup for the Experiments I and II.

Work-material	Experiment I (high <i>MRR</i>)		Experiment II (good surface finish)	
	Carbide	Brass	Carbide	Brass
Spark cycle (μs)	28	20	28	20
Pulse on-time (μs) [#]	14	14	2~5	2~5
(Duty factor)	(50%)	(70%)	(7~18%)	(10~25%)
Wire tension (N)	14.7	14.7	17.64	17.64
Gap voltage (V)	35	45	57	57
Wire feed rate v_f (mm/min) ^{+, #}	0.61, 0.91, 1.22	2.54, 3.81, 4.57	0.25, 0.375, 0.5	0.5, 1.0, 1.5
Part rotation speed ω (rpm) ⁺	10, 20, 30, 40	30, 60, 90, 120	25, 37.5, 50	50, 100, 150

⁺ denotes the set up parameters for Experiment I

[#] denotes the set up parameters for Experiment II

Table 3.2. Material removal rate of Experiments I and II.

Experiment	Work-material	Carbide			Brass		
	Experiment I (high <i>MRR</i>)	Pulse on-time (μs)	14			14	
Part rotational speed ω (rpm)		10, 20, 30, 40			30, 60, 90, 180		
Wire feed rate v_f (mm/min)		1.22	0.91	0.61	4.57	3.81	2.54
<i>MRR</i> (mm^3/min)		13.9	10.4	6.95	52.1	43.4	29.0
Experiment II (good surface finish)	Pulse on-time (μs)	2, 3, 4, 5			2, 3, 4, 5		
	Part rotational speed ω (rpm)	50	37.5	25	150	100	50
	Wire feed rate v_f (mm/min)	0.5	0.375	0.25	1.5	1.0	0.5
	<i>MRR</i> (mm^3/min)	5.70	4.28	2.85	17.1	11.4	5.70

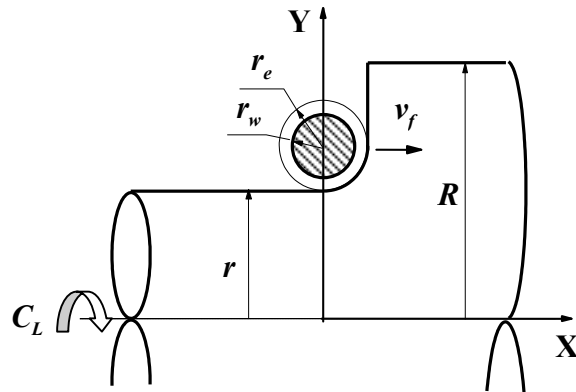


Fig. 3.2. The configuration of surface finish experiment.

3.3.1. Results of Experiment I

The surface finish and roundness of the 24 parts machined in Experiment I are shown in Fig. 3.3. The surface finish was measured using a Taylor Hobson Talysurf stylus profiler. The cutoff was set at 0.8 mm. Five cutoff lengths or 4 mm in total measuring length was used. The surface roughness parameter R_z (ISO standard), instead of R_t , was used to represent the peak-to-valley of the measured trace. R_z is defined as the distance between the average of the top five peaks and the average of the bottom five valleys on the filtered waviness trace. Since the 4 mm measuring range covers a large number (over 30) of peaks and valleys across an ideal surface shown in Fig. 3.1, R_z is a better indication than R_t for the true peak-to-valley value on the cylindrical wire EDM surface to avoid the misleading spikes of peak or valley in the measurement trace.

Three sets of data are presented in the surface roughness graphs in Fig. 3.3.

- *Ideal Surface Roughness:* For an ideal surface, the peak-to-valley surface roughness, R_t , is equal to R_z . Equations (3.2) and (3.8) are used to calculate R_z and R_a , respectively, of an ideal surface consisting of circular arcs. As shown in Fig. 3.3, higher part rotational speed and slower wire feed rate generate smaller pitch and lower R_a and R_z .
- *Measured Surface Roughness:* Results of the R_a and R_z on the 24 cylindrical wire EDM carbide and brass parts are shown in Fig. 3.3. The measured values of R_a and R_z are much higher than the ideal surface roughness due to the additional craters on the EDM surface. Slightly higher values of measured R_a and R_z were seen on parts machined at high rotational speeds. This contradicts the trend suggested in the ideal surface roughness equation. The possible cause is the vibration at higher spindle speed affects the surface roughness.
- *Combined Ideal and 2D Surface Roughness:* A set of 2D wire experiments was conducted on the same work-materials and under the same EDM process parameters as in Experiment I, except that the workpiece was stationary. Table 3.3 shows the measured R_a and R_z values of the 2D wire EDM carbide and brass parts under the same wire feed rate, v_f , as used in the cylindrical wire EDM experiments. The three dashed curves in Fig. 3.3 show results of the addition of the ideal and 2D surface roughness at three wire feed rates. These three curves have fairly good agreement with the three measured surface roughness curves. Although simply adding two surface roughness parameters to get the combined surface roughness lacks scientific

justification, results in Fig. 3.3 suggest a simple method to predict the roughness of cylindrical wire EDM surface. The SEM micrographs shown in following section reveal that cylindrical wire EDM surfaces do consist of both the ideal arc-shape in macro-scale and the surface craters and recast layer in the micro-scale.

Table 3.3. Surface finish of 2D wire EDM parts in Experiment I.

Work-material	Carbide			Brass		
v_f (mm/min)	1.22	0.91	0.61	4.57	3.81	2.54
R_a (μm)	1.80	1.45	1.46	2.89	2.59	2.34
R_z (μm)	11.6	9.23	9.27	18.0	16.7	14.6

The roundness of the machined parts was measured using the Mahr Formtester MMQ40 form measurement machine. Roundness results, ranging from 8 to 20 μm under high *MRR* conditions, are shown in Fig. 3.3. The results indicate that, in general, better roundness can be achieved at lower wire feed rate v_f . This is possibly due to less wire vibration. The effect of part rotational speed on roundness is not significant.

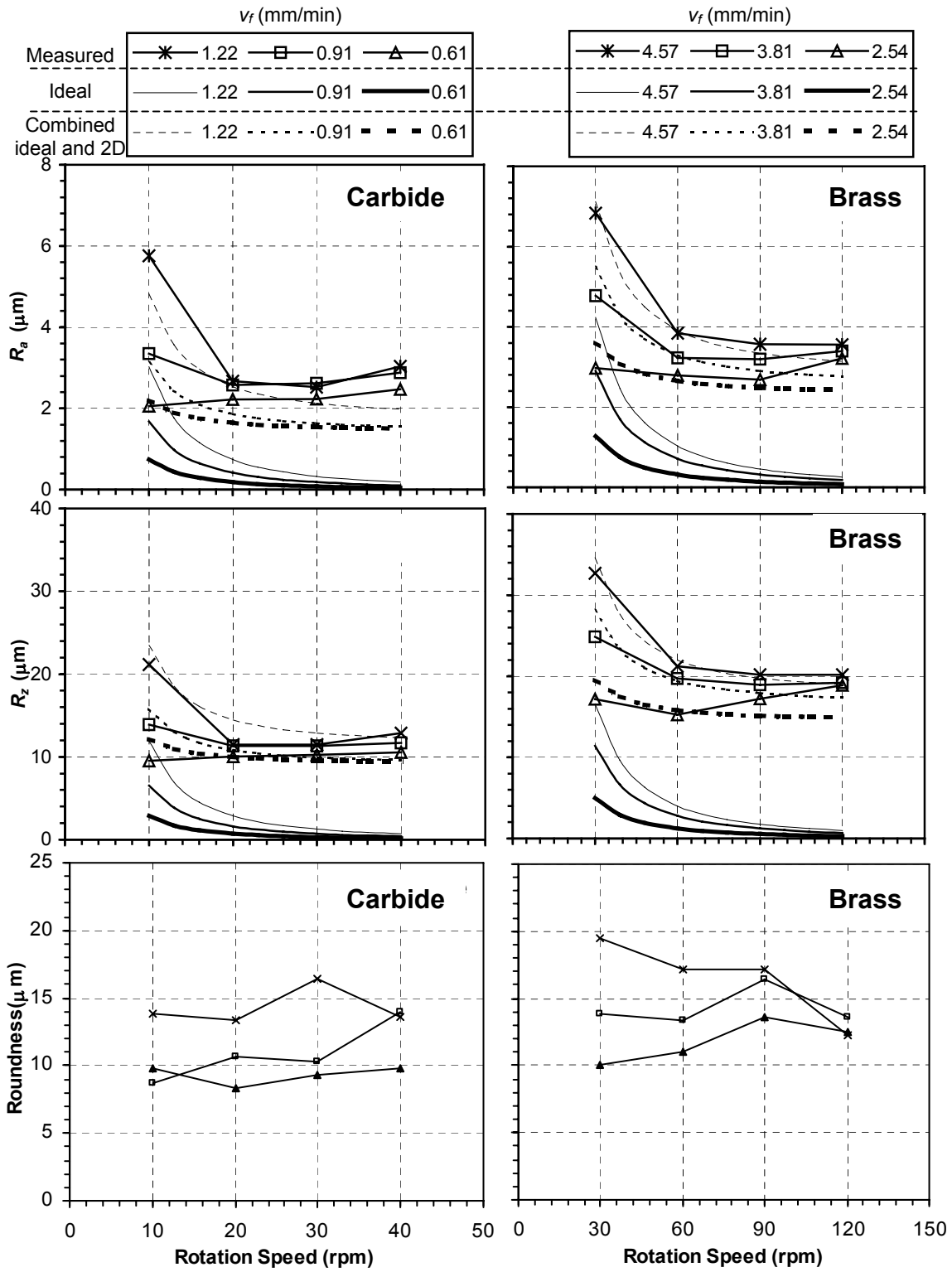


Fig. 3.3. The surface finish and roundness of cylindrical wire EDM parts in Experiment I with high material removal rate.

3.3.2. Results of Experiment II

The goal of experiment II was to achieve the best possible surface finish and roundness by adjusting two critical process parameters, the wire feed rate and pulse on-time. Figure 3.4 shows the surface finish and roundness results for Experiment II. Much better surface finish and roundness are observed in Experiment II. The shorter pulse on-time and lower feed rate, in general, created better surface finish and roundness. At the shortest pulse on-time, 2 μs , significant decreases in the surface roughness and roundness can be observed. Shorter pulse on-time generates smaller sparks, which, in turn, creates smaller craters and better surface finish. This can be verified in the SEM micrographs of EDM surfaces. The best R_a and roundness generated on carbide in this study are 0.68 and 1.7 μm , respectively. These values are comparable to that of rough grinding, which makes the cylindrical wire EDM process suitable for both high material removal rate and precision machining of the difficult-to-machine materials. However, this value is not as low as the 0.014 μm R_a surface roughness reported in EDM of silicon [5]. Better EDM machines could generate even lower surface roughness.

The 1.7 μm roundness at 2 μs pulse on-time are much smaller than the 6 to 9 μm spindle error presented in Fig. 2.5 of Chapter 2. The frequency spectrum of the spindle error presented in Fig. 2.6 of Chapter 2 is used to explain this observation. The f_o , the major peak of the spindle error at the frequency that is equal to the part rotational speed, is about 2.2 μm in amplitude or 4.4 μm in spindle error. This large off center error does not affect the roundness because the distance from the rotational axis to the wire remains

constant. The second peak of the spindle error, f_1 , at the frequency that is equal to five times the part rotational speed, is about $0.8 \mu\text{m}$ in amplitude or $1.6 \mu\text{m}$ in spindle error. This is identified as the main cause of the $1.7 \mu\text{m}$ roundness error on cylindrical wire EDM parts. The third and fourth peaks of the spindle error, f_2 and f_3 , remain at 60 and 120 Hz, respectively, independent of the spindle rotational speed. Since the standard 1-50 undulation per revolution filter was used in roundness measurement, the spindle error at these two high frequencies does not show up in the roundness results. In summary, only the f_1 peak of the spindle error spectrum affects the roundness results in low *MRR* cylindrical wire EDM conditions.

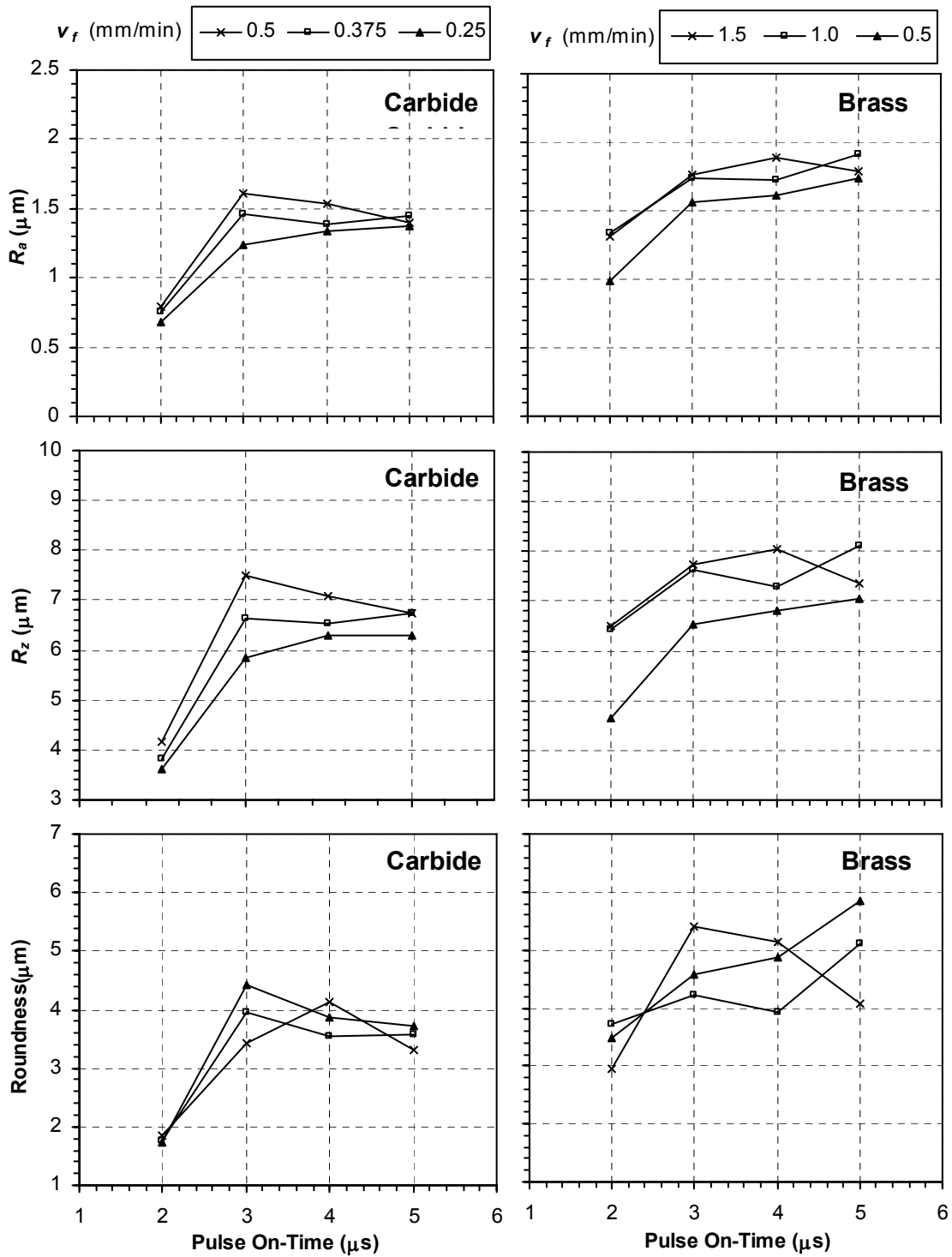


Fig. 3.4. The surface finish and roundness of cylindrical wire EDM parts in Experiment II with improvements on surface finish and roundness.

3.4. SEM Micrographs of EDM Surface and Sub-Surface

SEM is used to examine the surface and sub-surface of cylindrical wire EDM carbide and brass parts in Experiments I and II. The cylindrical samples were sliced in the radial direction. Surfaces of sliced cross-sections were polished to observe the sub-surface damage. The macro-ridges and craters on the surface and the recast layers and heat-affected zones in the sub-surface of the cylindrical wire EDM parts are presented in the following three sections.

3.4.1. Macro-ridges

Although regular EDM surfaces are isotropic and have no specific texture or pattern [1], cylindrical wire EDM surfaces may have macro-ridges, or circular arcs, in the cross-section. Figure 3.5 shows the surfaces of three cylindrical wire EDM brass parts in Experiment I with 30 rpm rotational speed and wire feed rates of 4.57, 3.81, and 2.54 mm/min. The corresponding pitches are 152, 127, and 84.7 μm . Similar macro-ridges exist on carbide parts. Figure 3.5 also shows the ideal surfaces that consist of circular arcs with the same p and r_e . These SEM micrographs also verify the surface finish model described in Section 2.

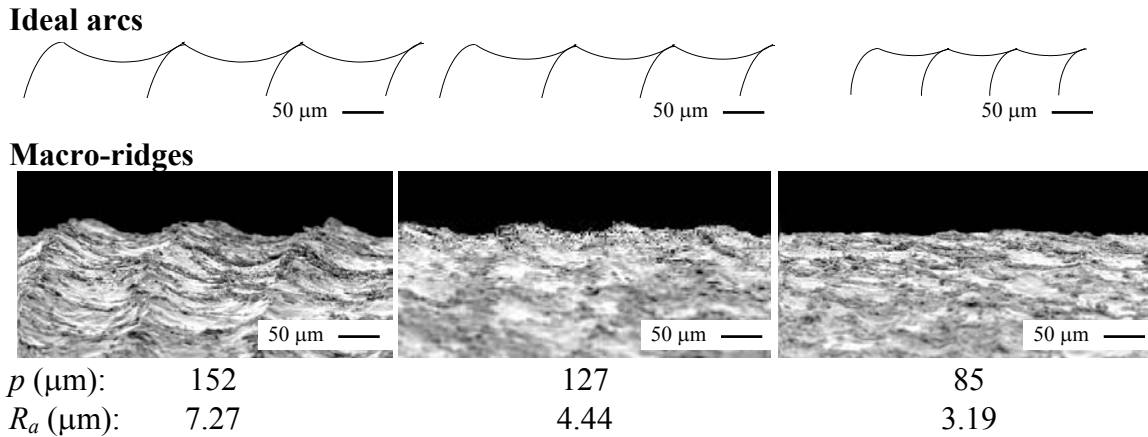
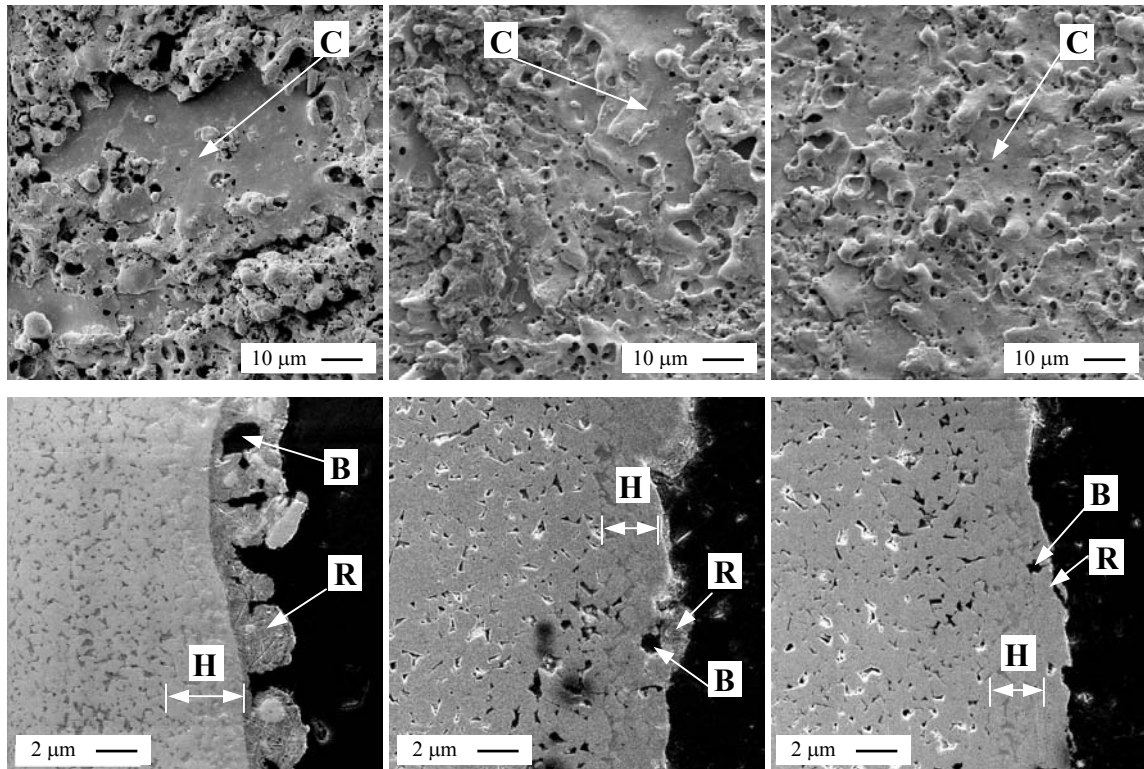


Fig. 3.5. SEM micrographs of macro-ridges and ideal arcs on surfaces of brass parts in Experiment I ($r_e=0.183$ mm).

3.4.2. Craters

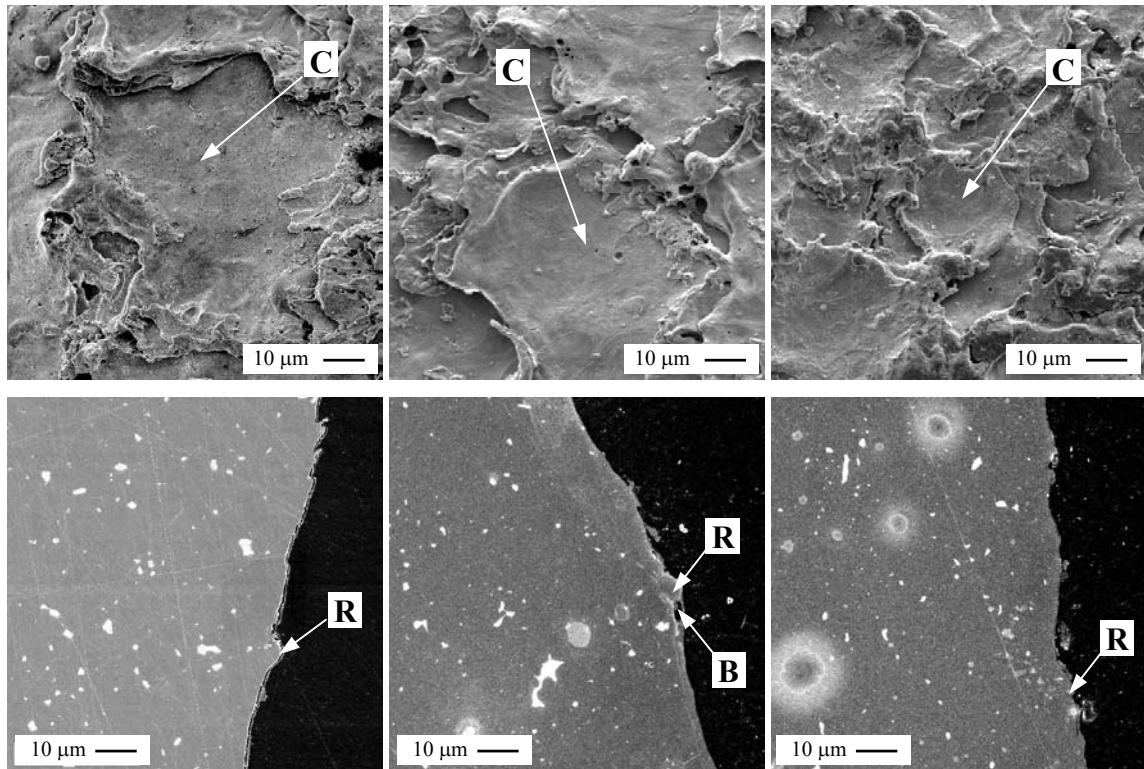
The rough surfaces in Experiment I and fine surfaces in Experiment II are observed using the SEM machine to compare the surface texture and crater size. As illustrated in the surface finish results in Fig. 3.4, the short, 2 μs , pulse on-time generates fine surface finish. Under shorter pulse on-time, electrical sparks generate smaller craters on the surface. For carbide parts, as shown in Fig. 3.6, the rough estimate of the crater size is about 50, 30, and 20 μm under 14, 5, and 2 μs pulse on-time, respectively. As shown in Fig. 3.7, slightly bigger craters, estimated as 60, 40, and 25 μm , can be seen on the brass parts machined under the same pulse on-time. On carbide parts, about 1 to 2 μm size tungsten carbide grain can be seen on the SEM micrographs in Fig. 3.6.



	Experiment I	Experiment II	Experiment II
R_a (μm):	2.53	1.40	0.68
On-time (μs):	14	5	2
ω (rpm):	30	50	25
v_f (mm/min):	1.22	0.5	0.25
MRR (mm^3/min):	13.9	5.70	2.85

Legend – C: Crater, R: Recast layer, B: Bubble, H: Heat affected zone.

Fig. 3.6. SEM micrographs of surfaces and cross-sections of carbide parts.



	Experiment I	Experiment II	Experiment II
R_a (μm):	3.19	1.78	0.98
On-time (μs):	14	5	2
ω (rpm):	30	150	50
v_f (mm/min):	2.54	1.5	0.5
MRR (mm^3/min):	29.0	17.1	5.70

Legend – C: Crater, R: Recast layer, B: Bubble.

Fig. 3.7. SEM micrographs of surfaces and cross-sections of brass samples.

3.4.3. Sub-surface recast layers and heat-affected zones

The recast layer is defined as the material melted by electrical sparks and resolidified on the surface without being ejected nor removed by flushing [2]. Below the recast layer is the heat-affected zone. For the carbide material, the cobalt matrix melts and resolidifies in the heat-affected zone. The molten cobalt fills the pores in the tungsten

carbide. This is observed in the SEM micrographs of the carbide cross-section and is used to identify the depth of heat-affected zone. Rajurkar and Pandit [18] have studied the recast layer and heat-affected zones of EDM surfaces and developed a thermal model to predict the thicknesses of damaged layers. For the die-sinking EDM process, the depth of the damaged layer was reported to be from 30 to 100 μm for an AISI 4130 steel workpiece machined with pulse on-time of 100 to 300 μs [4]. Anon [2] has studied the sub-surface heat-affected zones and recast layers of steel and tungsten carbide using the die-sinking EDM and have summarized and explained the possible causes for EDM surface defects.

SEM micrographs of the cross-section of carbide and brass parts machined under both high and low *MRRs* (Experiments I and II) are shown in Figs. 3.6 and 3.7. On carbide parts, the μm size carbide grains can be identified. The recast layer, bubbles in the recast layer, and heat affected zone of three carbide samples are identified in Fig. 3.6. Under high *MRR* at 14 μs pulse on-time, the recast layer, about 3 μm thick, can be clearly recognized on the surface. Thinner recast layers, less than 2 μm , exist on samples machined using shorter pulse on-time. Bubbles can be identified in the recast layers of all three carbide samples. Anon [2] has proposed that these micro-bubbles were generated by thermal stresses and tension cracking in the recast layer. As shown in Fig. 3.6, the depth of the heat-affected zone is estimated to be about 4, 3, and 2 μm on the three carbide samples with 14, 5, and 2 μs pulse on-time, respectively.

As shown in Fig. 3.7, very thin recast layers, about 1 μm , can be observed on the cross-section of three brass samples. No heat-affected zone can be recognized on brass samples, possibly due to the good thermal conductivity of brass. The heat-affected zone may exist but cannot be identified in brass samples. For carbide, the contrast of porosity filled by the molten cobalt makes the identification of the heat-affected zone easier. For brass material, such phenomenon does not exist. This has made the heat-affect zone difficult to be identified.

3.5. Concluding Remarks

The surface integrity and roundness of cylindrical wire EDM carbide and brass parts were investigated. A model with the closed-form solution of the arithmetic average surface roughness of the ideal surface generated by the cylindrical wire EDM process was derived and compared to two approximate solutions. Two sets of experiments, Experiments I and II, were conducted to identify the effects of part rotational speed, wire feed rate, and pulse on-time on the surface finish and roundness. Experiment I verified the surface finish model and found that simply adding the roughnesses of 2D wire EDM surfaces and ideal surfaces provided a good estimate of the surface roughness of cylindrical wire EDM parts. Experiment II demonstrated that good surface finish and roundness could be achieved in the cylindrical wire EDM process. The macro-ridges, surface craters, recast layers, and heat-affected zones were observed, and their sizes were estimated using the SEM.

In the study, all EDM experiments were conducted on a Brother HS-5100 wire EDM machine. Experimental results, such as material removal rate, surface roughness, and roundness, presented in this study may not be directly transferable to other wire EDM machines using different EDM power supply, wire, and tooling. Concepts presented in this study, including the quantification of maximum material removal rate, key process parameters to achieve fine surface finish and roundness, and thickness of recast layers and heat-affected zones, etc., can be applied for cylindrical wire EDM using other wire EDM machines on different types of work-materials.

References

- [1] Rajurkar, K. P. and Pandit, S. M., 1988, "Recent Progress in Electrical Discharge Machine Technology and Research," *Proceedings of Manufacturing International '88, Atlanta, GA, USA*, Vol. 1, pp. 219-226.
- [2] Anon, 1987, "Controlling EDM Surface Integrity," *American Machinist & Automated Manufacturing*, Vol. 131, No. 11, pp. 80-83.
- [3] Rajurkar, K. P. and Royo, G. F., 1988, "Improvement in EDM performance by R.F. Control and Orbital Motion," *ASME Symposium Volume on Research and Technological Developments in Non-traditional Machining*, PED-Vol. 34, pp. 51-62.
- [4] Rajurkar, K. P. and Royo, G. F., 1989, "Effect of R.F. Control and Orbital Motion on Surface Integrity of EDM Components," *Journal of Mechanical Working Technology*, Vol. 20, pp. 341-352.
- [5] Reynaerts, D., Meeusen, W., and Brussel, H. V., 1998, "Machining of Three-Dimensional Microstructures in Silicon by Electro-discharge Machining," *Sensors and Actuators*, Vol. A 67, pp. 159-165.
- [6] Liao, Y.S. and Woo, J.C., 1997, "The Effects of Machining Settings on the Behavior of Pulse Trains in the WEDM Process," *Journal of Materials Processing Technology*, Vol. 71, pp. 433-439.

- [7] Williams, R. E. and Rajurkar, K. P., 1991, "Study of Wire Electrical Discharge Machined Surface Characteristics," *Journal of Materials Processing Technology*, Vol. 28, pp. 127-138.
- [8] Ramulu, M., Jenkins, M. G., and Daigneanult, J. A., 1997, "Spark-Erosion Process Effects on the Properties and Performance of a TiB_2 Particulate-Reinforced/Sic Matrix Ceramic Composite," *Ceramic Engineering and Science Proceedings*, Vol. 18, No. 3, pp. 227-238.
- [9] Gatto, A. and Iuliano, L., 1997, "Cutting Mechanisms and Surface Features of WED Machined Metal Matrix Composites," *Journal of Materials Processing Technology*, Vol. 65, pp. 209-214.
- [10] Shaw, M. C. and Crowell, J. A., 1965, "Finishing Machining," *Annals of CIRP*, Vol. 13, pp. 5-22.
- [11] Nassirpour, F. and Wu, S. M., 1977, "Statistical Evaluation of Surface Finish and its Relationship to Cutting Parameters in Turning," *International Journal of Machine Tool Design & Research*, Vol. 17, pp.197-208.
- [12] Vajpayee, S., 1981, "Analytical Study of Surface Roughness in Turning," *Wear*, Vol. 70, pp. 165-175.
- [13] Shiraishi, M. and Sato, S., 1990, "Dimensional and Surface Roughness Controls in a Turning Operation," *Transactions of the ASME, Journal of Engineering for Industry*, Vol. 112, No. 1, pp. 78-83.
- [14] El-wardany, T., Elbestawi, M. A., Attia, M. H., and Mohamed, E., 1992, "Surface Finish in Turning of Hardened Steel," *Engineered surfaces, American Society of Mechanical Engineers, Production Engineering Division*, Vol. 62, pp. 141-159.
- [15] Whitehouse, D. J., 1994, *Handbook of Surface Metrology*, Institute of Physics, Bristol, Philadelphia.
- [16] Cheung, C. F. and Lee, W. B., 2001, "Characterization of Nanosurface Generation in Single-Point Diamond Turning," *International Journal of Machine Tools & Manufacture*, Vol. 41, No. 6, pp. 851-875.
- [17] Qu, J., Shih, A. J., and Scattergood, R., 2002, "Development of the Cylindrical Wire Electrical Discharge Machining Process, Part I: Concept, Design, and Material Removal Rate," *Journal of Manufacturing Science and Engineering* (accepted).
- [18] Rajurkar, K. P. and Pandit, S. M., 1984, "Quantitative Expressions for Some Aspects of Surface Integrity of Electro-Discharge Machined Components," *Transactions of ASME Journal of Engineering for Industry*, Vol. 106, No. 2, pp. 171-177.

CHAPTER 4. ANALYTICAL SURFACE ROUGHNESS PARAMETERS OF A THEORETICAL PROFILE CONSISTING OF ELLIPTICAL OR CIRCULAR ARCS

4.1. Introduction

Surface roughness parameters are used to characterize the finish and predict the functional performance of a surface [1-7]. Many researchers have investigated methods to measure and quantify the surface roughness and correlated the measurement results to component performances. De-Chiffre et al. [7] have reviewed the recent developments in surface metrology. In a recent study of the cylindrical wire EDM surface [8, 9], the theoretical profile of the machined surface was found to consist of small and repetitive circular arcs. Similar profiles exist on the surfaces of single-point diamond and traditional turning with a radius tool tip and on the surfaces machined by ball-end milling tools [10-22]. The theoretical surface profile with elliptical arcs, a more general case of circular arcs, can be generated in the flat-end milling process [23, 24]. In this study, three parameters of the surface consisting of elliptical and circular arcs, the peak-to-valley roughness R_t , arithmetic average roughness R_a , and root-mean-square roughness R_q , are investigated. These are three parameters commonly used to evaluate the surface roughness [2, 3, 5]. Among them, the peak-to-valley roughness R_t for a theoretical profile consisting of circular arcs has been well studied since the 1960s [6, 10-13, 17, 19, 22]. The approximate estimations of R_a for the theoretical profile formed by circular arcs have also been reported [23, 24]. However, based on the best of our knowledge, the

closed-form expressions of the R_a and R_q for a theoretical surface profile consisting of either elliptical or circular arcs have not been reported. One of the goals of this research is to derive the closed-form analytical expressions of these three roughness parameters, R_t , R_a , and R_q , for such ideal, theoretical surface profiles.

The real surface generated in machining processes and the profile measured by a surface finish measurement machine will be different from this theoretical surface profile. The tool wear, vibration of the tool during machining, elastic deformation and recovery of the tool and workpiece, build-up edge at tool tip, resolution of the measurement machine, etc. all create deviation from the theoretical surface profile. Formulas derived in this study are based purely on geometric consideration. This theoretical model can be used as prediction of the surface finish and comparison with the measured surface roughness values to investigate the influence of the work-material, tool behavior, cutting parameters, and other effects on the machined surface.

Formulas for these three closed-form surface roughness parameters are also arranged in dimensionless forms. A single dimensionless chart, which includes R_t , R_a , and R_q , can be used to present results for a wide range of theoretical surface profiles consisting of elliptical or circular arcs. Different tools, ranging from the sharp single-point diamond turning with 0.1 mm tool radius, to the conventional turning with 1 mm tool nose radius and to the ball end-milling with 5 mm tool radius, are used to generate the elliptical or circular arcs of various sizes.

There are several benefits and applications of such closed-form surface roughness parameters. First, it can be used for surface roughness prediction and evaluation in

CAD/CAM modeling of machining processes. Compared to the approximate solutions, the closed-form solution offers more accurate results for a wide range of process conditions. It is especially beneficial for precision machining processes, such as the single-point diamond turning and cylindrical wire EDM. Second, the dimensionless closed-form surface roughness parameters can be represented in a single chart to cover surface profiles consisting of a wide range of elliptical or circular arc sizes. Third, the closed-form solution can be used to evaluate different approximate solutions. The error analysis reveals the limitations and suitable ranges of approximate solutions.

In this paper, the closed-form expressions of the three roughness parameters R_t , R_a , and R_q for the theoretical surface profile consisting of elliptical arcs are first derived. The surface roughness parameters in dimensionless form are presented in Sec. 4.3. The closed-form solutions of R_t , R_a , and R_q for a theoretical profile with circular arcs, a special case of the elliptical arcs, are discussed in Sec. 4.4. In Sec. 4.5, two approximate solutions used to estimate the surface roughness parameters, R_t , R_a , and R_q , are derived and compared with the closed-form solutions.

4.2. Closed-form Expressions of Roughness Parameters for a Theoretical Surface Profile Consisting of Elliptical Arcs

Figure 4.1 illustrates a theoretical surface profile consisting of elliptical arcs. As shown in Fig. 4.1, a XY coordinate system is first defined. The elliptical arc on the surface profile can be expressed as

$$\frac{x^2}{a^2} + \frac{(y-b)^2}{b^2} = 1 \quad (4.1)$$

where a and b are the major and minor semi-axis of the elliptical arc, respectively, and

$$-\frac{f}{2} \leq x \leq \frac{f}{2} \quad (4.2)$$

The feed, f , as shown in Fig. 4.1, is the distance between two adjacent peaks of the surface profile. The closed-form expressions of three surface roughness parameters, R_t , R_a , and R_q , for this surface profile with elliptical arcs are derived in the following three sections. The derivation of three parameters, a , b , and f , for a measurement profile on the surface machined by flat-end milling is presented in Appendix B.

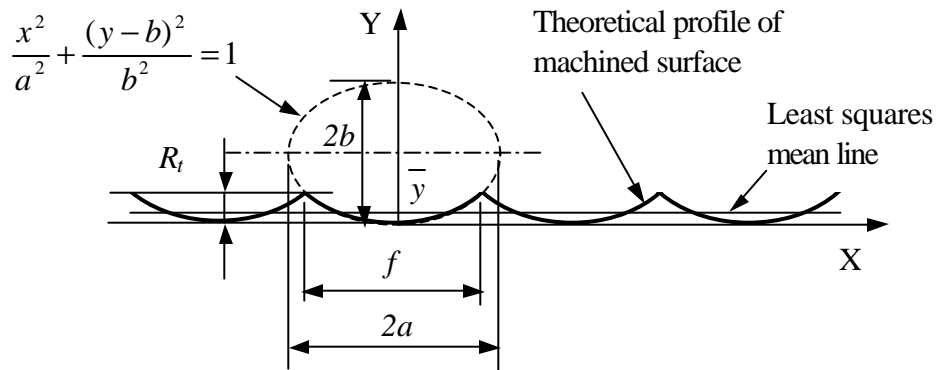


Fig. 4.1. A theoretical surface profile consisting of elliptical arcs.

4.2.1. Peak-to-valley roughness R_t

The peak-to-valley surface roughness, R_t , of the theoretical profile, as defined in Fig. 4.1, is

$$R_t = b - \frac{b}{a} \sqrt{a^2 - \frac{f^2}{4}} \quad (4.3)$$

4.2.2. Arithmetic average roughness R_a

According to ASME B46.1-1995 [25] and ISO 4287-1997 [26], the reference mean line in surface roughness is either the least squares mean line or filtered mean line. The least squares mean line is selected. The least squares mean line of this theoretical profile is a straight line parallel to the X-axis, $y = \bar{y}$. Based on the definition of least squares mean line,

$$\frac{\partial \int_{-f/2}^{f/2} (y - \bar{y})^2 dx}{\partial \bar{y}} = 0 \quad (4.4)$$

Thus,

$$\bar{y} = \frac{1}{f} \int_{-f/2}^{f/2} y dx \quad (4.5)$$

In order to simplify the expressions of \bar{y} , R_a , and R_q , a parameter $S(x)$ is first defined.

$$S(x) = \int y dx = \int \left(b - \frac{b}{a} \sqrt{a^2 - x^2} \right) dx = bx - \frac{b}{2a} x \sqrt{a^2 - x^2} - \frac{ab}{2} \arcsin\left(\frac{x}{a}\right) \quad (4.6)$$

Using $S(x)$, \bar{y} can be expressed as

$$\bar{y} = \frac{2}{f} \int_0^{f/2} y dx = \frac{2}{f} [S(\frac{f}{2}) - S(0)] = \frac{2}{f} S(\frac{f}{2}) \quad (4.7)$$

Define another parameter x_c as the x coordinate where $y(x_c) = \bar{y}$ on the theoretical profile.

$$x_c = \frac{a}{b} \sqrt{2b\bar{y} - \bar{y}^2} \quad (4.8)$$

The arithmetic average surface finish R_a is defined as

$$R_a = \frac{1}{f} \int_{-f/2}^{f/2} |y - \bar{y}| dx \quad (4.9)$$

For the theoretical surface profile consisting of elliptical arcs shown in Fig. 4.1, the closed-form expression of R_a can be derived and simplified with the three pre-defined parameters, x_c , \bar{y} , and $S(x)$.

$$R_a = \frac{2}{f} \left[\int_0^{x_c} (\bar{y} - y) dx + \int_{x_c}^{f/2} (y - \bar{y}) dx \right] = \frac{2}{f} [x_c \cdot \bar{y} - S(x_c)] \quad (4.10)$$

where x_c , \bar{y} , and $S(x_c)$ are functions of f .

4.2.3. Root-mean-square roughness R_q

The root-mean-square roughness, R_q , is defined as

$$R_q = \sqrt{\frac{1}{f} \int_{-f/2}^{f/2} (y - \bar{y})^2 dx} \quad (4.11)$$

The closed-form expression of R_q for the theoretical surface profile shown in Fig. 4.1 can be represented by

$$R_q = \sqrt{\frac{2}{f} \int_0^{f/2} (y^2 - 2y\bar{y} + \bar{y}^2) dx} = \sqrt{-\bar{y}^2 + 2b\bar{y} - \frac{f^2 b^2}{12a^2}} \quad (4.12)$$

Instead of using the above implicit form, another method using the parametric form to derive the closed-form solution of the surface roughness parameters are summarized in the Appendix C. These two methods give different expressions but same results for the three surface roughness parameters.

4.3. Roughness Parameters in Dimensionless Form

In this section, the dimensionless form expressions of three surface roughness parameters are presented. The three dimensionless parameters, R_t/b , R_a/b , and R_q/b , are expressed as functions of another dimensionless parameter, f/a , which ranges from 0 to 2. Using the dimensionless form, a single chart can be used to present the surface roughness results of theoretical surface profiles with a wide range of elliptical arc sizes. The derivation of dimensionless expressions of the three roughness parameters R_t , R_a , and R_q are discussed in the following three sections.

4.3.1. Peak-to-valley roughness R_t

Equation (4.3) is rearranged to present the dimensionless peak-to-valley roughness, R_t/b , as a function of f/a .

$$\frac{R_t}{b} = 1 - \sqrt{1 - \frac{1}{4} \left(\frac{f}{a} \right)^2} \quad (4.13)$$

Similar dimensionless expression for the theoretical surface profile consisting of circular arcs has been derived by Shaw and Crowell [12].

4.3.2. Arithmetic average roughness R_a

The $S(x_c)$, \bar{y} , and x_c in Eqs. (4.6), (4.7), and (4.8) are first rewritten as functions of the dimensionless parameter, f/a .

$$\bar{y} = \frac{2}{f} S\left(\frac{f}{2}\right) = b \cdot f_1\left(\frac{f}{a}\right) \quad (4.14)$$

$$x_c = \frac{a}{b} \sqrt{2b\bar{y} - \bar{y}^2} = a \cdot f_2\left(\frac{f}{a}\right) \quad (4.15)$$

$$S(x_c) = bx_c - \frac{b}{2a} x_c \sqrt{a^2 - x_c^2} - \frac{ab}{2} \arcsin\left(\frac{x_c}{a}\right) = ab \cdot f_3\left(\frac{f}{a}\right) \quad (4.16)$$

where

$$f_1\left(\frac{f}{a}\right) = 1 - \frac{1}{2} \sqrt{1 - \frac{1}{4} \left(\frac{f}{a}\right)^2} - \frac{a}{f} \arcsin\left(\frac{f}{2a}\right) \quad (4.17)$$

$$f_2\left(\frac{f}{a}\right) = \sqrt{2f_1\left(\frac{f}{a}\right) - f_1^2\left(\frac{f}{a}\right)} \quad (4.18)$$

$$f_3\left(\frac{f}{a}\right) = f_2\left(\frac{f}{a}\right) - \frac{1}{2} f_2\left(\frac{f}{a}\right) \sqrt{1 - f_2^2\left(\frac{f}{a}\right)} - \frac{1}{2} \arcsin\left(f_2\left(\frac{f}{a}\right)\right) \quad (4.19)$$

Substituting Eqs. (4.14) – (4.16) into Eq. (4.10), R_a / b can be expressed in the dimensionless form.

$$\frac{R_a}{b} = \frac{1}{b} \left[\frac{2}{f} (x_c \bar{y} - S(x_c)) \right] = f_a \left(\frac{f}{a} \right) \quad (4.20)$$

where

$$f_a \left(\frac{f}{a} \right) = 2 \frac{a}{f} \cdot \left[f_1 \left(\frac{f}{a} \right) f_2 \left(\frac{f}{a} \right) - f_3 \left(\frac{f}{a} \right) \right] \quad (4.21)$$

4.3.3. Root-mean-square roughness R_q

Substituting \bar{y} in Eq. (4.14) to Eq. (4.12), R_q / b can be expressed as

$$\frac{R_q}{b} = \frac{1}{b} \sqrt{-\bar{y}^2 + 2b\bar{y} - \frac{f^2 b^2}{12a^2}} = f_q \left(\frac{f}{a} \right) \quad (4.22)$$

where

$$f_q \left(\frac{f}{a} \right) = \sqrt{-f_1^2 \left(\frac{f}{a} \right) + 2f_1 \left(\frac{f}{a} \right) - \frac{1}{12} \left(\frac{f}{a} \right)^2} \quad (4.23)$$

Using Eqs. (4.13), (4.20), and (4.22), the three dimensionless surface roughness parameters, R_t / b , R_a / b , and R_q / b , vs. f/a are illustrated in Fig. 4.2. The chart is zoomed in at three different levels for small f/a values. To calculate R_t , R_a , and R_q for a theoretical surface profile consisting of elliptical or circular arcs, f/a is first calculated and

used to find the corresponding R_t/b , R_a/b , and R_q/b in Fig. 4.2. These three dimensionless values are then multiplied by b to find the value of surface roughness parameters, R_t , R_a , and R_q . Two examples are used to illustrate this procedure.

Example 1. Flat-end milling with 5 mm radius tool. Assume the major semi-axis a , minor semi-axis b , and feed f , equal 5, 2, and 2 mm, respectively, then $f/a = 0.4$. From Fig. 4.2, the corresponding $R_t/b = 0.0202$, $R_a/b = 0.0052$, and $R_q/b = 0.0060$. By multiplying $b = 2$ mm to these three dimensionless parameters, the R_t , R_a , and R_q , of this theoretical surface profile are 40.4, 10.4, and 12.0 μm , respectively.

Example 2. Single-point diamond turning with 0.1 mm radius tool. In this case, the theoretical surface profile is formed by circular arcs with $a = b = r = 0.1$ mm. Assume the feed $f = 0.008$ mm, the $f/a = 0.08$. From Fig. 4.2, the corresponding $R_t/b = 0.00080$, $R_a/b = 0.00021$, and $R_q/b = 0.00024$. By multiplying $b = 0.1$ mm to these three values, the surface roughness parameters, R_t , R_a , and R_q , of the theoretical surface profile are 0.80, 0.21, and 0.24 μm , respectively.

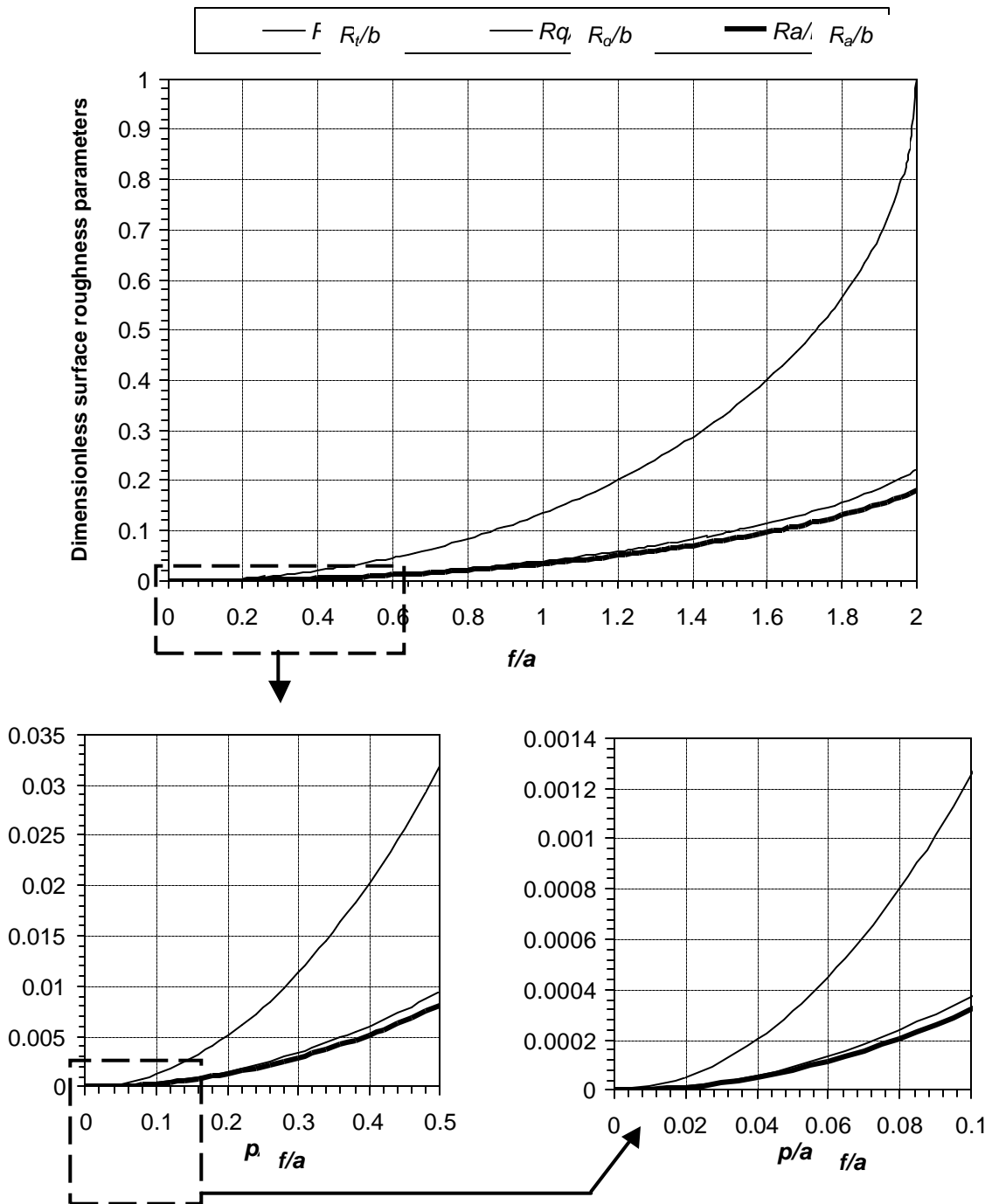


Fig. 4.2. Dimensionless surface roughness parameters R_f/b , R_a/b , and R_q/b vs. f/a .

4.4. Theoretical Surface Profile Consisting of Circular Arcs

Mathematically, the circular arc is a special case of the elliptical arc with $a = b = r$. Theoretical surface profiles consisting of circular arcs can be used to model the surface generated by turning with radius tools and milling with ball-end mills. The closed-form expressions of the three surface roughness parameters are derived in the following sections.

4.4.1. Peak-to-valley roughness R_t

By substituting a and b with r in Eq. (4.3), the closed-form expression of the peak-to-valley surface roughness, R_t , of a theoretical profile with circular arcs is

$$R_t = r - \sqrt{r^2 - \frac{f^2}{4}} \quad (4.24)$$

Equation (4.24) has been reported in references [6, 10, 12, 19].

4.4.2. Arithmetic average roughness R_a

The closed-form expression of the arithmetic average roughness R_a in Eq. (4.10) is still valid for the theoretical profile consisting of circular arcs. Substituting a and b by r in Eqs. (4.6) and (4.8), $S(x)$ and x_c can be expressed as

$$S(x) = \int y dx = \int (r - \sqrt{r^2 - x^2}) dx = rx - \frac{1}{2} x \sqrt{r^2 - x^2} - \frac{1}{2} r^2 \arcsin\left(\frac{x}{r}\right) \quad (4.25)$$

$$x_c = \sqrt{2r\bar{y} - \bar{y}^2} \quad (4.26)$$

The \bar{y} also has the same expression as in Eq. (4.7).

4.4.3. Root-mean-square roughness R_q

The root-mean-square roughness, R_q , of the theoretical profile consisting of circular arcs can be derived by substituting a and b with r in Eq. (4.12).

$$R_q = \sqrt{-\bar{y}^2 + 2r\bar{y} - \frac{f^2}{12}} \quad (4.27)$$

4.5. Approximate Solutions

Two approximate solutions of the three roughness parameters for the theoretical surface profile consisting of elliptical or circular arcs are presented. Two approximate solutions, one based on the parabolic approximation and another further simplified approximation, are derived. Results and comparisons to closed-form solutions are given in the following sections.

4.5.1. Approximations of the peak-to-valley roughness R_t

Assuming R_t is small and the higher order term R_t^2 can be neglected, the peak-to-valley roughness R_t of the theoretical profile consisting of elliptical arcs can be simplified to

$$R_t \cong \frac{f^2 b}{8a^2} \quad (4.28)$$

Substituting a and b by r in Eq. (4.28), the peak-to-valley roughness R_t of a theoretical surface profile consisting of circular arcs is

$$R_t \cong \frac{f^2}{8r} \quad (4.29)$$

Equation (4.29) has been reported in references [6, 11-13, 17, 19, 22]. Vajpayee [17] has compared the closed-form, Eq. (4.24), and simplified, Eq. (4.29), expressions of R_t for surface profile with circular arcs and indicated that the error would be high for a large f .

4.5.2. Approximations of the arithmetic average roughness R_a

In the past, the parabolic curve was used to approximate the elliptical or circular arcs to simplify the derivation of R_a . This is defined as the parabolic approximation. Assuming the surface profile consisting of parabolic curves with the same width (feed)

and height (minor semi-axis) as the elliptical arcs, the approximate R_a can be expressed as

$$R_a \cong \frac{4}{9\sqrt{3}} \left(b - \frac{b}{a} \sqrt{a^2 - \frac{f^2}{4}} \right) \quad (4.30)$$

When the R_a is small, Eq. (4.30) can be further simplified as

$$R_a \cong 0.032 \frac{f^2 b}{a^2} \quad (4.31)$$

This is defined as the simplified approximation.

For a theoretical surface profile with circular arcs, the parabolic approximation of R_a is

$$R_a \cong \frac{4}{9\sqrt{3}} \left(r - \sqrt{r^2 - \frac{f^2}{4}} \right) \quad (4.32)$$

A further simplification of Eq. (4.32) is the simplified approximation.

$$R_a \cong 0.032 \frac{f^2}{r} \quad (4.33)$$

Equation (4.33) is commonly used to estimate the R_a of a theoretical surface consisting of circular arcs, as reported in references [6, 22].

4.5.3. Approximations of the root-mean-square roughness R_q

The derivation of R_q can also be simplified by approximating the elliptical arcs by parabolic curves with the same feed and height. The parabolic approximation of R_q is

$$R_q \cong \frac{2}{3\sqrt{5}} \left(b - \frac{b}{a} \sqrt{a^2 - \frac{f^2}{4}} \right) \quad (4.34)$$

The further simplified form of Eq. (4.34) or the simplified approximation of R_q is

$$R_q \cong 0.037 \frac{f^2 b}{a^2} \quad (4.35)$$

For a theoretical profile consisting of circular arcs, the parabolic approximation of R_q is

$$R_q \cong \frac{2}{3\sqrt{5}} \left(r - \sqrt{r^2 - \frac{f^2}{4}} \right) \quad (4.36)$$

Based on Eq. (4.36), the simplified approximation of R_q is

$$R_q \cong 0.037 \frac{f^2}{r} \quad (4.37)$$

4.5.4. Comparison of the closed-form and approximate solutions

Results of the parabolic and simplified approximations of R_t , R_a , and R_q , comparing to the closed-form solution, are shown in Fig. 4.3. The parabolic approximations overestimate and the simplified approximations underestimate the closed-form solution. More significant errors can be seen at higher f/a . This indicates that both approximate solutions have good estimations at small f/a . When $f/a < 0.5$, both approximation methods gives satisfactory estimations. Replacing a and b by r , Fig. 4.3 can be used for the theoretical surface with circular arcs. For turning with a radius tool, $f/r < 0.5$ occurs when the feed, f , is smaller than the half tool radius, $r/2$.

Table 4.1 shows more detailed error analysis results for four different values of f/a . Under the worst case, when $f/a = 2$, the error is 41.5% and 33.6% for the parabolic approximation of R_a and R_q and 50.0%, 29.4%, and 33.2% for the simplified approximation of R_t , R_a and R_q , respectively. Very small error, less than 0.33% for the parabolic approximation and 1.6% for the simplified approximation, can be seen when $f/a = 0.5$. This indicates that the approximation solutions do provide good estimations of the surface roughness parameters when $f/a < 0.5$.

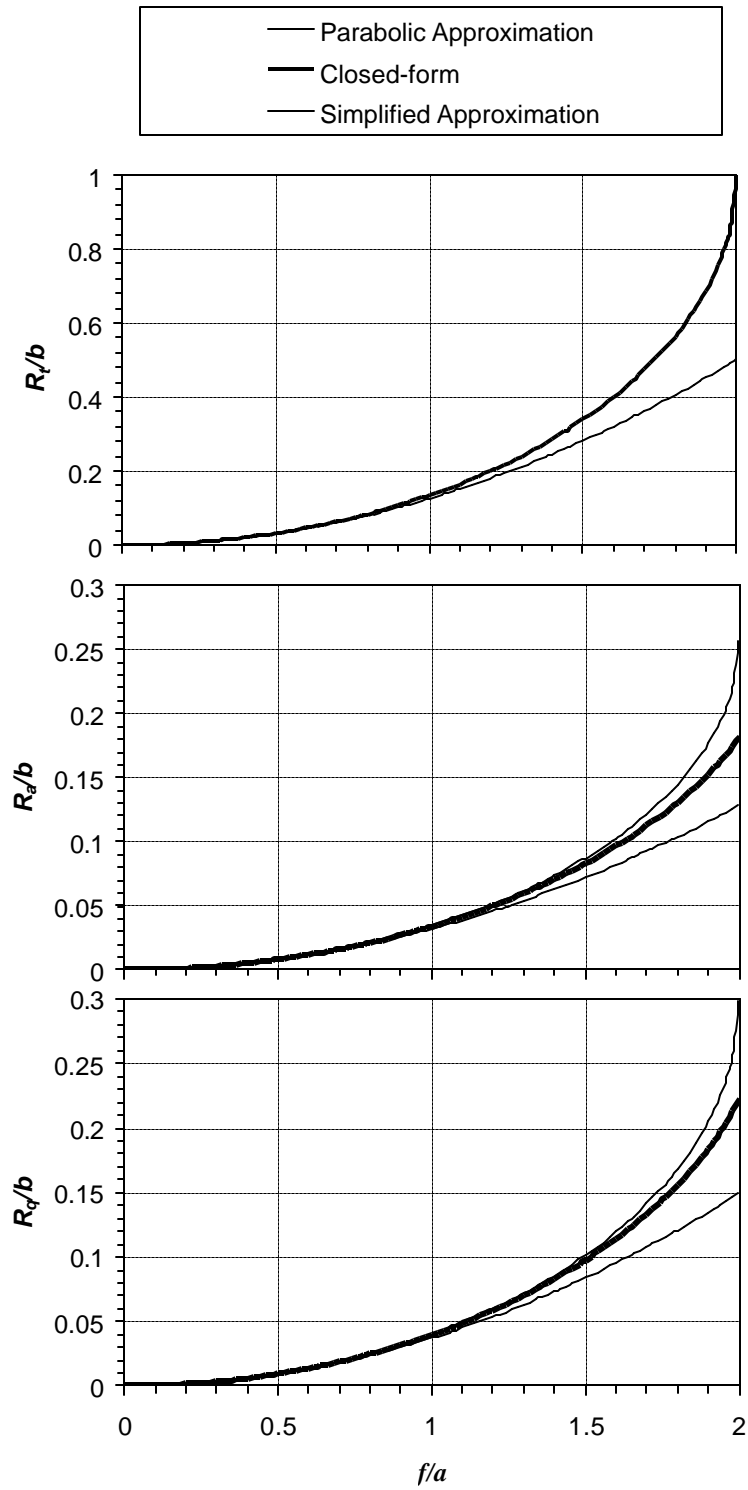


Fig. 4.3. Comparison of closed-form and approximate solutions of surface finish parameters.

Table 4.1. Error analysis of approximate solutions.

f/a	Error (%)				
	Parabolic approximation (overestimate)		Simplified approximation (underestimate)		
	R_a	R_q	R_t	R_a	R_q
0.5	0.33%	0.23%	1.59%	1.50%	1.35%
1	1.53%	1.09%	6.70%	5.50%	5.67%
1.5	4.82%	3.47%	16.93%	13.13%	14.04%
2	41.53%	33.58%	50.00%	29.40%	33.21%

4.6. Concluding Remarks

The closed-form solutions of surface finish parameters, R_t , R_a , and R_q , for the theoretical profile of a machined surface consisting of elliptical or circular arcs were derived. It offers accurate surface roughness evaluation for a wide range of process conditions and can be used in CAD/CAM systems for machining process modeling. Both the implicit and parametric forms are applied to derive the closed-form solutions. The dimensionless form of surface roughness parameters, R_t , R_a , and R_q , were also presented. Two approximation solutions, parabolic approximation and simplified approximation, were defined and developed to estimate the surface roughness parameters. Limitations of these approximate solutions were investigated. The comparison of the closed-form and approximate solutions showed that the parabolic approximation overestimated and the simplified approximation underestimated the surface roughness parameters. When f/a is smaller than 0.5, both approximation solutions have good estimation of R_t , R_a , and R_q .

Although a detailed survey was conducted to investigate previous research in this subject, it is still possible that other researchers could have investigated this basic problem, perhaps in different format and other approaches. The goal of this study is to present a complete derivation of the closed-form solution from two different approaches and to provide a detailed comparison with two approximation solutions.

References

- [1] Vajpayee, S., 1973, "Functional Approach to Numerical Assessment of Surface Roughness," *Microtecnic*, Vol. 27, pp. 360-361.
- [2] Peters, J., Vanherck, and Sastrodinoto, M., 1979, "Assessment of Surface Typology Analysis Techniques," *Annals of CIRP*, Vol. 28/2, pp. 539-554.
- [3] Thomas, T. R., 1981, "Characterization of Surface Roughness," *Precision Engineering*, Vol. 3, pp. 97-104.
- [4] Nowicki, B., 1981, "Investigation of the Surface Roughness Range," *Annals of CIRP*, Vol. 30, pp. 493-497.
- [5] Malburg, M. C., Raja, J., and Whitehouse, D. J., 1993, "Characterization of Surface Texture Generated by Plateau honing Process," *Annals of CIRP*, Vol. 42, No. 1, pp. 637-639.
- [6] Whitehouse, D. J., 1994, *Handbook of Surface Metrology*, Institute of Physics, Bristol, Philadelphia.
- [7] De-Chiffre, L., Lonardo, P., Trumpold, H., Lucca, D. A., Goch, G., Brown, C. A., Raja, J., and Hansen, H. N., 2000, "Quantitative Characterization of Surface Texture," *Annals of CIRP*, Vol. 49, No. 2, pp. 635-652.
- [8] Qu, J., Shih, A.J., and Scattergood, R., 2001 "Development of the Cylindrical Wire Electrical Discharge Machining Process," *Symposium on Nontraditional Manufacturing Research and Applications*, Proceedings of 2001 ASME International Mechanical Engineering Congress and Exposition, Vol. 3, IMECE2001/MED-23343, Nov. 11-16, New York.

- [9] Qu, J., Shih, A.J., and Scattergood, R., 2002, "Development of the Cylindrical Wire Electrical Discharge Machining Process, Part II: Surface Integrity and Roundness," *ASME Journal of Manufacturing Science and Engineering* (accepted).
- [10] Lambert, H. J., 1961-1962, "Two Years of Finish-Turning Research at the Technological University, Delft," *Annals of CIRP*, Vol. 10, pp. 246-255.
- [11] Sata, T., 1964, "Surface Finish in Metal Cutting," *Annals of CIRP*, Vol. 7, pp. 190-197.
- [12] Shaw, M. C. and Crowell, J. A., 1965, "Finishing Machining," *Annals of CIRP*, Vol. 13, pp. 5-22.
- [13] Olsen, K. V., 1968, "Surface Roughness on Turned Steel Components and the Relevant Mathematical Analysis," *The Production Engineer*, pp. 593-606.
- [14] Wallbank, J., 1979, "Surfaces Generated in Single-Point Diamond Turning," *Wear*, Vol. 56, pp. 391-407.
- [15] Hasegawa, M., Seireg, A., and Lindberg, R. A., 1976, "Surface Roughness Model for Turning," *Tribology International*, Vol. 9, pp. 285-289.
- [16] Nassirpour, F. and Wu, S. M., 1977, "Statistical Evaluation of Surface Finish and its Relationship to Cutting Parameters in Turning," *International Journal of Machine Tool Design & Research*, Vol. 17, pp. 197-208.
- [17] Vajpayee, S., 1981, "Analytical Study of Surface Roughness in Turning," *Wear*, Vol. 70, pp. 165-175.
- [18] Sata, T., Li, M., Takata, S., Hiroaka, H., Li, C. Q., Xing, X. Z., and Xiao, X. G., 1985 "Analysis of Surface Roughness Generation in Turning Operation and Its Applications," *Annals of CIRP*, Vol. 34, pp. 473-476.
- [19] Shiraishi, M. and Sato, S., 1990, "Dimensional and Surface Roughness Controls in a Turning Operation," *Transactions of the ASME, Journal of Engineering for Industry*, Vol. 112, No. 1, pp. 78-83.
- [20] El-wardany, T., Elbestawi, M. A., Attia, M. H., and Mohamed, E., 1992, "Surface Finish in Turning of Hardened Steel," *Engineered surfaces, American Society of Mechanical Engineers, Production Engineering Division*, Vol. 62, pp. 141-159.
- [21] Salsbury, J. G. and Raja, J., 1995, "Quantitative Metrology for Process Capability Analysis of Turning Centers," *Proceedings of the NAMRC XXIII*, Society of Manufacturing Engineers, p. 6.

- [22] Cheung, C. F. and Lee, W. B., 2001, "Characterization of Nanosurface Generation in Single-Point Diamond Turning," *International journal of machine tools & manufacture*, Vol. 41, No. 6, pp. 851-875.
- [23] Lee, Y. S. and Chang, T. C., 1996, "Machined Surface Error Analysis for 5-axis Machining," *International Journal of Production Research*, Vol. 34, No. 1, pp. 111-135.
- [24] Lee, Y. S., 1998, "Mathematical Modeling of Using Different Endmills and Tool Placement Problems for 4-and 5-axis NC Complex Surface Machining," *International Journal of Production Research*, Vol. 36, No.3, pp. 785-814.
- [25] ASME B46.1-1995 Surface Texture – Surface Roughness, Waviness, and Lay, 1995.
- [26] ISO 4287-1997 Geometrical Product Specifications (GPS) – Surface Texture: Profile Method – Terms, Definitions, and Surface Texture Parameters, 1997.

CHAPTER 5. NANOINDENTATION CHARACTERIZATION OF SURFACE LAYERS OF ELECTRICAL DISCHARGE MACHINED WC-CO

5.1. Introduction

MMC materials are widely used because of their outstanding hardness, wear resistance, and strength. However, the MMCs are difficult to machine by conventional processes due to the high hardness and toughness. Alternatively, EDM process has been used extensively to manufacture the MMC components [1–4]. Although EDM can machine precise, complex, and intricate MMC components, the surface recast layer and subsurface heat-affected zone are generated [5]. The surface integrity, including roughness, size of craters, and depth of recast layer and heat-affected zone, on cylindrical wire EDM WC-Co surface has been investigated [2]. This study applies nanoindentation, EDS X-ray, and X-ray diffraction methods to further study the mechanical properties (hardness and modulus of elasticity) and material compositions of the WC-Co surface layers machined by the cylindrical wire EDM process.

Indentation has been widely used as an experimental tool to probe the hardness and modulus of materials by means of load-displacement behavior. Nanoindentation applies very small load, at the μN level, to the specimen and generates indentation depths in the sub- μm or nm scale [6]. This makes nanoindentation suitable and effective in measuring mechanical properties of thin films and small volumes of material and the microstructure and mechanical properties of MMCs [7–12]. The thickness of EDM recast layer and

heat-affected zone is usually very thin [2–4]. For example, as shown in Fig. 3.6 in Chapter 3, the thickness of EDM surface layers is less than 3 μm . It is difficult to use conventional methods to measure and distinguish the mechanical properties of EDM surface layers. Llanes et al. [3] has used the microscratch tests to characterize the sliding contact response of the wire EDM WC-Co surfaces. In this study, the nanoindentation method is applied. In the following section, the experiment setup and sample preparation are introduced. Experimental results and discussions are then presented in Sec. 5.3.

5.2. Experiment Setup and Sample Preparation

In the past two decades, the nanoindentation method with continuous load-displacement sensing has been developed and applied by researchers to measure mechanical properties of thin films and surface layers. The hardness, H , and modulus of elasticity, E , can be calculated using the following formulas.

$$H = \frac{P_{\max}}{A} \quad (5.1)$$

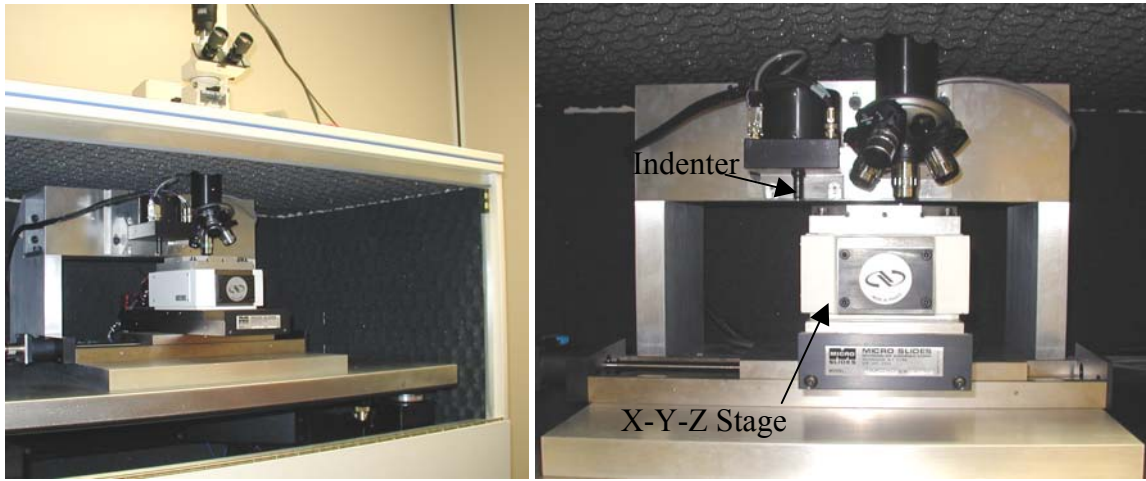
$$E_r = \frac{\sqrt{\pi}}{2} \frac{S}{\sqrt{A}} \quad (5.2)$$

$$\frac{1}{E_r} = \frac{(1-\nu^2)}{E} + \frac{(1-\nu_i^2)}{E_i} \quad (5.3)$$

where P is the indentation load and P_{max} is the peak indentation load, h is the displacement of the indenter, A is the projected area of the hardness impression, S ($=dP/dh$) is the contact stiffness, ν is the Poisson's ratio of the work-material, E is the modulus of elasticity of the work-material, and E_r is the reduced modulus of elasticity with consideration of the effect of non-rigid indenters. E_i and ν_i are the modulus of elasticity and Poisson's ratio of the indenter, respectively.

In this study, the continuous stiffness measurement method was used to obtain the contact stiffness, S . Details of this technique and analysis procedure are described in [6,13,14]. The displacement control was used in the nanoindentation experiment and the load was dependent on the indenter penetration depth. The hardness and modulus of elasticity were calculated from the load-displacement curves.

The nanoindentation experiments were conducted at the Oak Ridge National Lab on a MTS Nano-indenter™ II with the Berkovich diamond indenter, as shown in Fig. 5.1. The machine was operated to measure the thin surface layers of WC-Co after EDM. A precision X-Y table with a calibrated distance from the indenter to an optical microscope was used for accurate positioning of indents.



(a) Front-side view.

(b) Close view.

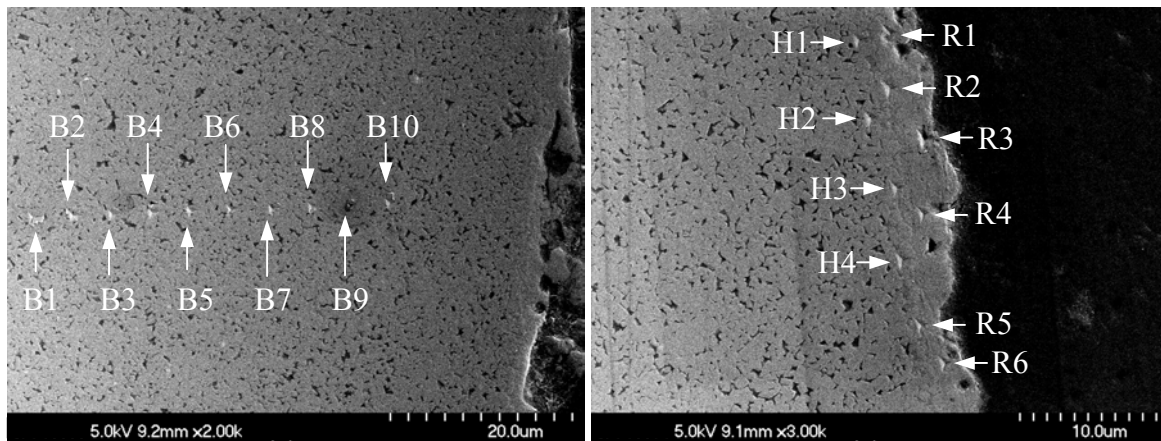
Fig. 5.1. MTS Nano-indenter™ II.

The WC-Co composite used in this study consists of WC particles about 1 μm size with a volume fraction of 10% cobalt matrix. The SEM micrographs in Fig. 3.6 in Chapter 3 show the surfaces and cross-sections of three WC-Co parts machined by cylindrical wire EDM. The sample machined by 5 μs pulse on-time was selected for the nanoindentation and other material characterization study. Cross-section of the EDM surface was used for the nanoindentation test.

5.3. Experimental Results and Discussion

In the experiment, multiple indents were performed on the cross-section of the bulk material, heat-affected zone, and recast layer of the WC-Co part machined by cylindrical wire EDM. Examples of three sets of nano-indents are shown in Fig. 5.2. The ten nano-indents in the bulk material are marked by B1 to B10 in Fig. 5.2(a). Four nano-indents in

the heat-affected zone are labeled by H1 to H4 in Fig. 5.2(b). R1 to R6 are the six nano-indentations on the recast layer.



(a) Nano-indentations in bulk material.

(b) Nano-indentations on recast layer and heat-affected zone.

Fig. 5.2. Nanoindentation on the cross-section of WC-Co part machined by cylindrical wire EDM.

The measured hardness and modulus of elasticity of the 14 sample nano-indentations from each of the three regions (bulk material, heat-affected zone, and recast layer) are presented in Table 5.1. These data are arranged in the descending order of the measured hardness. Relatively large variations of both the measured hardness and modulus of elasticity are observed in all three regions. The porosity, soft cobalt matrix, cracks, and defects within three regions contribute to such large discrepancy in measured hardness. This will be further illustrated by SEM micrographs of sample nano-indentations in each of three regions in the following three sections.

Table 5.1. Hardness and modulus of elasticity of bulk material, heat-affected zone, and recast layer in descending order of the hardness. (Unit: GPa)

Bulk material			Heat-affected zone			Recast layer		
Hardness	Modulus		Hardness	Modulus		Hardness	Modulus	
19.7	497		21.0	434		17.3	283	
19.3	496	B5	20.4	515	H4	16.6	328	
17.4	514	B4	19.9	377		16.4	318	R5
17.4	479	B10	19.3	438		16.4	312	R6
16.5	453		18.5	317		15.1	235	
16.2	493	B3	18.2	440		15.0	323	
13.9	417	B6	18.1	379	H3	14.5	411	R2
13.8	462	B8	17.9	392		13.4	363	
13.2	477	B7	16.5	452		13.2	286	
12.3	477	B1	16.4	318		12.7	198	
11.6	401	B2	16.1	386	H1	11.2	189	
10.8	433	B9	15.2	354		10.9	352	R4
7.7	238		15.0	394	H2	7.4	294	R1
7.6	395		15.0	323		5.6	191	R3



Regular nano-indentations



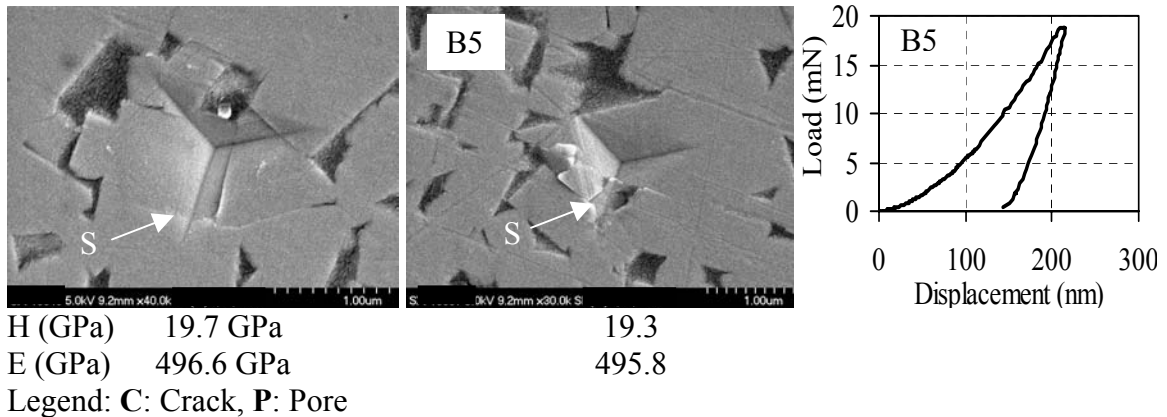
Irregular nano-indentations

5.3.1 Bulk Material

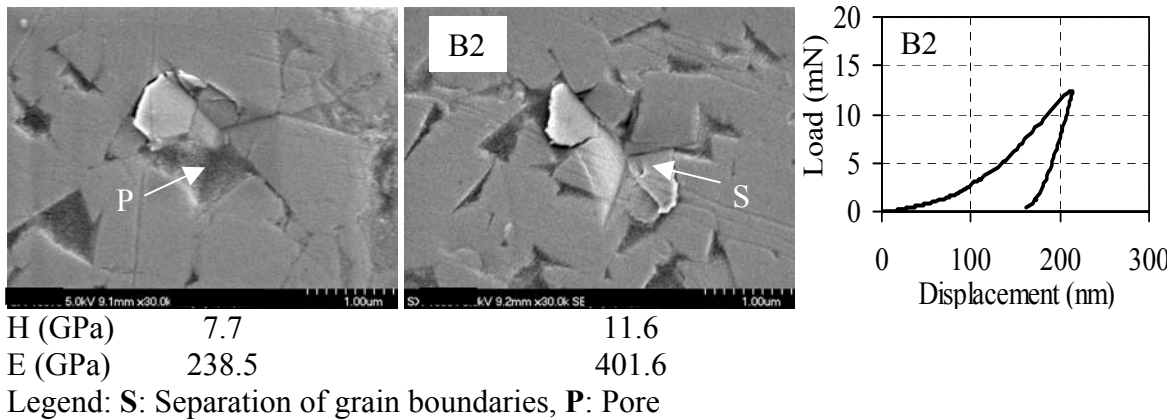
The porosity and soft Co matrix surround the hard WC grain can be identified on the cross-sectional SEM micrographs of the EDM surface of WC-Co. For the 14 nano-indentations in the bulk material listed in Table 5.1, the measured hardness varied between 7.6 and 19.7 GPa and the modulus of elasticity ranged from 239 to 514 GPa. These indentations were observed using the SEM individually and then separated into two groups: regular and irregular nano-indentations. The irregular nano-indentations have pores and/or separation of grain boundaries on the indent area and show, in general, lower hardness and modulus of elasticity.

SEM micrographs of two sample nano-indentations from each group are shown in Fig. 5.3. One sample load-displacement curve for one of the nano-indentations in each set of frames is also shown in Fig. 5.3.

- Regular nano-indentations. Figure 5.3(a) shows the two regular nano-indentations located on the WC particles. The measured hardness values are 19.7 and 19.3 GPa, respectively. This level hardness is comparable to the 18 GPa of WC reported in [12]. In contrast to irregular indentations, which hit pores or generated separation of grain boundaries, these two indented areas had only minor damage on the outside edges.
- Irregular nano-indentations. Two sample irregular nano-indentations are shown in Fig. 5.3 (b). A large portion of the indentation with 7.7 GPa hardness was on a pore. The indentation with 11.6 GPa hardness had significant separation of grain boundaries around the center, possibly due to a pore underneath the surface. For these two irregular indentations, the contact area was difficult to define because of the morphology, which resulted in a decay of measured hardness and modulus.



(a) Regular Nano-indentations.



(b) Irregular Nano-indentations.

Fig. 5.3. Nanoindentation on the bulk material.

5.3.2 Heat-Affected Zone

The heat-affected zone is between the recast layer and bulk material. For the WC-Co composite, the Co melted and resolidified in the heat-affected zone during the EDM spark erosion and filled the pores between the WC particles. As shown in Fig. 5.4, this can be observed in SEM micrographs of the WC-Co cross-section and has been used to identify the depth of heat-affected zone. The thickness of heat-affected zone in this sample is about 1–2 μm.

Unlike nano-indentations in the bulk material, separation of grain boundaries rarely occurred on nano-indentations in the heat-affected zone. It is probably due to the Co filled in pores and gave more consistent support to the WC particles. Variations of measured hardness and modulus of elasticity in the heat-affected zone are lower than those in the bulk material and recast layer. The measured hardness varies between 15.0 and 20.4 GPa, and the modulus of elasticity ranges from 323 to 515 GPa.

The nano-indentations in the heat-affected zone can also be grouped into regular nano-indentations and irregular nano-indentations.

- Regular nano-indentations. Figure 5.4 (a) shows two regular nano-indentations with hardness of 20.4 and 18.1 GPa. Similar to the regular nano-indentations in bulk material, no pore or separation of grain boundaries is close to the center of the nano-indent. The measured results reflect the mechanical properties of WC.
- Irregular nano-indentations. Figure 5.4(b) shows two sample irregular nano-indentations and a large overview of a thermal crack extending from the surface, through the recast layer, to an indent in the heat-affected zone. This study shows that irregular nano-indentations are less likely to occur and smaller variation of indentation results are observed in the heat-affected zone. It is likely due to the pores filled by the melted and resolidified Co matrix. The soft Co matrix is one possibility that may affect the irregular indentations in the heat-affected zone. Another possibility is the indent on a thermal crack initiated from outside the heat-affected zone, as shown in the 15.0 GPa hardness indent in Fig. 5.4(b).

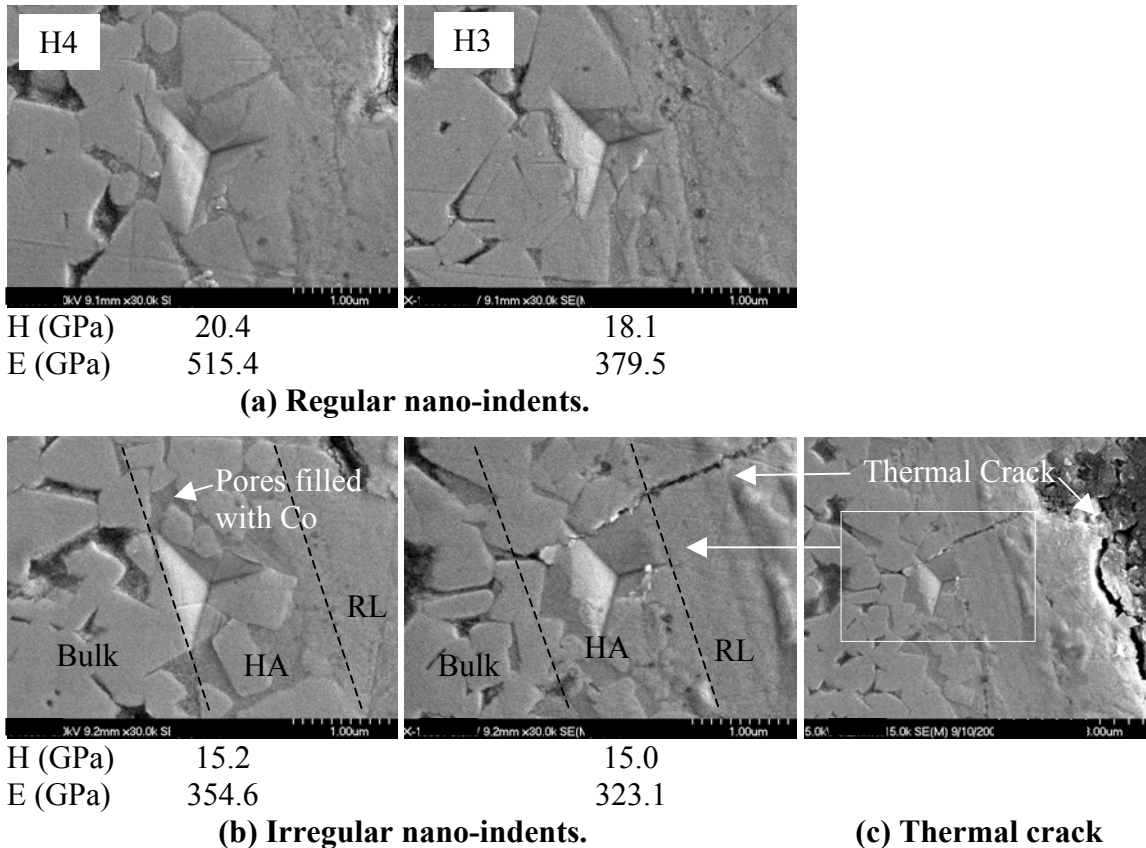


Fig. 5.4. Nanoindentation on heat-affected zone.

5.3.3 Recast Layer

The recast layer is defined as the material melted by electrical sparks and resolidified onto the surface without being ejected nor removed by flushing. As shown in Fig. 5.4, the grain boundary of WC was not clear and the porosity disappeared in the recast layer. Micro-bubbles and cracks, generated by thermal stresses in cylindrical wire EDM process, exist in the recast layer. The thickness of recast layer of the sample examined in this experiment is about 2–3 μm .

EDS X-ray was used to identify the elements in three regions: bulk material, heat-affected zone, and recast layer. Based on the EDS X-ray analysis, W, Co, and C are the main elements of the three regions. Only the recast layer has the additional peaks of Cu, Zn, and O, as shown in Fig. 5.5. The melting and resolidification of brass wire have deposited the Cu on the recast layer of WC-Co workpiece during EDM spark erosion. The high temperature also causes the oxidation, which will be investigated in the following X-ray diffraction analysis. Such contamination of Cu, O, and Zn on the surface of wire EDM silicon has been reported by Uno, et al. [15] using the X-ray Photoelectron Spectroscopy (XPS) analysis.

The X-ray diffraction was then used to further analyze the material composition of the recast layer. A 4-axis (Φ , χ , Ω , 2Θ) goniometer [16] using a copper radiation was employed for this test. Table 5.2 lists the details of the experimental conditions for the X-ray diffraction measurements. The X-ray diffraction results are shown in Fig. 5.6. Major peaks in the scan show that the recast layer contains Tungsten Carbide (WC, WC_{1-x} , and W_2C), Brass (Cu,Zn), and Cobalt Oxide (CoO). Copper Oxide (CuO) and/or Tungsten Oxide Carbide ($W_2(C, O)$), possibly exist in the recast layer, but are not distinguished. The results indicate that the tungsten carbide still exist in the recast layer, even though it cannot be well recognized by the grain boundary as in the bulk material and heat-affected zone. The Cu and Zn from the brass wire electrode were deposited to the surface recast layer. Oxides were generated due to the high temperature in EDM spark erosion.

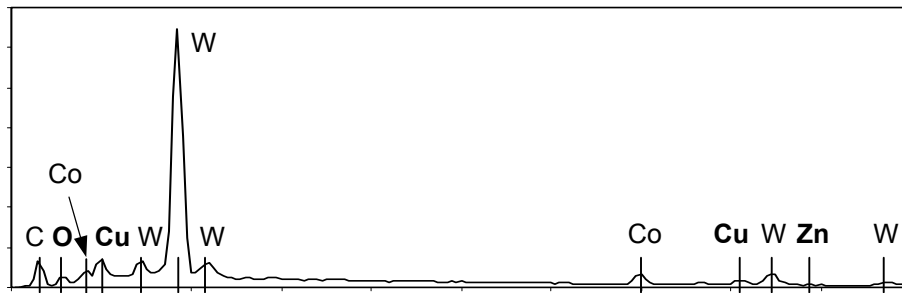


Fig. 5.5. EDS X-Ray analysis of the recast layer.

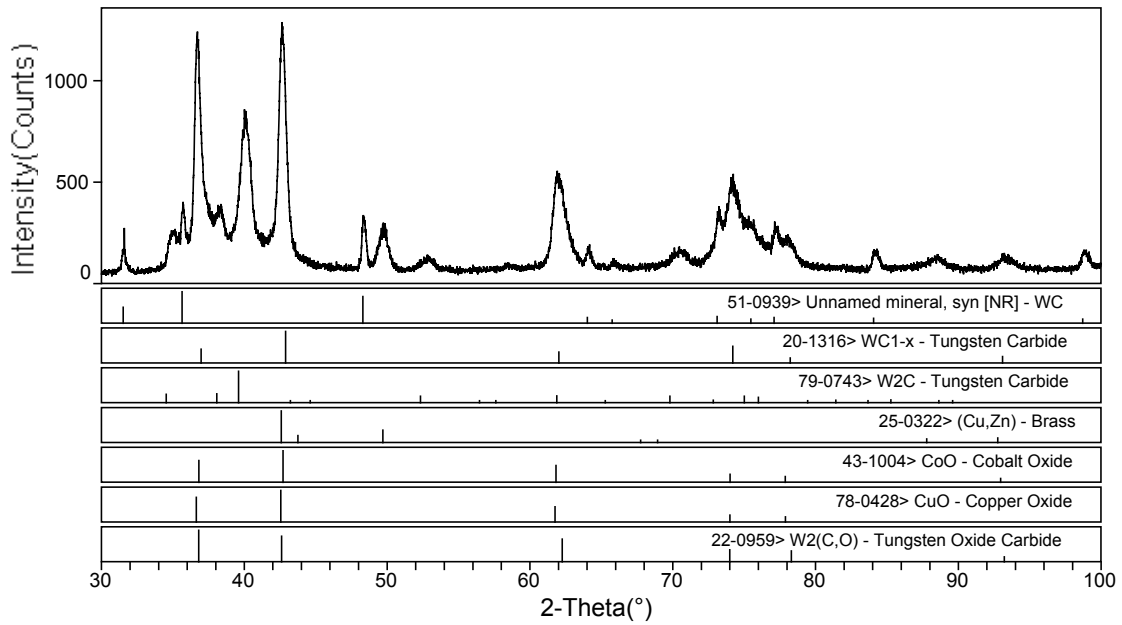


Fig. 5.6. X-Ray diffraction analysis of the recast layer.

Table 5.2. Experimental conditions of the X-ray diffraction measurements.

Parameter	Condition
Equipment	Scintag PTS goniometer MAC Science 18 kW rotating anode generator Scintag liquid N ₂ -cooled Ge detector
Power	8 kW; 40 kV, 200 mA
Radiation	Cu, $\lambda = 1.54059 \text{ \AA}$, Line Mode
Incident Optic	OSMIC "X-ray mirror" (CMF12.5 – INFCu8)
Incidence slit width	0.5 mm
Receiving slit acceptance	0.25°; radial divergence limiting (RDL) Soller slit
Source to specimen distance	360 mm
Specimen to back slit distance	280 mm
Scans	$\Theta-2\Theta$; 0.02° 2 Θ /step; 0.2°/min

The measured hardness and modulus of elasticity of the recast layer are generally lower than those of the bulk material and heat-affected zone. The deposition of brass from the wire electrode, oxidation of material, and thermal cracks are the causes for the deterioration of mechanical properties in the recast layer. Regular and irregular nano-indentations in the recast layer are identified.

- Regular nano-indentations. Figure 5.7(a) shows two regular nano-indentations in the area without clear grain boundary of WC, pores, and cracks. The measured hardness and modulus of elasticity were lower than those regular indentations in the bulk material and heat-affected zone.
- Irregular nano-indentations. The measured hardness and modulus of elasticity were highly affected by thermal cracks, bubbles, and edges in the recast layer. Some indentations with very low hardness and modulus of elasticity were observed.

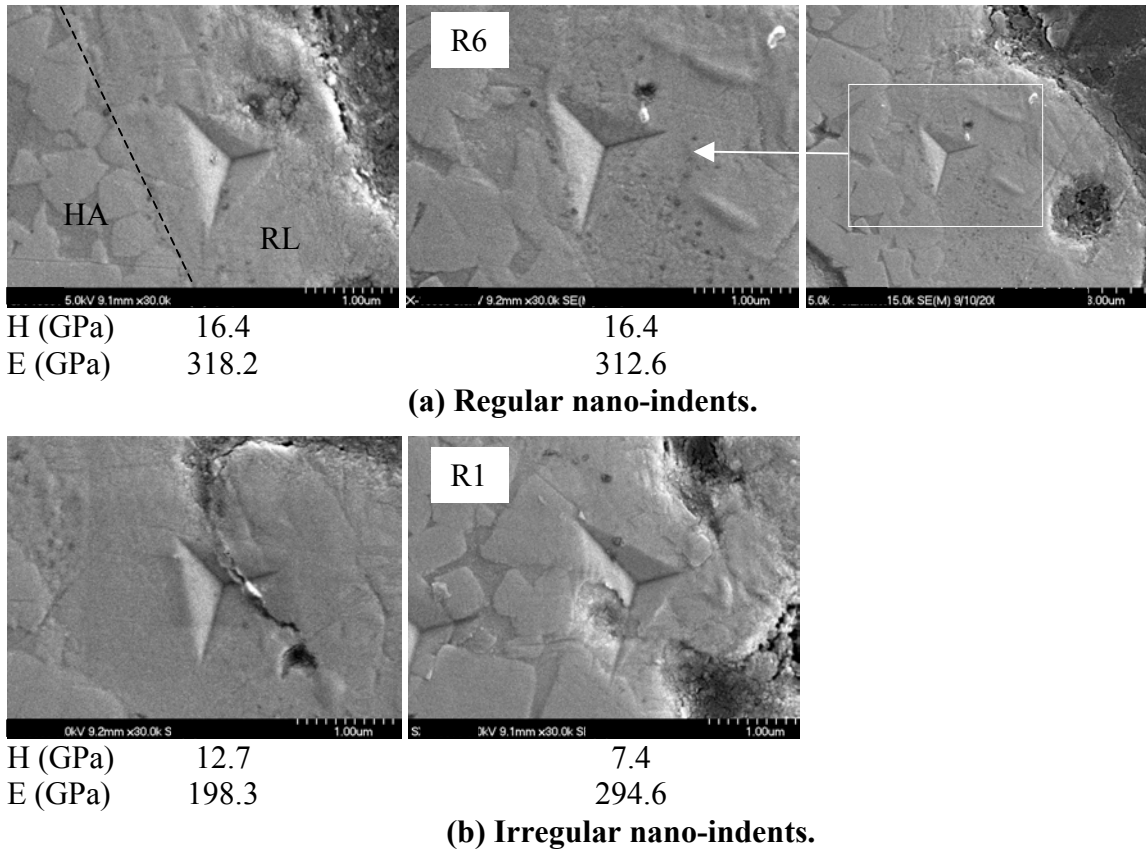


Fig. 5.7. Nanoindentation on the recast layer.

5.4. Concluding Remarks

Mechanical properties of the bulk material, sub-surface heat-affected zone, and surface recast layer of a WC-Co part machined by cylindrical wire EDM were investigated using the nanoindentation. SEM micrographs were used to classify indents in these three regions to the regular and irregular indents. Irregular indents were caused by the porosity, soft Co matrix, thermal cracks, and separation of grain boundaries

generated during indentation. The hardness and modulus of elasticity of the regular indents in bulk material and heat-affected zone are comparable to those of WC.

The heat-affected zone had more compact microstructure and better support of the WC particles. Less indentation cracking was observed in the heat-affected zone. For the regular indents, the recast layer had lower hardness and modulus of elasticity compared to the bulk material and heat-affected zone. The grain boundary of WC was not clear in the recast layer. EDS X-ray and X-ray diffraction analysis showed the WC still existed in the recast layer. In addition, the deposition of Cu and Zn from brass wire electrode and oxidation of Co and Cu on the recast layer could be identified. These effects and thermal cracks and bubbles all contribute to the deterioration of mechanical properties of the recast layer.

References

- [1] Qu, J., Shih, A. J., and Scattergood, R., 2002, "Development of the Cylindrical Wire Electrical Discharge Machining Process, Part I: Concept, Design, and Material Removal Rate," *Journal of Manufacturing Science and Engineering* (accepted).
- [2] Qu, J., Shih, A. J., and Scattergood, R., 2002, "Development of the Cylindrical Wire Electrical Discharge Machining Process, Part II: Surface Integrity and Roundness," *Journal of Manufacturing Science and Engineering* (accepted).
- [3] Llanes, L., Idanez, E., Martinez, E., Casas, B., Esteve, J., 2001, "Influence of Electrical Discharge Machining on the Sliding Contact Response of Cemented Carbides," *International Journal of Refractory Metals and Hard Materials*, Vol. 19, No. 1, pp. 35-40.
- [4] Ramulu, M., Jenkins, M. G., and Daigneanult, J. A., 1997, "Spark-Erosion Process Effects on the Properties and Performance of a TiB_2 Particulate-Reinforced/SiC Matrix Ceramic Composite," *Ceramic Engineering and Science Proceedings*, Vol. 18, No. 3, pp. 227-238.

- [5] Williams, R. E. and Rajurkar, K. P., 1991, "Study of Wire Electrical Discharge Machined Surface Characteristics," *Journal of Materials Processing Technology*, Vol. 28, pp. 127-138.
- [6] Oliver, W.C. and Pharr, G.M., 1992, "An Improved Technique for Determining Hardness and Modulus of elasticity Using Load and Displacement Sensing Indentation Experiments," *Journal of Materials Research*, Vol. 7, No. 6, pp. 1564-1580.
- [7] Riester, L. and Ferber, M.K., 1994, "Investigation of Depth-Area Relationships Associated with Nanoindentations," *Proceedings of International Engineering Foundation Conference on the Plastic Deformation of Ceramics*, August 7-12, 1994, Snowbird, Utah, pp. 185-194
- [8] Tsui, T.Y. and Pharr, G.M., 1999, "Substrate Effects on Nanoindentation Mechanical Property Measurement of Soft Films on Hard Substrates," *Journal of Materials Research*, Vol. 11, No. 1, pp. 292-301.
- [9] Zhang, J.S., Liu, X.J., Cui, H., Duan, X.J., Sun, Z.Q., and Chen, G.L., 1997, "Microstructure and Properties of Spray-Deposited 2014+15 Vol Pct Sic Particulate-Reinforced Metal Matrix Composite," *Metallurgical and Materials Transactions A: Physical Metallurgy and Materials Science*, Vol. 28A, No. 5, pp. 1261-1269.
- [10] Gee, M.G., Roebuck, B., Lindahl, P., and Andren, H.O., 1996, "Constituent Phase Nanoindentation of WC/Co and Ti(C, N) Hard Metals," *Materials Science and Engineering A: Structural Materials: Properties, Microstructure and Processing*, Vol. 209, No. 1-2, pp. 128-136.
- [11] Zhou, Y., Asaki, R., Soe, W.H., Yamamoto, R., Chen, R., and Iwabuchi, A., 1999, "Hardness Anomaly, Plastic Deformation Work and Fretting Wear Properties of Polycrystalline TiN/CrM Multilayers," *Wear*, Vol. 236, No. 1, pp. 159-164.
- [12] Zambrano, G., Prieto, P., Perez, F., Rincon, C., Galinda, H., Cota, A.L., Esteve, J., and Martinez, E., 1998, "Hardness and Morphological Characterization of WC Thin Films," *Surface and Coatings Technology*, Vol. 108, No. 1-3, pp. 323-327.
- [13] Pethica, J.B. and Oliver, W.C., 1989, "Mechanical properties of Nanometer Volumes of Material: Use of the Elastic Response of Small Area Indentations," *Thin Films Stresses and Mechanical Properties Materials Research Society Symposium Proceedings*, Vol. 130, pp. 13-23.
- [14] Oliver, W.C. and Pethica, J.B., 1989, "Method for Continuous Determination of the Elastic Stiffness of Contact Between Two Bodies," U.S. Patent No. 4848141.

- [15] Uno, Y., Okada, A., Okamoto, Y., and Hirano, T., 2000, "Wire EDM Slicing of Monocrystalline Silicon Ingot," *Proceedings of 2000 ASPE Annual Meeting*, Vol. 22, pp. 172-175.
- [16] Krause, H. and Haase, A., 1986, "X-Ray Diffraction System PTS for Powder, Texture and Stress Analysis," *Experimental Techniques of Texture Analysis*, DGM Informationsgesellschaft•Verlag, H. J. Bunge, Editor. pp. 405-408.

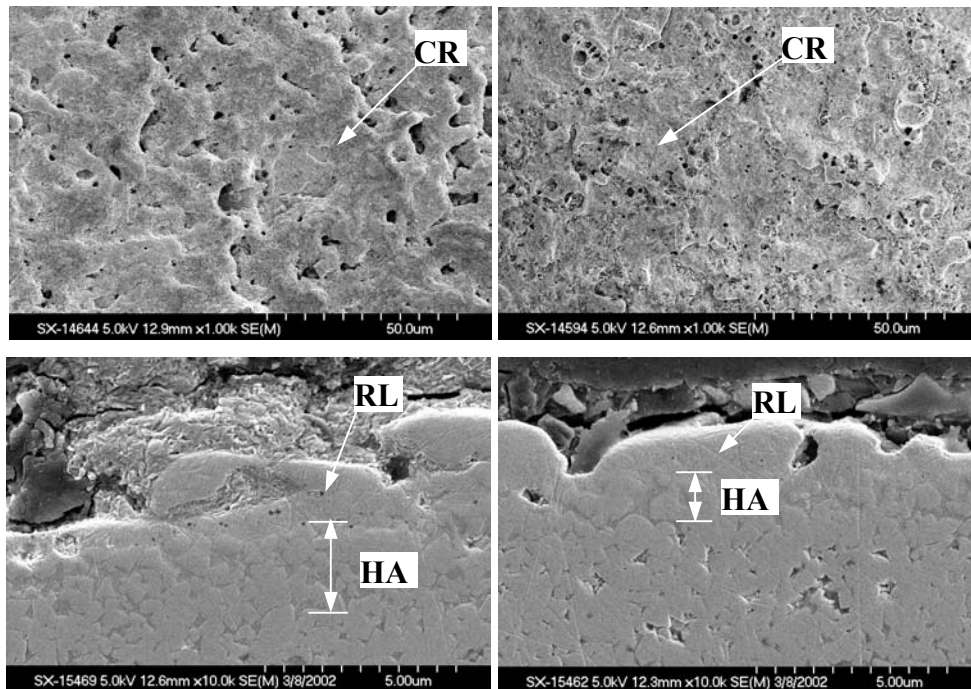
CHAPTER 6. ABRASIVE MICRO-BLASTING OF WIRE ELECTRICAL DISCHARGE MACHINED WC-CO COMPOSITE

6.1. Introduction

EDM process has been used extensively to manufacture the MMC components [1–4]. Although EDM can machine precise, complex, and intricate MMC components, the surface recast layer and subsurface heat-affected zone deteriorate the surface mechanical properties [5,6]. Figure 6.1 shows SEM micrographs of the surfaces and cross-sections of a WC-Co sample machined by rough cut and skim cut under 14 and 2 μs pulse on-time, respectively. Electrical sparks generate craters, bubbles, and cracks on the recast layer, marked by RL. A sub-surface heat-affected zone, denoted by HA, with essentially no porosity can be identified between the recast layer and bulk material. Pulse on-time is an important EDM process parameter that affects the thickness of the recast layer and heat-affected zone [2]. Keeping the spark cycle at 28 μs , the longer (14 μs) pulse on-time generates thicker recast layer and heat-affected zone, as shown in Fig. 6.1(a). The material removal rate is, in general, higher for the longer pulse on-time.

The surface integrity, including roughness, size of craters, and depth of recast layer and heat-affected zone, on cylindrical wire EDM WC-Co surface has been investigated in Chapter 3 [2]. Nanoindentation, EDS X-ray, and X-ray diffraction methods were applied to study the mechanical properties (hardness and modulus of elasticity) and material compositions of the WC-Co surface layers machined by the cylindrical wire EDM process in Chapter 5 [6]. The heat-affected zone of the EDM WC-Co part has more

compact microstructure than the bulk material and shows high hardness and modulus of elasticity [6]. However, the recast layer with craters and thermal cracks and bubbles deteriorates the surface finish and mechanical properties of the wire EDM WC-Co surface [2,6], and should be removed for surface sensitive applications. The diamond wheel grinding process has been used for this task, but it is limited to certain size, and to a flat or convex circular surface. The erosion properties of WC-Co composite has been studied by [7,8]. In this study, micro-blasting is proposed, as a finishing process, to improve the surface integrity of the WC-Co parts machined by wire EDM. The material removal mechanism of blasting is erosion wear.

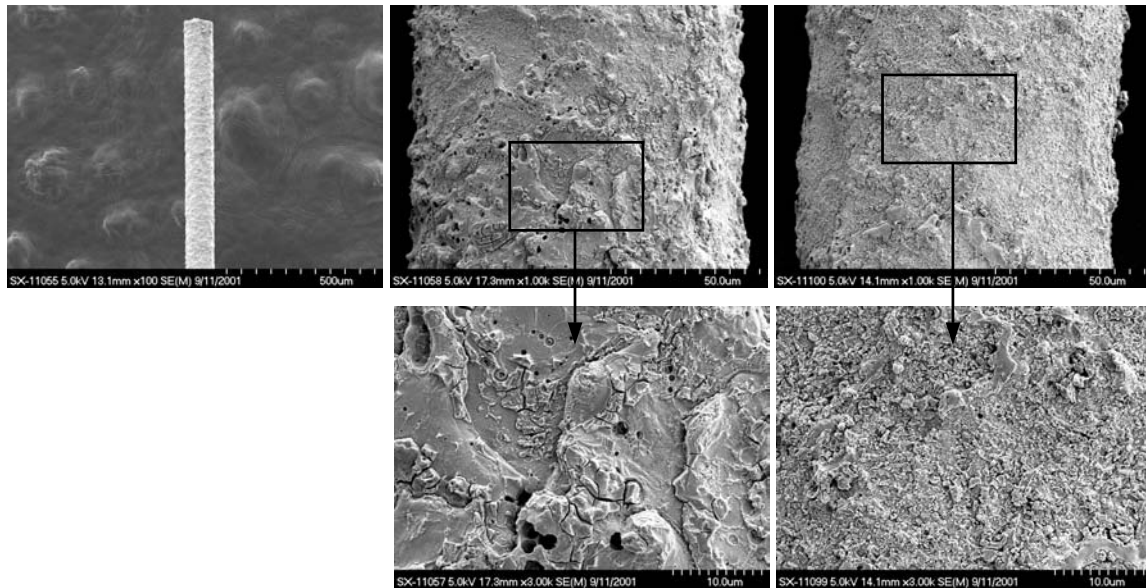


(Legend – CR: Crater, RL: Recast layer, and HA: Heat affected zone)
 (a) Rough cut (14 μ s pulse on-time). (b) Skim cut (2 μ s pulse on-time).

Fig. 6.1. SEM micrographs of the surface and cross-section of a WC-Co part machined by wire EDM.

Abrasive blasting has been widely applied to surface treatment, increasing roughness for higher adhesion strength in coating process [9,10], or reducing roughness for better surface integrity and higher strength and wear resistance with compressive residual stress introduced by the blasting process [11–14]. Micro-blasting using very small size media is particularly suitable for microfabrication and surface treatment of micro components [9,15]. The micro size abrasives along with low air pressure enable the micro-blasting to do microfabrication or treat the surface of micro parts. The EDM process, without macro cutting force, is suitable to machine micro components [16,17]. Improving the surface integrity of the EDM micro parts has been an important research topic. The thickness of EDM recast layer and heat-affected zone is usually very thin [2–4]. For example, as shown in Fig. 6.1, the thickness of EDM surface layers is less than 3 μm .

In this study, micro-blasting was applied to the micro cylindrical wire EDM WC-Co parts. Figure 6.2 shows a 100 μm diameter WC-Co cylinder machined by cylindrical wire EDM and then blasted using 6~12 μm size black SiC abrasive at 0.138 MPa air pressure for 5 s. The close-views illustrate that the craters on the surface generated by EDM sparks were eliminated by blasting and the surface turned to be smoother.



(a) Over view of the micro part before blasting.

(b) Close view of the surface before blasting.

(c) Close view of the surface after blasting.

Fig. 6.2. Micro-blasting on a micro cylindrical wire EDM WC-Co part.

Lee and Deng [13,18,19] have used abrasive blasting to treat the wire EDM ceramic composite surface to improve the surface integrity, strength, and reliability. There was lack of optimization of the blasting process and correlation between the process parameters. In this study, blasting with micro size SiC abrasives is applied to the wire EDM WC-Co surface at multiple process settings to investigate the erosion wear and surface integrity improvement. Effects of key process parameters of micro-blasting, abrasive size, air pressure, and blasting time, on the both rough and fine wire EDM WC-Co surfaces are explored. The micro-blasting process is also applied to the micro round shape parts machined by cylindrical wire EDM. Scanning Electron Microscopy (SEM) is used to examine the surface and polished cross-section of the blasted wire EDM WC-Co samples.

The sample preparation and experiment setup are introduced in the following section. The experimental results and discussions are presented in Sec. 6.3.

6.2. Sample Preparation and Experiment Setup

The WC-Co composite consisting of WC particles about 1 μm size in 10% cobalt matrix was used as the work-material in this study. It has 92 Rc hardness, 3.4 MPa transverse rupture stress, and 14.5 specific density. Two sets of WC-Co parts were prepared for micro-blasting, which were machined by wire EDM using rough cut and skim cut technologies, and represented by R and S in the following sections, respectively. The process parameters of the two wire EDM cutting technologies are given in Table 6.1.

Table 6.1. Process parameters of wire EDM rough cut and skim cut.

Cutting technology	Rough cut	Skim cut
Spark cycle (μs)	28	28
On-time (μs)	14	2
Axial wire speed (mm/s)	18	15
Wire tension (N)	14.7	17.6
Gap voltage (V)	45	60

Micro-blasting experiments on wire EDM WC-Co surfaces were conducted to investigate the erosion wear rate and surface integrity improvement. All experiments were conducted on a Mangum blasting machine, manufactured by Blast-it-all. Two types of black SiC abrasives were used in the micro-blasting experiments. The abrasive A, as

shown in Fig. 6.3(a), is the mix of 4~8, 6~12, and 8~16 μm sizes SiC particles, and the size of abrasive B is in the range of 6~12 μm , as shown in Fig. 6.3(b).

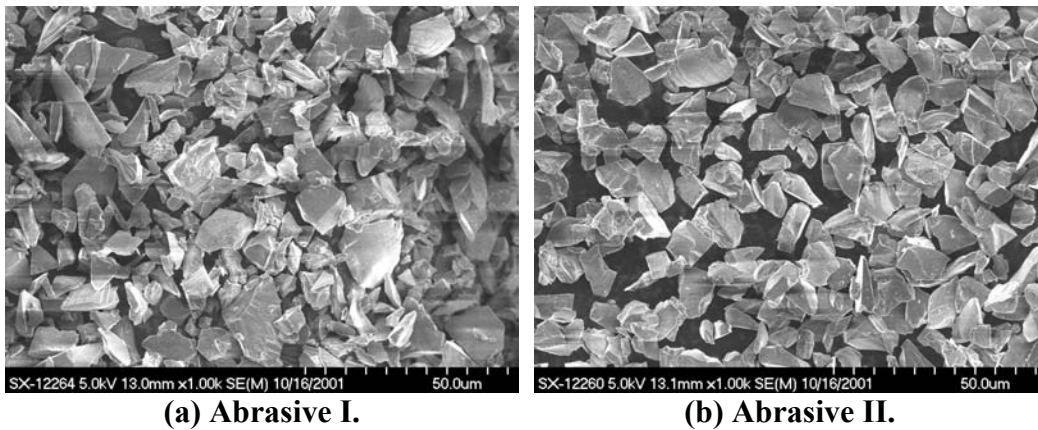


Fig. 6.3. Two sizes of SiC abrasives.

The process parameters of the experiments are listed in Table 6.2. In this study, zero incident angle was used, which means the abrasive velocity vector is normal to the surface. Two key parameters of the blasting process, the air pressure and blasting time were varied in this study to explore their effect on the erosion wear and surface integrity. The WC-Co workpieces for erosion wear rate experiment were machined using wire EDM rough cut. In the surface integrity experiment, the micro-blasting was applied to the surfaces of both rough cut and skim cut WC-Co parts.

Table 6.2. Process parameters of Micro-blasting experiments.

Experiment	Erosion wear rate	Surface integrity
Air pressure (MPa)	0.138, 0.276	0.138, 0.276
Blasting time (s)	10, 20, 30	5, 10, 15

6.3. Experimental Results and Discussions

The results of the erosion wear and surface integrity improvement experiments are summarized below.

6.3.1. Erosion wear Rate

The micro-blasting erosion wear rate was measured by the weight reduction during the blasting process. In the erosion wear rate experiment, the wire EDM rough cut WC-Co part was blasted using abrasives A and B at 0.276 and 0.138 MPa air pressure by 10, 20, and 30 s blasting durations. Figure 6.4 shows the experimental results of erosion wear for abrasive A and B at two air pressures and three blasting durations. Some observations could be made:

- *Effect of abrasive size.* The erosion wear rate using abrasive A was higher than that of abrasive B under the same blasting condition, because abrasive A had the relatively larger size particles.
- *Effect of air pressure.* The higher air pressure (0.276 MPa) generated higher erosion wear than the lower air pressure (0.138 MPa). Almost doubled erosion wear rate was achieved for doubled air pressure.
- *Effect of blasting duration.* More material was removed at the first 10 s than the following blasting durations. That is probably because of the weak recast layer was removed at beginning. The recast layer had lower hardness and modulus of

elasticity than the heat-affected zone and bulk material [6]. In addition, the thermal cracks and bubbles in the recast layer made it to be blasted off easily.

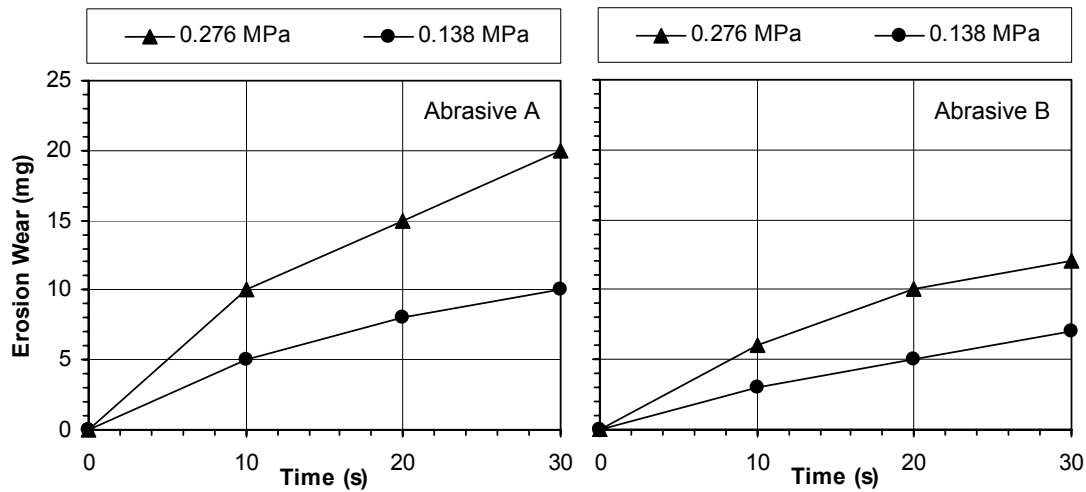


Fig. 6.4. Erosion wear rate of micro-blasting on wire EDM WC-Co.

6.3.2. Surface Integrity Improvement

In this experiment, the micro-blasting process was applied to improve the surface integrity of the wire EDM WC-Co parts by removing the recast layer. Abrasives A and B were used to blast the rough cut and skim cut EDM surfaces at high (0.138 MPa) and low (0.276 MPa) air pressures and three blasting durations, 5, 10, and 15 s. Totally twenty-four parts were blasted and examined. The surface roughness for the WC-Co parts before blasting and after blasting at different experimental conditions is represented by two roughness parameters, R_a and R_z , as shown in Fig. 6.5. The charts of surfaces roughness

indicate that the surface finish improvement of micro-blasting highly depends on the original surface integrity and blasting parameters.

SEM was used to examine the surfaces and sub-surfaces of the WC-Co parts to investigate the effect of the micro-blasting. The SEM micrographs of the surfaces and polished cross-sections of selected blasted parts are shown in Figs. 6.6~6.10.

Based on the surface roughness results and SEM micrographs, the original EDM surface, abrasive size, air pressure, blasting duration all together determined the surface integrity after blasting.

- *Effect of original EDM surface.* The rough cut WC-Co parts had 2~3 μm thick recast layer and 1.3~1.4 μm R_a and 8~9 μm R_z surface roughness. The surface and cross-section of a sample parts are shown in Fig. 6.1(a). The recast layer was removed after 15 s blasting, as shown in Figs. 6.6, 6.7, and 6.8, and the surface roughness could be reduced significantly, down to about 0.8 μm R_a and 4 μm R_z , as shown in Fig. 6.5. As the surface and cross-section shown in Fig. 6.1(b), the skim cut EDM parts had thinner recast layer (about 1 μm). The surface roughness was about 0.7~0.9 μm R_a and 5~7 μm R_z for the skim cut parts. Figures 6.9 and 6.10 show that the recast layer had been removed after 5 s blasting. Using abrasive A at low air pressure and abrasive B at both high and low air pressure, the roughness values did not drop down much, as shown in Fig. 6.5, though the surfaces look smoother in the SEM micrographs (Fig. 6.9). The surface finish may turn to be worse using abrasive A at high air pressure, as illustrated in Figs. 6.5 and 6.10.
- *Effect of abrasive size and air pressure.* The abrasive A with larger size particles and/or high air pressure (0.276 MPa) removed the recast layer faster and reduced the surface roughness of rough cut parts more efficiently than the lower air pressure (0.138 MPa), as shown in roughness charts (Fig. 6.5) and SEM micrographs (Figs. 6.6~6.9). However, the skim cut surface may be deteriorated by short time blasting using abrasive A and high air pressure, as shown in Figs. 6.5 and 6.10.

- *Effect of blasting duration.* Basically, the longer blasting time, the better surface finish. For certain abrasive and air pressure, the surface roughness will reach the bottom line after long enough blasting duration, no matter the original surface finish. Figure 6.5 shows the trend, though some roughness values did not drop down to the limit because of insufficient blasting time.

Some interesting pattern can be seen on the blasted surfaces, as shown in Figs. 6.6~6.10. The topography was probably generated by the EDM process, but messed with the rough recast layer, and revealed by the blasting process.

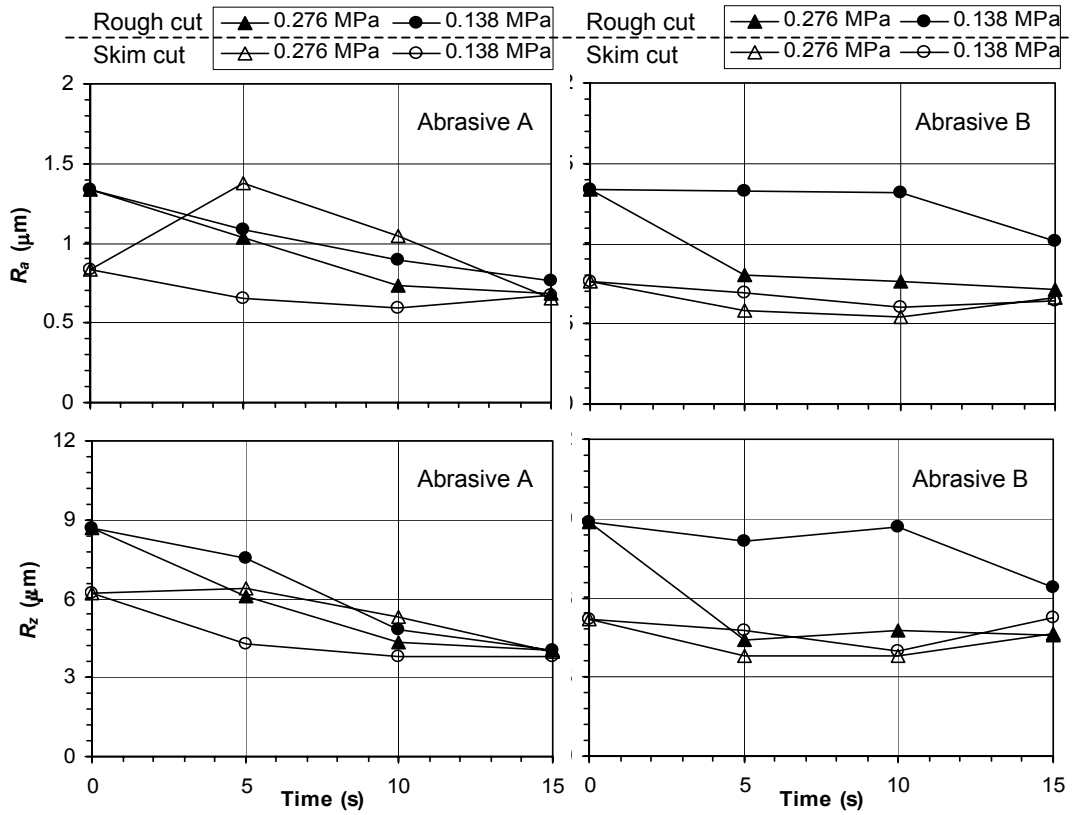


Fig. 6.5. Surface finish improvement on wire EDM WC-Co using micro-blasting.

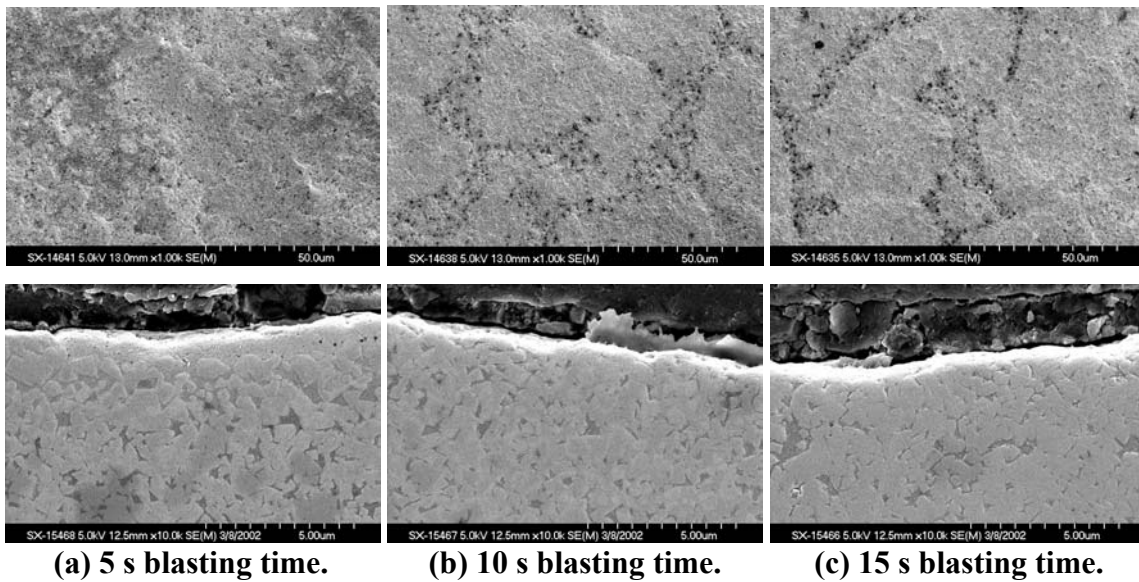


Fig. 6.6. SEM micrographs of surfaces and cross-sections of the wire EDM rough cut WC-CO part after micro-blasting using abrasive A at 0.276 MPa air pressure.

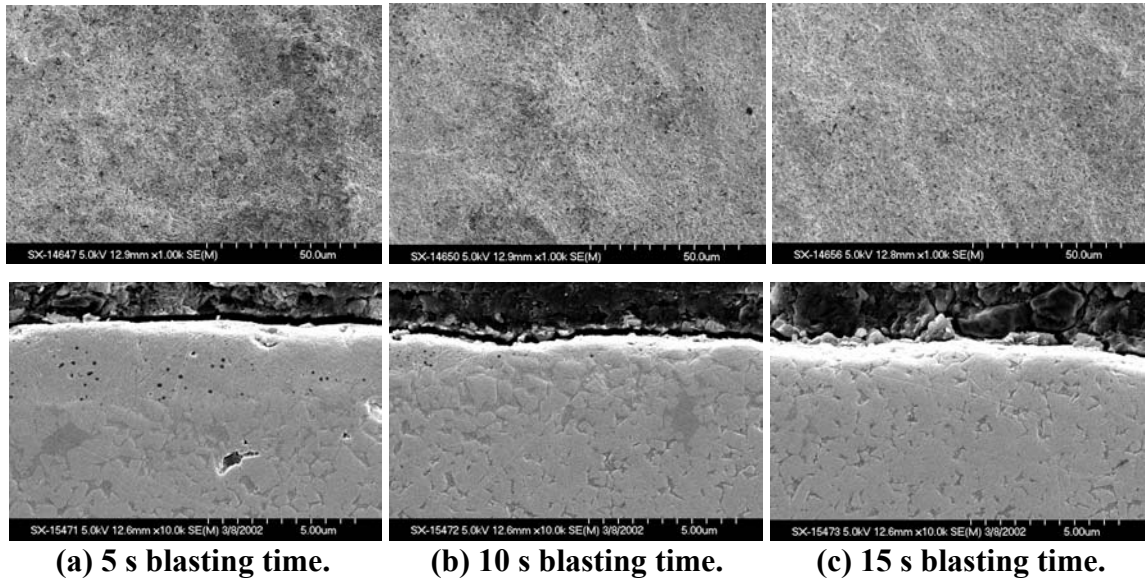


Fig. 6.7. SEM micrographs of surfaces and cross-sections of the wire EDM rough cut WC-CO part after micro-blasting using abrasive A at 0.138 MPa air pressure.

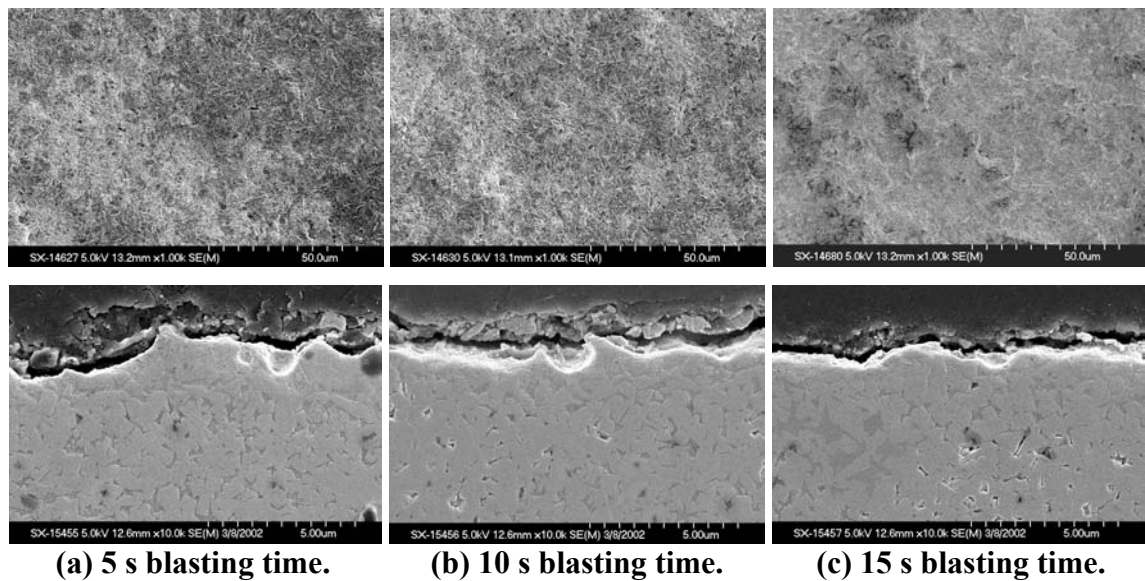


Fig. 6.8. SEM micrographs of surfaces and cross-sections of the wire EDM rough cut WC-CO part after micro-blasting using abrasive B at 0.138 MPa air pressure.

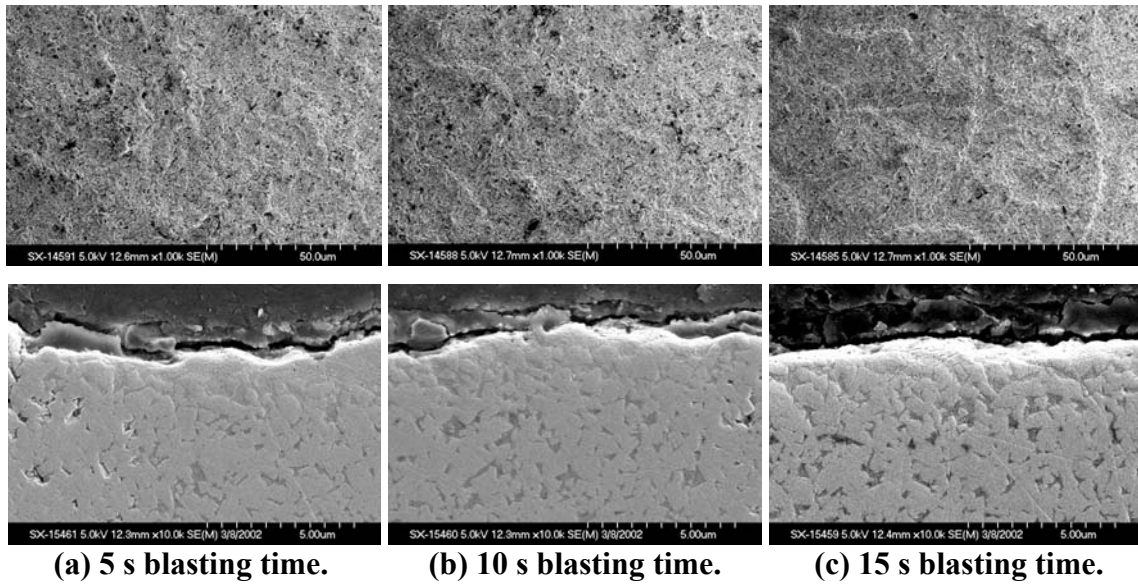


Fig. 6.9. SEM micrographs of surfaces and cross-sections of the wire EDM skim cut WC-CO part after micro-blasting using abrasive B at 0.276 MPa air pressure.

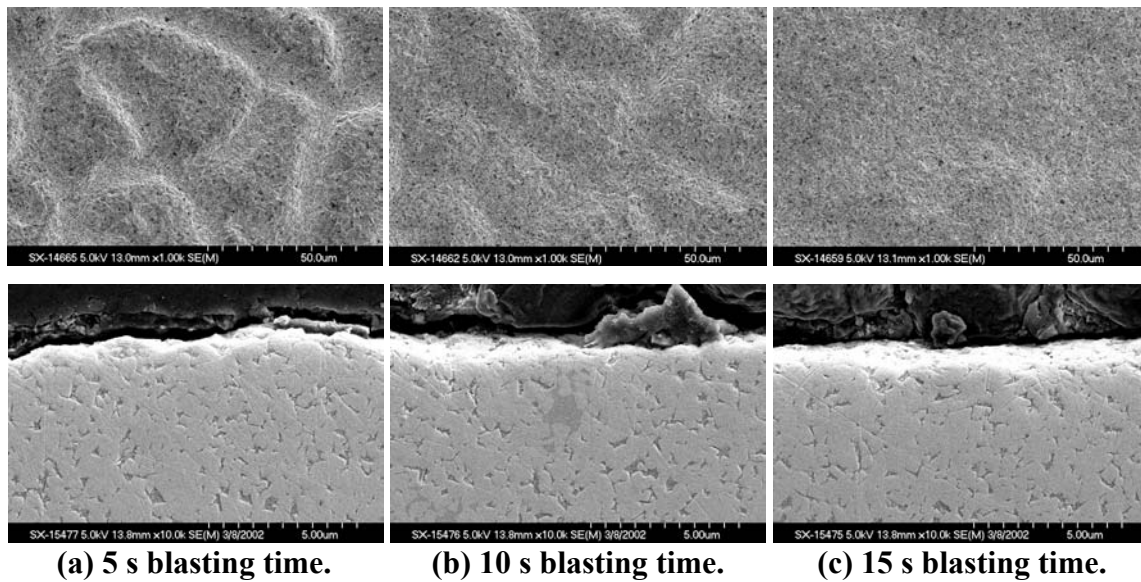


Fig. 6.10. SEM micrographs of surfaces and cross-sections of the wire EDM skim cut WC-CO part after micro-blasting using abrasive A at 0.276 MPa air pressure.

6.4. Concluding Remarks

The abrasive micro-blasting process was used to improve the surface integrity of the WC-Co parts machined by wire EDM. Two sizes of black SiC abrasives, two air pressures, and three blasting durations were applied to both wire EDM rough cut and skim cut WC-Co surfaces to explore the effects of blasting parameters on the surface integrity. The SEM micrographs showed that the recast layer was eventually removed by micro-blasting. The larger size abrasive and higher air pressure had higher erosion wear rate and reduce the surface roughness more effectively. The surface roughness of EDM rough cut parts was reduced significantly, R_a dropping down from 1.34 to about 0.7 μm , while little improvement was made on the surface finish of skim cut parts.

References

- [1] Qu, J., Shih, A. J., and Scattergood, R., 2002, "Development of the Cylindrical Wire Electrical Discharge Machining Process, Part I: Concept, Design, and Material Removal Rate," *Journal of Manufacturing Science and Engineering* (accepted).
- [2] Qu, J., Shih, A. J., and Scattergood, R., 2002, "Development of the Cylindrical Wire Electrical Discharge Machining Process, Part II: Surface Integrity and Roundness," *Journal of Manufacturing Science and Engineering* (accepted).
- [3] Llanes, L., Idanez, E., Martinez, E., Casas, B., Esteve, J., 2001, "Influence of Electrical Discharge Machining on the Sliding Contact Response of Cemented Carbides," *International Journal of Refractory Metals and Hard Materials*, Vol. 19, No. 1, pp. 35-40.
- [4] Ramulu, M., Jenkins, M. G., and Daigneanult, J. A., 1997, "Spark-Erosion Process Effects on the Properties and Performance of a Tib_2 Particulate-Reinforced/Sic Matrix Ceramic Composite," *Ceramic Engineering and Science Proceedings*, Vol. 18, No. 3, pp. 227-238.

- [5] Williams, R. E. and Rajurkar, K. P., 1991, "Study of Wire Electrical Discharge Machined Surface Characteristics," *Journal of Mechanical Processing Technology*, Vol. 28, pp. 127-138.
- [6] Qu, J., Riester, L., Shih, A. J., Scattergood, R., Lara-Curzio, E., and Watkins, T., 2002, "Nanoindentation Characterization of Surface Layers of Electrical Discharge Machined Wc-Co," *Materials Science and Engineering-A* (to be submitted).
- [7] Beste, U., Hammerstrom, L., Engqvist, H., Rimlinger, S., and Jacobson, S., 2001, "Particle erosion of cemented carbides with low Co content," *Wear*, Vol. 250-251, pp. 809-817.
- [8] Pugsley, V.A., Allen, C., 1999, "Microstructure/property relationships in the cavitation **erosion** of tungsten carbide-cobalt," *Wear*, Vol. 233-235, pp. 93-103.
- [9] Bouzakis, K.D., Michailidis, N., Hadjiyiannis, S., Efstathiou, K., Pavlidou, E., Erkens, G., Rambadt, S., and Wirth, I., 2001, "Improvement of PVD Coated Inserts Cutting Performance Through Appropriate Mechanical Treatments of Substrate and Coating Surface," *Surface and Coating Technology*, Vol. 146-147, pp. 443-450.
- [10] Guilemany, J.M., Llorca, I.N., and Szabo, P.J., 1996, "Residual Stress Characterization of Grit Blasted Steel Surfaces," *Surface Engineering*, Vol. 12, No. 1, pp. 77-79.
- [11] Hung, N.P., Teong, L.H., and Yoong, C.M., 1996, "Review of Unconventional Machining of Metal Matrix Composites," *Proceedings of the 1996 3rd Biennial Joint Conference on Engineering Systems Design and Analysis, ASME PD*, New York, NY, Vol. 75, No. 3, pp. 47-53.
- [12] Ben Rhouma, A., Braham, C., Fitzpatrick, M.E., Ledion, J., and Sidhom, H., "Effects of Surface Preparation on Pitting Resistance, Residual Stress, and Stress Corrosion Cracking in Austenitic Stainless Steels," *Journal of Materials Engineering and Performance*, Vol. 10, No. 5, pp. 507-514.
- [13] Deng, J. and Le, T.C., 2000, "Techniques for Improved Surface Integrity of Electrodischarge Machined Ceramic Composites," *Surface Engineering*, Vol. 16, No. 5, pp. 411-414,
- [14] Lai, M.O. and Siew, Y.H., 1995, "Fatigue Properties of Cold Worked Holes," *Journal of Materials Processing Technology*, Vol. 48, pp. 533-540.
- [15] Schlautmann, S., Wensink, H., Schasfoort, R., Elwenspoek, M., and Berg, A., 2001, "Powder-Blasting Technology as an Alternative Tool for Microfabrication of Capillary Electrophoresis Chips with Integrated Conductivity Sensors," *Journal of Micromechanics and Microengineering*, Vol. 11, pp. 386-389.

- [16] Masuzawa, T. and Tonshoff, H. K., 1997, "Three-Dimensional Micromachining by Machine Tools," *Annals of CIRP*, Vol. 46, pp. 621-628.
- [17] Rajurkar, K. P. and Yu, Z. Y., 2000, "3D Micro-EDM Using CAD/CAM," *Annals of CIRP*, Vol. 49, pp. 127-130.
- [18] Lee, T.C. and Zhang, J.H., 1997, "Surface Treatment of Wire Electro-Discharge Machined Engineering Ceramics by Abrasive Blasting," *Journal of Adhesion Science Technology*, Vol. 12, No. 6, pp. 585-592.
- [19] Lee, T. and Deng, J., 2002, " Mechanical Surface Treatments of Electro-Discharge Machined (EDMed) Ceramic Composite for Improved Strength and Reliability," *Journal of European Ceramic Society*, Vol. 22, pp. 545-550.

CHAPTER 7. CONCLUSIONS

The cylindrical wire EDM process was developed for machining free-form cylindrical components of difficult-to-machine materials, such as the Metal Matrix Composites. This process is suitable to machine micro-size shafts, because of the minimum cutting force. A precise, flexible, and corrosion-resistant underwater rotary spindle was designed and the spindle errors were analyzed using FFT. The spindle was found to be a critical factor in achieving the desired roundness, surface finish, and material removal rate.

The mathematical models of the material removal rate and surface finish for any free-form cylindrical geometry were derived and verified by experiments. The closed-form surface finish model was extended to a general solution for any theoretical surface profile consisting of elliptical or circular arcs. It offers accurate surface roughness evaluation for a wide range of process conditions and can be used in CAD/CAM systems for machining process modeling.

Experimental results indicated that higher maximum material removal rate might be achieved in the cylindrical wire EDM than the conventional 2D wire EDM. This indicates that the cylindrical wire EDM is an efficient material removal process. Two sets of experiments were conducted to identify the effects of part rotational speed, wire feed rate, and pulse on-time on the surface roughness and roundness. It was demonstrated that good surface finish and low roundness error could be achieved in the cylindrical wire EDM process.

The surface integrity and material composition of cylindrical wire EDM WC-Co surface layers were investigated using SEM, Nanoindentation, EDS X-ray, and X-ray diffraction. Cylindrical EDM WC-Co surfaces were first examined using SEM to identify the EDM surface features, e.g. craters, and thermal cracks and bubbles. The recast layer and heat-affected zone were then observed and quantified on the SEM micrographs of the cross-sections of the EDM parts. The effects of process parameters on the surface roughness and the thickness of damage layers were also studied. The nanoindentation was applied to a cylindrical wire EDM WC-Co part to investigate the mechanical properties of the bulk material, heat-affected zone, and recast layer. SEM was used to observe and classify the indents to the regular and irregular indents. Irregular indents were caused by the porosity, soft Co matrix, thermal cracks, and cracking generated during indentation. The hardness and modulus of elasticity of the regular indents in bulk material and heat-affected zone are comparable to those of WC. The heat-affected zone had more compact microstructure less indentation cracking. For the regular indents, the recast layer had lower hardness and modulus of elasticity compared to the bulk material and heat-affected zone. EDS X-ray and X-ray diffraction analysis showed the WC still existed in the recast layer, though the grain boundary of WC was not clear. In addition, the deposition of Cu and Zn from brass wire electrode and oxidation of Co and Cu on the recast layer could be identified. These effects and thermal cracks and bubbles all contribute to the deterioration of mechanical properties of the recast layer.

The micro-blasting process with micro-size SiC abrasives was applied to improve the surface integrity of the EDM surfaces. The recast layer with poor mechanical properties

was eventually removed and the surface roughness of WC-Co parts was reduced. Compressive residual stress introduced by micro-blasting could result in higher surface wear resistance. The effects of micro-blasting process parameters on the surface integrity of EDM WC-Co surfaces were investigated to increase the process efficiency. SEM was also used to examine the blasted surfaces and their cross-sections.

APPENDICES

Appendix A. Material Removal Rate Modeling in Cylindrical Wire EDM

The mathematical model of Material Removal Rate (*MRR*) in cylindrical wire EDM of a free-form shape is presented. This is a geometrical model, which does not include the process parameters, such as voltage and current. Figure A.1 shows the free-form cylindrical geometry machined by the cylindrical wire EDM process. The effective circles of the wire at time $t-\Delta t$ and t are represented by $C_e^{t-\Delta t}$ and C_e^t , respectively. Δr is the change of r during Δt , and can be expressed as:

$$\Delta r = v_f \Delta t \cdot \sin \alpha \tag{A.1}$$

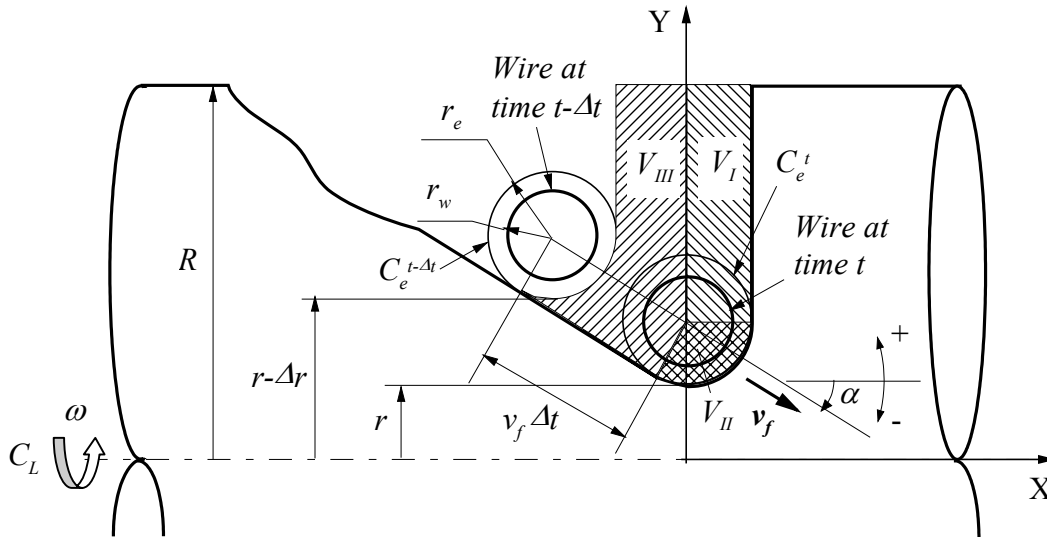


Fig. A.1. Free form geometry in cylindrical wire EDM.

The volume of the material removed from $t-\Delta t$ to t is denoted as V . As shown in Fig. A.1, V is the volume swept by the hatched area around the X-axis. V can be divided into three portions, V_I , V_{II} , and V_{III} .

$$V = V_I + V_{II} + V_{III} \tag{A.2}$$

V_I is a ring with outer radius R , inner radius $r + r_e$, and thickness r_e .

$$V_I = \pi[R^2 - (r + r_e)^2]r_e \tag{A.3}$$

An enlarged figure of the volume V_{II} is shown in Fig. A.2.

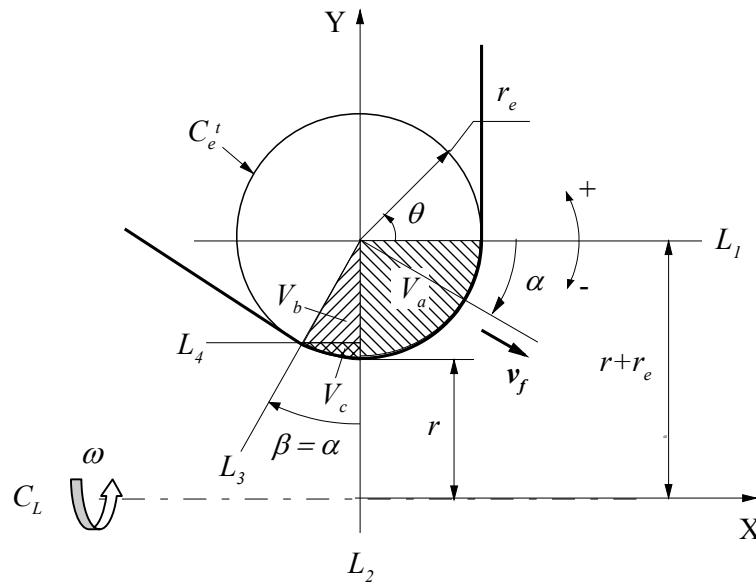


Fig. A.2. Calculation of V_{II} .

$$V_{II} = V_a + V_b + V_c \quad (\text{A.4})$$

where

$$V_a = \pi r_e^2 \left[\frac{\pi}{2}(r + r_e) - \frac{2}{3}r_e \right] \quad (\text{A.4a})$$

$$V_b = \pi r_e^2 \left[-(r + r_e) \sin \alpha \cos \alpha + \frac{2}{3}r_e \sin \alpha \cos^2 \alpha \right] \quad (\text{A.4b})$$

$$V_c = \pi r_e^2 \left[(r + r_e)(-\alpha + \sin \alpha \cos \alpha) + \frac{2}{3}r_e \sin^3 \alpha \right] \quad (\text{A.4c})$$

Substituting Eqs. (A.4a) – (A.4c) into Eq. (A.4),

$$V_{II} = \pi [r_e^2 (r + r_e) \left(\frac{\pi}{2} - \alpha \right) - \frac{2}{3}r_e^3 (1 - \sin \alpha)] \quad (\text{A.5})$$

V_{III} is the combination of cylinders, cones and rotated pies, as shown in Fig. A.3.

$$V_{III} = V_{NBFH} + V_{CDEF} - V_{ABCM} - V_{MCD} - V_{KGED} - V_{JKGH} \quad (\text{A.6})$$

where

$$V_{NBFH} = \pi R^2 \Delta r / \tan \alpha \quad (\text{A.6a})$$

$$V_{ABCM} = \pi [R^2 - (r - \Delta r + r_e)^2] \cdot r_e \quad (\text{A.6b})$$

$$V_{CDEF} = V_{PFC} - V_{PED} = -\frac{1}{3} \pi [(r - \Delta r + r_e)^3 - (r - \Delta r + r_e - r_e \cos \alpha)^3] \tan \alpha \quad (\text{A.6c})$$

$$V_{KDEG} = V_{TDE} - V_{TKG} = -\frac{1}{3} \pi [(r - \Delta r + r_e - r_e \cos \alpha)^3 - (r + r_e - r_e \cos \alpha)^3] / \tan \alpha \quad (\text{A.6d})$$

$$V_{JKGH} = V_{SHJ} - V_{SGK} = -\frac{1}{3} \pi [(r + r_e)^3 - (r + r_e - r_e \cos \alpha)^3] \tan \alpha \quad (\text{A.6e})$$

$$V_{MCD} = \pi \left[r_e^2 (r - \Delta r + r_e) \left(\frac{\pi}{2} - \alpha \right) - \frac{2}{3} r_e^3 (1 - \sin \alpha) \right] \quad (\text{A.6f})$$

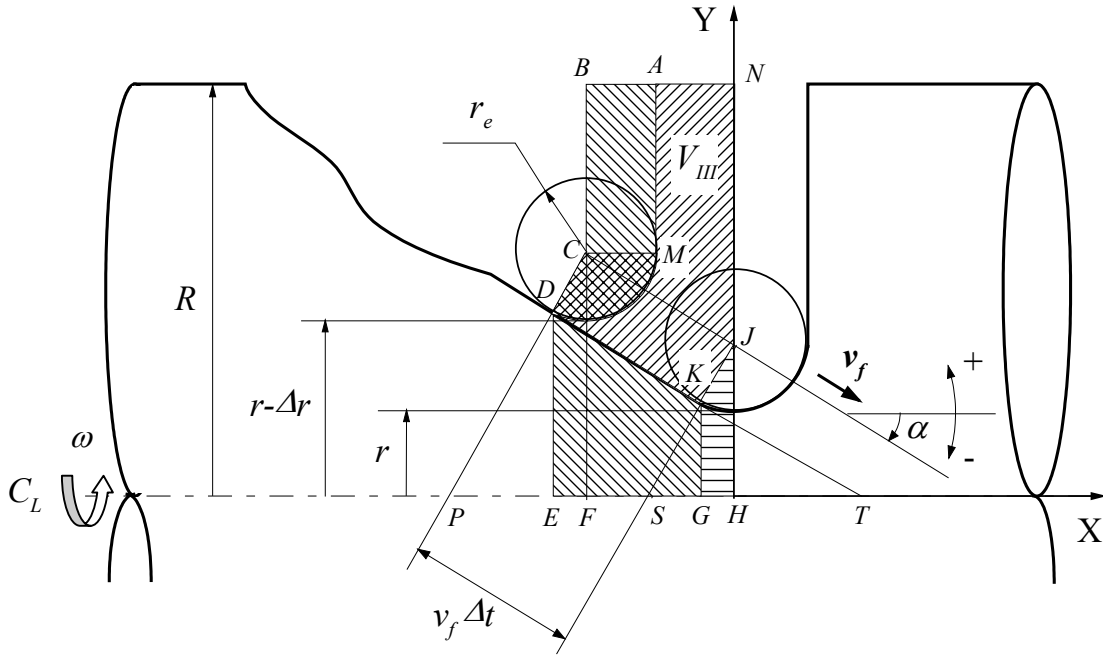


Fig. A.3. Calculation of V_{III} .

Substituting the formula of V_I , V_{II} , and V_{III} into Eq. (A.2), V can be expressed as:

$$\begin{aligned}
 V = & -\pi \left(\frac{1}{3 \tan \alpha} \right) \cdot (\Delta r)^3 + \pi \left[r \frac{1}{\tan \alpha} + r_e \left(\frac{1}{\tan \alpha} - \frac{1}{\sin \alpha} + 1 \right) \right] \cdot (\Delta r)^2 \\
 & + \pi \left[\begin{aligned} & (R^2 - r^2) \frac{1}{\tan \alpha} + 2rr_e \left(\frac{1}{\sin \alpha} - \frac{1}{\tan \alpha} - 1 \right) \\ & + r_e^2 \left(\frac{2}{\sin \alpha} - \frac{2}{\tan \alpha} - 2 - \alpha + \frac{\pi}{2} \right) \end{aligned} \right] \cdot \Delta r
 \end{aligned} \tag{A.7}$$

Substituting Eq. (A.1) into Eq. (A.7),

$$\begin{aligned}
 MRR = \lim_{\Delta t \rightarrow 0} \frac{V}{\Delta t} = & v_f \cdot \pi [(R^2 - r^2) \cos \alpha \\
 & + 2rr_e (1 - \sin \alpha - \cos \alpha) \\
 & + r_e^2 (2 - 2 \cos \alpha + (\frac{\pi}{2} - 2 - \alpha) \sin \alpha)]
 \end{aligned} \tag{A.8}$$

Appendix B. Derivation of Semi-Axes a and b and Feed f for a Measurement Profile on the Surface Machined by Flat-End Milling

Figure B.1 shows a grooved surface machined by a flat-end mill with radius r and pitch p between parallel tool paths. The trace for surface finish measurement is at an angle θ relative to the velocity vector of the end mill, V . The definitions of the X- and Y-axes are the same as on the surface measurement profile presented in Fig. 1. X-axis is tangent to the valley of the elliptical arcs and Y-axis is perpendicular to the nominal surface. On the XY plane, the theoretical profile consists of elliptical arcs with semi-axes a and b and feed f . Two angles, α and β , are used to define the orientation of the tool relative to the XYZ coordinate. A coordinate X'Y'Z' with origin at O' on the axis of the tool is illustrated in Fig. A.1. X', Y', and Z' axes are parallel to X, Y, and Z axes, respectively. Line O'D is the projection of the tool axis O'C on the X'-Z' plane. α is the angle between X'-axis and O'D and β is the angle between O'C and O'D.

The semi-axes a and b and feed f of the elliptical arc on the measuring profile are:

$$a = r \frac{\cos(\alpha - \theta)}{\sin \theta} \quad (\text{B.1})$$

$$b = r \cos \beta \quad (\text{B.2})$$

$$f = \frac{p}{\sin \theta} \quad (\text{B.3})$$

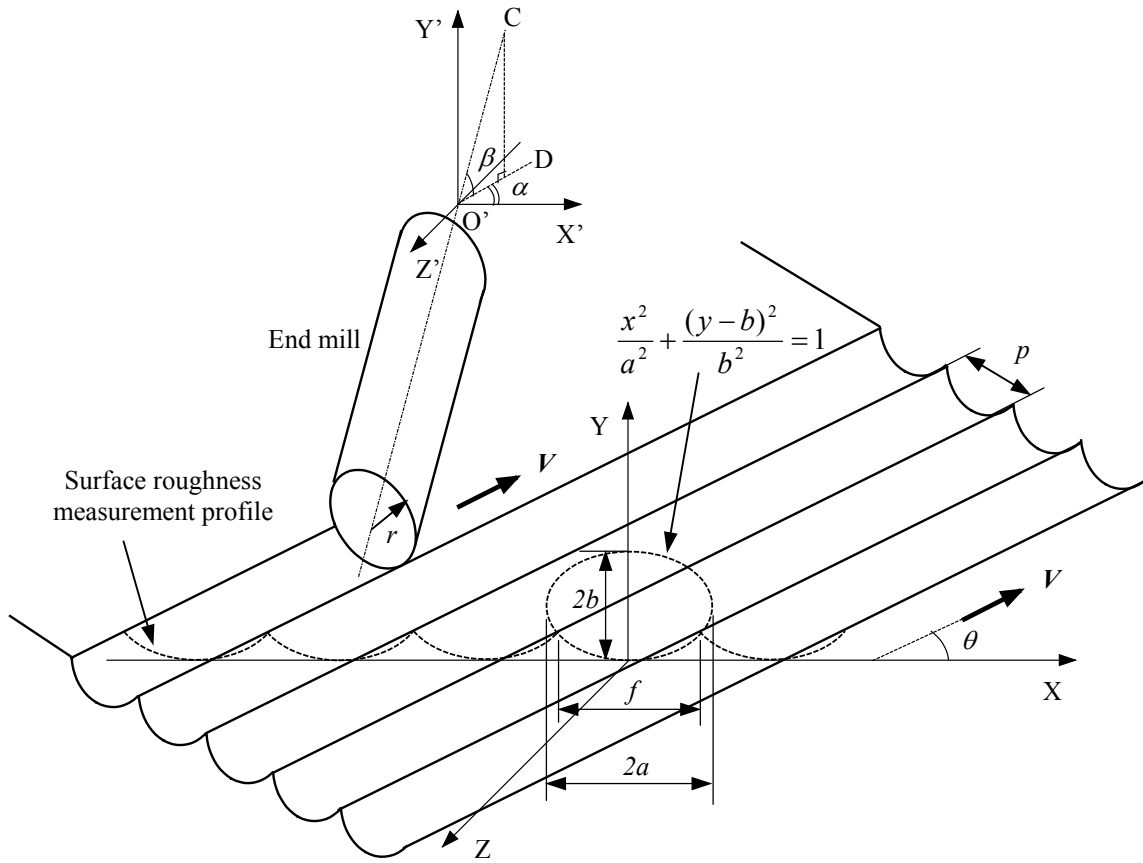


Fig. B.1. The measurement profile on the surface machined by flat-end milling.

Appendix C. Derivation of the Closed-Form R_a and R_q Using the Parametric Form

As shown in Fig. 1, the elliptical arc, with a and b as the major and minor semi-axis and center at $(0, b)$, on the surface profile can be expressed in the parametric form.

$$x = a \cos \theta \quad (\text{C.1})$$

$$y = b \sin \theta + b \quad (\text{C.2})$$

Define $S(\theta)$ as follows:

$$S(\theta) = \int y dx = \int (b \sin \theta + b)(-a \sin \theta) d\theta = ab \left(\cos \theta + \frac{1}{4} \sin 2\theta - \frac{1}{2} \theta \right) \quad (\text{C.3})$$

Thus, \bar{y} can be expressed as

$$\bar{y} = \frac{1}{f} \int_{-f/2}^{f/2} y dx = \frac{2}{f} \left(S(\theta_e) - \frac{\pi}{4} ab \right) \quad (\text{C.4})$$

Two new parameters, θ_c and θ_e , are defined by $y(\theta_c) = \bar{y}$ and $x(\theta_e) = \frac{f}{2}$.

$$\theta_c = \arcsin \left(\frac{\bar{y}}{b} - 1 \right) - \pi \quad (\text{C.5})$$

$$\theta_e = -\arccos\left(\frac{f}{2a}\right) \quad (\text{C.6})$$

The arithmetic average roughness R_a and root-mean-square roughness R_q of the theoretical profile then can be derived and represented by the following formulas.

$$R_a = \frac{1}{f} \int_{-f/2}^{f/2} |y - \bar{y}| dx = \frac{1}{f^2} \left[8a \cos \theta_c \cdot S(\theta_e) - 2f \cdot S(\theta_c) - 2\pi a^2 b \cos \theta_c + \pi abf \right] \quad (\text{C.7})$$

$$R_q = \sqrt{\frac{1}{f} \int_{-f/2}^{f/2} (y - \bar{y})^2 dx} = \sqrt{-\bar{y}^2 + 2b\bar{y} - \frac{f^2 b^2}{12a^2}} \quad (\text{C.8})$$